UNIVERSITY OF ALBERTA

DESIGN OF GRADIENT AND SHIM COIL SYSTEMS FOR *IN VIVO* NMR

BY

QIN LIU ©

A THESIS
SUBMITTED TO THE FACULTY OF GRADUATE STUDIES AND RESEARCH
IN PARTIAL FULFILLMENT OF THE REQUIREMENTS FOR THE DEGREE
OF
DOCTOR OF PHILOSOPHY

IN

MEDICAL PHYSICS

DEPARTMENT OF PHYSICS

EDMONTON, ALBERTA
FALL 1996

Canada

UNIVERSITY OF ALBERTA

LIBRARY RELEASE FORM

NAME OF AUTHOR: Qin Liu
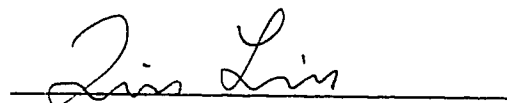
TITLE OF THESIS: Design of Gradient and Shim Coil Systems for *in vivo* NMR

DEGREE: Doctor of Philosophy

YEAR THIS DEGREE GRANTED: 1996
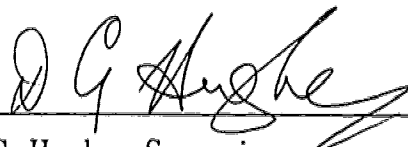
Qin Liu
Department of Physics
University of Alberta
Edmonton, Alberta
T6G 2J1

Date: *October 2, 1996*

UNIVERSITY OF ALBERTA

FACULTY OF GRADUATE STUDIES AND RESEARCH

The undersigned certify that they have read, and recommend to the Faculty of Graduate Studies and Research for acceptance, a thesis entitled "Design of Gradient and Shim Coil Systems for *in vivo* NMR" submitted by Qin Liu in partial fulfillment of the requirements for the degree of Doctor of Philosophy in Medical Physics.

D.G. Hughes, Supervisor
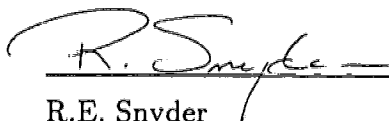
P.S. Allen

F.E. Vermeulen

J.A. Tuszynski

R.E. Snyder

M. Razavy

B.K. Rutt

Date: September 23, 1996

To Yang and Tina
For Their Love and Support

ABSTRACT

The work described in the first part of the thesis was stimulated by the very poor quality of the images obtained with an animal-size MRI system at the University of Alberta's *In vivo* NMR Facility. This was mainly caused by eddy current fields induced in the 40 cm bore Bruker superconducting magnet. The temporal and spatial dependence of these fields were therefore measured using the offset frequency of the proton signal from a small spherical sample. Three eddy currents were found, with decay times ranging from 13 to 480 ms. These currents generated very large gradients and significant field shifts, which led us to construct, in house, a set of distributed current, shielded gradient coils of minimum inductance. During the installation of the gradient coils, it became apparent that very accurate registration of the primary and shielding coils was required to achieve proper shielding. The effect of misregistration of the coils was therefore studied by determining the artifacts that would be produced in typical imaging and spectroscopic protocols by a small relative axial displacement of the primary and shielding coils in a shielded z gradient set from their proper locatio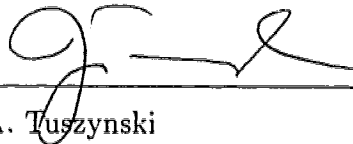n. Numerical values of the tolerance required for minimal artifacts ranged from 0.1 mm for STEAM proton spectroscopy to 1 mm for SE, FLASH and MBEST imaging.

Another defect found in the animal-size MRI system was an axial (z) variation in the magnetic field, which was predominantly fourth order in z, and could only be one-third compensated by the z^4 shim coil provided by the manufacturer, with a power dissipation of 100 watts. This led us to study, theoretically, the power dissipation and field profile accuracy of z^4 shim coils of various designs, and to construct a shim coil that compensated the z^4 field variation with a power dissipation of only 21 watts.

Many MRI protocols require strong gradients which can be switched rapidly.

This requires gradient coils of low inductance and low power dissipation in generating a given gradient. Since these are strongly dependent on the volume within the coil, and since the human body is more elliptical than circular in "cross section", the second part of the thesis studies the design of gradient coils which utilize distributed currents flowing on the surface of an elliptic cylinder. General expressions were derived for the magnetic field and stored energy associated with currents flowing azimuthally and axially on the surface of an elliptic cylinder. It was then shown how these expressions could be used to design elliptical z gradient coils of minimum inductance. Allowing the current to flow axially as well as azimuthally greatly reduced the field nonuniformity in transverse planes. For a coil design with an axial ratio of 0.75, the gradient nonlinearity along the z axis and field nonuniformity in the transverse directions were $< 0.1\%$ out to $0.66a$ and $0.5a$, respectively, over the region $|z| < 0.4a$, where a is the semi-major axis of the ellipse.

ACKNOWLEDGEMENTS

TABLE OF CONTENTS

LIST OF TABLES

LIST OF FIGURES

Chapter One

INTRODUCTION

1.1 Background to the Thesis

Since its discovery in 1945, nuclear magnetic resonance (NMR) has had extensive applications in chemistry, biomedicine and physics. However, it was not until 1973 that it was widely appreciated that the proportionality of the NMR frequency of magnetic nuclei, to the strength of the magnetic field experienced by them, enables their spatial distribution in an object to be imaged by deliberately making the magnetic field spatially dependent [1, 2]. The development of the appropriate technology led to applications to diagnostic medicine. The technique, now called magnetic resonance imaging (MRI), usually achieves the spatial localization by superimposing uniform magnetic field gradients on the large homogeneous main magnetic field. When a field gradient is applied, the resonance frequency of the magnetic nuclei will depend upon their location in the gradient direction. To achieve spatial encoding in three-dimensional space, three mutually orthogonal gradients are used, a longitudinal one in the direction of the main field and two transverse ones which are directed at orthogonal orientations in a plane perpendicular to the main field. These gradients are generated by a set of three gradient coils inserted into the main magnet. In most imaging protocols, the gradients are applied as short pulses.

Ideally, a gradient coil must be able to produce a uniform field gradient over a large volume, be capable of being switched on and off rapidly, as well as being characterized by a high coil efficiency (gradient per unit current) and low power dissipation. In the early development of MRI, gradient coils were constructed using discrete current path approaches, examples being Maxwell coils for generating longitudinal gradients and Golay (saddle) coils for generating transverse gradients [3, 4].

1

Such coils are easy to construct. However, they have large inductances, so that the gradient pulses have long rise and fall times. Moreover, the volume over which a uniform gradient can be achieved in such coils is quite limited. Nevertheless, these types of gradient coils were common in early MRI systems due to their simplicity. MRI techniques developed more recently, in particular fast imaging [5, 6], require much better performance by gradient coils. A number of improvements have been made, in particular the use of coils with distributed windings, which approximate a required continuous current distribution in a coil, and the development of the target field approach [7] for designing such coils. The main advantage of a gradient coil with distributed windings over that with discrete windings is that it is able to generate a more uniform gradient over a larger volume. The target field approach, on the other hand, not only facilitates designs of distributed winding coils, but also enables one to optimize coil performance by minimizing the power dissipation or the stored energy (which in turn shortens the switching time), or any combination of the two [8].

The switching of magnetic field gradients induces several eddy currents in the conducting structures of the main magnet. These are particularly troublesome in superconducting magnets because of the presence of cryogenic shields made of low resistivity material. The induced eddy currents decay exponentially, thereby generating exponentially decaying inhomogeneous magnetic fields which cause image artifacts [9, 10]. The eddy current fields also cause spectral artifacts in *in vivo* NMR spectroscopy (MRS) [11], another important application of NMR in medicine, when volume localization is achieved using gradient pulses.

One way to compensate the effect of eddy currents is to modify the shape of the current pulses fed to the gradient coils using the so-called pre-emphasis unit in the gradient system, so as to cancel the eddy current field in the region of interest. In order to implement the compensation successfully, knowledge of the eddy current

2

fields is needed, so that amplitudes and time constants of the compensating currents can be chosen accordingly. This compensation scheme requires little or no hardware modification if the eddy current fields are primarily uniform gradients.

An entirely different approach is to prevent the eddy currents occurring in the first place, by magnetically shielding the gradient coil. This can be done by passing a current through a suitably designed shielding coil which surrounds the main gradient coil [12]. Although adding the shielding coil results in a loss of space inside the main magnet and a reduced coil efficiency, shielded gradient coils can greatly reduce artifacts caused by eddy current fields [13, 14].

1.2 Overview of the Thesis

The work described in this thesis is a result of collaboration with Dr. P.S. Allen, director of the University of Alberta's *In vivo* NMR Facility. It began in the late 1980s, when measurements on phantoms showed that a 40 cm bore, 2.35 T Bruker MR system, used for animal studies in the *In vivo* NMR Facility, displayed serious intensity artifacts in MRI, as a result of eddy current fields [10]. A preliminary study made by measuring the offset frequency of the proton free induction decay (FID) obtained from a small spherical water sample, after switching off a field gradient, showed that the eddy current fields had very large amplitudes, and that the pre-emphasis unit was poorly adjusted [15]. In particular, the time constants of the compensation currents did not match those of the eddy currents. A more detailed study of the eddy current fields in this Bruker magnet was therefore carried out. It showed that the eddy currents generated field gradients that were quite uniform. However, the planes where the eddy current fields were zero did not pass through the "isocentre" of the gradient set, the point where the three applied gradient fields are zero. Thus, each eddy current could be regarded as generating both an exponentially decaying gradient field which is zero at the isocentre, and a

large homogeneous field which decays exponentially at the same rate. This large homogeneous field, sometimes called a field shift or a B_0 shift, combined with the very large gradient associated with each eddy current, showed that it was necessary to use shielded gradient coils in the system, in order to obtain high quality images and spectra.

Since shielded gradient coils that met our specifications were not available at the time, three shielded, distributed current, cylindrical gradient coils of minimum inductance were constructed "in house" using designs kindly provided by Dr. R. Turner at the National Institutes of Health in Bethesda, Maryland. Construction of the x gradient coil was described in my M.Sc. thesis [16]. A y gradient coil of similar design was fabricated around the x gradient coil, and a z gradient coil was wound with wire around both coils. In constructing and installing these coils, it became clear that an important aspect is the constructional tolerance required to achieve minimal artifacts in MRI and MRS. This issue was addressed theoretically by determining the artifacts generated in various imaging and spectroscopic protocols resulting from a small axial displacement of the primary and shielding coils in a shielded, distributed current, cylindrical z gradient set.

In upgrading the 40 cm bore, 2.35 T Bruker MR system with a view to using it for fast imaging studies, it was also found that the axial variation of the field strength, which was predominantly fourth order in the axial, z, coordinate, could only be one-third compensated using the room-temperature z^4 shim coil provided by the manufacturer. Moreover, the associated power dissipation was about 100 watts, leading to temperature increases in the sample space of up to 12°C in one hour. The relative merits of different designs of z^4 shim coils was therefore investigated by studying the effects of changing various design parameters on the power dissipation and field profile accuracy. A replacement z^4 shim coil, which provided full compensation of the z^4 field variation with a power dissipation only 21 watts, was

built and installed on the shielded gradient set just mentioned.

Because of financial difficulties, this Bruker system had to be shut down in 1994 in order to concentrate available resources on a newly acquired 80 cm bore, 3 T whole-body MR system. It was decided, therefore, to switch to a theoretical study of elliptic cylinder gradient coil designs. Even though funding was later obtained via an NSERC Collaborative Project Grant, it was decided to continue with this project, especially since the work was relevant to the project for which the grant was awarded.

As we have seen, two important characteristics of a gradient system are its power dissipation and switching time. For a given gradient driver, these are, respectively, governed by the resistance and inductance of the gradient coil. Because the aspect ratio of a typical human body at its largest cross-section is significantly different from unity, coils which are more elliptical than circular in section can be advantageous in *in vivo* NMR since they allow a better "filling factor" to be achieved, thereby reducing the power dissipation as well as the rise and fall times of the gradient pulses. In the study of elliptic cylinder gradient coil designs, general expressions were derived for the magnetic field and stored energy associated with a distributed current flowing on the surface of an elliptic cylinder. During the course of the work, we became aware of a proposed design of an elliptic cylinder z gradient coil by Petropoulos *et al.* [17]. However, these workers restricted the current flow to the azimuthal direction, whereas our expressions were derived by assuming that the current flows in both the azimuthal and axial directions. Our expressions can, in principle, be used to design, not only elliptic cylinder gradient coils, but also elliptic cylinder coils that generate a uniform field or a higher order shim field. Our expressions have been used to design an elliptic cylinder z gradient coil which generates a much more uniform gradient than can be achieved using a purely azimuthal current alone.

5

In the rest of this chapter, relevant aspects of basic principles of NMR and MRI are reviewed. The study of eddy current fields induced by gradient switching is presented in Chapter Two. In Chapter Three, constructional tolerances of shielded gradient coil sets in relation to artifacts in MRI and errors in *in vivo* MRS are treated. The design of a low-power-dissipation, cylindrical z^4 shim coil is presented in Chapter Four, followed by the design of elliptic cylinder gradient coils in Chapter Five. Finally, some conclusions are given in Chapter Six.

1.3 Basic Concepts of NMR

1.3.1 Nuclear Magnetic Moments and a Classical Description of NMR

Many nuclei are known to possess a magnetic moment μ and an associated spin angular momentum $\hbar I$. The two quantities are related by

$$\mu = \gamma \hbar I, \tag{1.1}$$

where γ is the magnetogyric ratio which is different for different nuclei, and $\hbar$ is Planck's constant divided by 2π. When placed in a static magnetic field B_0, whose direction is taken to be the z direction, say, an isolated nucleus of angular momentum $\hbar I$ has $2I + 1$ discrete energy levels given by

$$E = -\gamma \hbar B_0 m_I, \tag{1.2}$$

where m_I is the quantum number of the z component of the angular momentum which takes the values $I, I-1, \ldots, -I$. Transitions can be induced between adjacent levels by applying a radio-frequency (rf) magnetic field of angular frequency

$$\omega_0 = \gamma B_0 \tag{1.3}$$

perpendicular to B_0.

6

In general, the complete treatment of a nuclear spin system requires quantum mechanics. If, however, the system contains a group of non-interacting spins, the macroscopic magnetization of the spin system in a magnetic field B obeys the classical equation of motion [18]

$$\frac{dM}{dt} = M \times \gamma B, \tag{1.4}$$

where M is the macroscopic magnetization, defined as the sum of the nuclear magnetic moments per unit volume.

According to Eq. (1.4), a magnetization M, initially inclined at an angle θ to a steady field B_0, say, will precess around B_0 with an angular frequency

$$\omega_0 = -\gamma B_0, \tag{1.5}$$

while keeping θ constant. This angle can be changed by applying a field B_1 rotating in the transverse plane perpendicular to B_0 and in the same sense as the precessing magnetization. Thus, for nuclei with a positive magnetogyric ratio, B_1 is of the form

$$B_1 = B_1 \left(i \cos \omega t - j \sin \omega t \right), \tag{1.6}$$

where ω is its angular frequency, and i and j are unit vectors in the x and y directions.

To visualize the behavior of the magnetization M under the influence of B_0 and B_1 more clearly, a rotating frame (x', y', z') is used. This rotating frame rotates at the same frequency, and in the same sense, as B_1 about its z' axis which coincides with the z axis of the previous laboratory frame. Thus, both B_0 and B_1 appear to be stationary in the rotating frame. The magnetization M can be expressed as

$$M = M_{x'}i' + M_{y'}j' + M_{z'}k', \tag{1.7}$$

where i', j' and k' are unit vectors along the x', y' and z' axes of the rotating frame.

The derivative of M with respect to time is then given by

$$\frac{dM}{dt} = \left(\frac{\partial M_{x'}}{\partial t}i' + \frac{\partial M_{y'}}{\partial t}j' + \frac{\partial M_{z'}}{\partial t}k'\right) + \left(M_{x'}\frac{\partial i'}{\partial t} + M_{y'}\frac{\partial j'}{\partial t} + M_{z'}\frac{\partial k'}{\partial t}\right). \quad (1.8)$$

By using relations

$$\frac{\partial i'}{\partial t} = \omega \times i', \qquad \frac{\partial j'}{\partial t} = \omega \times j', \qquad \frac{\partial k'}{\partial t} = \omega \times k', \quad (1.9)$$

where ω is the angular frequency vector of the rotating frame, and by denoting

$$\left(\frac{dM}{dt}\right)_{rot} = \left(\frac{\partial M_{x'}}{\partial t}i' + \frac{\partial M_{y'}}{\partial t}j' + \frac{\partial M_{z'}}{\partial t}k'\right), \quad (1.10)$$

Eq. (1.8) becomes

$$\frac{dM}{dt} = \left(\frac{dM}{dt}\right)_{rot} + \omega \times M. \quad (1.11)$$

Substituting for dM/dt using Eq. (1.4) and rearranging Eq. (1.11), one obtains

$$\left(\frac{dM}{dt}\right)_{rot} = M \times \gamma\left(B + \frac{\omega}{\gamma}\right). \quad (1.12)$$

Alternatively, Eq. (1.12) can be written in terms of an effective field,

$$\left(\frac{dM}{dt}\right)_{rot} = M \times \gamma B_{eff}, \quad (1.13)$$

where

$$B_{eff} = B + \frac{\omega}{\gamma}. \quad (1.14)$$

Equation (1.13) indicates that the motion of the magnetization in the rotating frame is governed by the same equation of motion as in the laboratory frame, provided that B_{eff}, defined in Eq. (1.14), is used in place of B. Thus, in the rotating frame, the magnetization precesses about B_{eff} with an angular frequency γB_{eff}.

If the x' axis of the rotating frame is taken along B_1, Eq. (1.14) becomes

$$B_{eff} = k'\left(B_0 - \frac{\omega}{\gamma}\right) + i'B_1, \quad (1.15)$$

At exact resonance, i.e. when ω is equal to γB_0, the effective field B_{eff} is given by

$$B_{eff} = i'B_1, \quad (1.16)$$

8

in which case the magnetization precesses in the rotating frame about the x' axis with an angular frequency γB_1. If the magnetization is initially in the z' direction, it will precess in the y'-z' plane. If B_1 is applied as a rectangular pulse of duration t_p, the magnetization will precess through an angle

$$\theta = \gamma B_1 t_p \tag{1.17}$$

as shown in Fig. 1.1a. If t_p is chosen such that $\theta = \pi/2$, the magnetization will rotate from the z'-axis to the y'-axis as shown in Fig. 1.1b. Such a pulse is referred to as a "90° pulse". If $\theta = \pi$, the magnetization is inverted so as to be antiparallel to B_0 as shown in Fig. 1.1c. Such a pulse is referred to as a "180° pulse".

If the frequency of B_1 is not equal to the resonance frequency γB_0, a situation called off-resonance, the magnetization will precess about B_{eff} which is no longer along the x'-axis of the rotating frame as can be seen from Eq. (1.15). In this case, inversion of the magnetization can never be achieved. Moreover, a pulse which would cause a 90° rotation if "on-resonance" will, if applied "off-resonance", leave some longitudinal magnetization, thereby creating a smaller transverse magnetization. While it is possible to adjust an "off-resonance" pulse to rotate the z magnetization through 90°, it will no longer be directed along the y'-axis.

Up to now it has been assumed that the spins are non-interacting so that their behaviour can be described by Eq. (1.4). However, in reality, nuclear spin systems undergo significant interactions. To take into account the interaction of spins, both with each other, and with their surroundings, Bloch [19] assumed that their magnetization M will undergo two distinct relaxation processes. One is relaxation of the magnetization in the direction of B_0 towards its equilibrium value denoted by M_0. For a spin system with spin number $I = 1/2$, this process is described by a single exponential characterized by a time constant T_1, and is called longitudinal relaxation. The second relaxation process concerns relaxation of the magnetization in the plane perpendicular to B_0 towards its equilibrium value of zero. This pro-
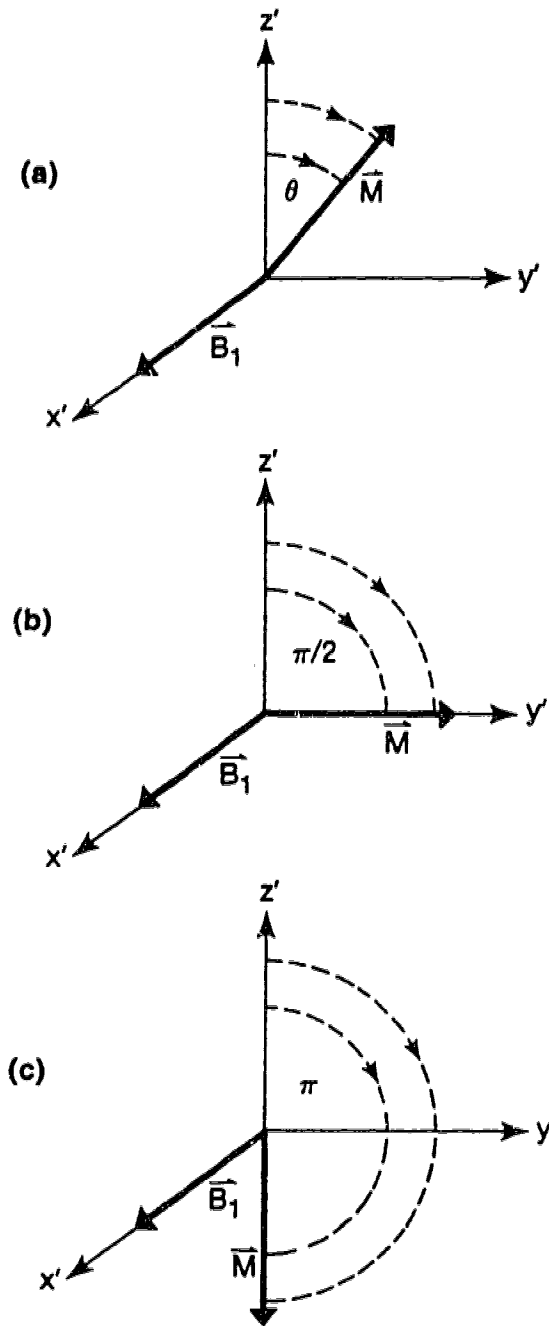
Figure 1.1: Precession of the nuclear magnetization M (for $\gamma > 0$) in the rotating frame about an "on-resonance" B_1 field through an angle of (a) θ, (b) $\pi/2$ and (c) π, expressed in radians. The primes here refer to the rotating frame.

10

cess is called transverse relaxation and is, in many cases, exponential with a time constant T_2. Bloch then made the assumption that the behaviour of M resulting from relaxation could be superimposed on the motion of the magnetization of non-interacting spins in the magnetic field, as given by Eq (1.4). This leads to the so-called Bloch equations, namely

$$\frac{dM_x}{dt} = \gamma(M_y B_0 + M_z B_1 \sin \omega t) - \frac{M_x}{T_2}, \tag{1.18}$$

$$\frac{dM_y}{dt} = \gamma(M_z B_1 \cos \omega t - M_x B_0) - \frac{M_y}{T_2}, \tag{1.19}$$

$$\frac{dM_z}{dt} = -\gamma(M_x B_1 \sin \omega t + M_y B_1 \cos \omega t) - \frac{M_z - M_0}{T_1}. \tag{1.20}$$

The Bloch equations are valid for many liquid-like systems found in biomedical applications of NMR. In liquids, the magnetic field that a spin experiences due to adjacent spins tends to average to zero because of the rapid random motion of the spins. In this so-called extreme narrowing limit, the transverse magnetization approaches to its equilibrium value exponentially as assumed by Bloch.

1.3.2 Detection of NMR Signals

In an NMR spectrometer, the rf magnetic field that excites the spins is generated by applying an rf voltage to a transmitter coil, which is wound in such a way that the rf field is perpendicular to B_0. That generates a linearly polarized rf field which can be decomposed into two contra-rotating components of equal amplitude. The component which rotates in the same sense as the precessing nuclear magnetization is the B_1 referred to in Eq. (1.6). It generates a rotating transverse magnetization, whereas the effect of the other rotating component is negligible.

The rotating transverse magnetization induces an rf voltage in a so-called receiver coil. This voltage is subsequently amplified and detected. Because of relaxation, the rotating magnetization decays to zero and so therefore does the rf

11

voltage induced in the coil. This decaying rf voltage is called a free induction decay (FID). In many cases, the same coil serves as both the transmitter and receiver coil.

The high frequency component of the rf signal is removed by phase-sensitive detection in which the rf signal is, in effect, multiplied by a reference signal whose frequency is normally the frequency of the rf pulse that excites the spins. The resulting signal has two components with frequencies equal to the sum and difference of the rf signal frequency and the reference frequency. A low-pass filter then filters out the high frequency component. By using so-called quadrature detection, two phase-sensitive detectors with reference signals differing in phase by 90°, one can distinguish signal frequencies which are higher than the reference frequency, from those which are lower. The use of such phase-sensitive detection is equivalent to observing the motion of the magnetization from a frame rotating at the frequency of the reference signal, instead of from the laboratory frame.

Fourier transformation of the detected FID converts it into a frequency spectrum. Provided the duration of the rf excitation pulse satisfies the condition

$$t_p \ll (\Delta\nu)^{-1},\qquad (1.21)$$

where $\Delta\nu$ is the width of the NMR spectrum, the Fourier transform of the FID corresponds to the spectrum obtained in a continuous wave (cw) experiment [18] in which a weak rf magnetic field is continuously applied while the frequency or the main magnetic field is swept through the resonance region. Eq. (1.21) implies that the whole spectrum is uniformly excited.

1.3.3   The Spin-Echo Technique

If the static magnetic field is perfectly homogeneous, the transverse magnetization decays with a time constant T_2, governed by the intrinsic relaxation mechanisms of the spin system. However, the magnetic field is not perfectly homogeneous in

12

practice, whether due to the NMR hardware, or due to variations in magnetic susceptibility at regional boundaries in a heterogeneous sample, so that spins in different regions experience different field strengths, and hence precess at different frequencies. This results in a dephasing of the spins, which in turn results in more rapid decay of the transverse magnetization. In many cases, the decay is roughly exponential and the decay time is then given the symbol T_2^*. In liquid-like systems, the effect of the field inhomogeneity on the decay of the transverse magnetization is usually much larger than that of intrinsic relaxation mechanisms characterized by T_2. However, the process of spin dephasing due to the static field inhomogeneity can be reversed, using a method pioneered by Hahn [20], by applying a 180° pulse at a time τ, say, after the initial 90° pulse which rotated the magnetization from its equilibrium position into the transverse plane.

Following the 90° pulse, spins experiencing different field strengths are precessing at different frequencies, spins with a lower precession frequency lagging behind those with a higher precession frequency, resulting in a loss of phase coherence. Application of the 180° pulse causes the spins with a lower precession frequency to be an equal amount ahead of those with a higher precession frequency. It follows that all the spins come in phase, or refocus, at a time 2τ after the 90° pulse, thereby generating a transverse magnetization with an amplitude governed only by the intrinsic decay with a time constant T_2. The signal generated by such a 90°–τ–180° pulse sequence is called a spin echo.

If the 180° pulse is in phase with the 90° pulse, the spins will refocus to form a magnetization in the opposite direction to the original magnetization, and the spin echo is therefore inverted as compared with the FID. If, however, the phase of the 180° pulse is shifted by 90° relative to the 90° pulse, the spins will refocus to form a magnetization in the same direction as the original magnetization, and the spin echo is therefore of the same sign as the FID, as shown in Fig. 1.2. A spin
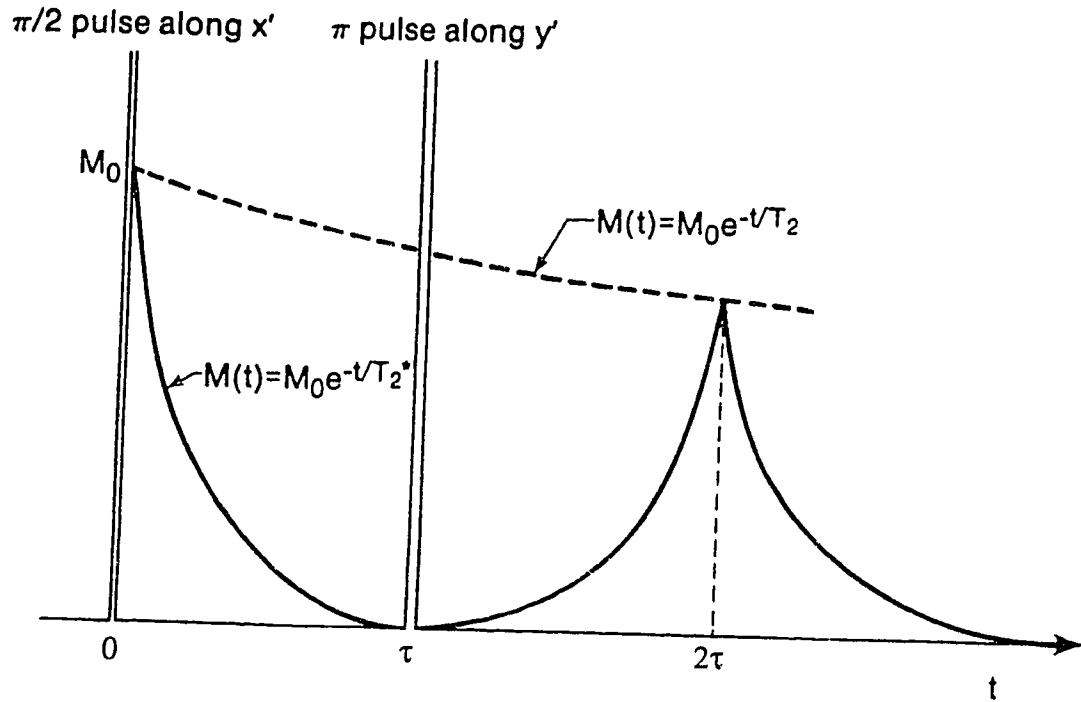
Figure 1.2: A spin-echo experiment. A 90° pulse along the x'-axis rotates the magnetization on to the y'-axis. The signal arising from this magnetization decays with a characteristic time T_2^*. At a time τ, a 180° pulse is applied along the y'-axis causing the magnetization to refocus at a time 2τ. The magnetization at 2τ is reduced from its initial value of M_0 because of the intrinsic T_2 relaxation.

echo can be considered to be two "back to back" free induction decays with their maximum amplitudes occurring at a time 2τ after the 90° pulse, as shown in the figure.

Spin-echo techniques were originally developed for measuring transverse relaxation times T_2. Now they are widely used in high-resolution NMR spectroscopy and in magnetic resonance imaging.

1.4 Basic Concepts of MRI

The basis of NMR applications to MRI is the fundamental relationship given by Eq. (1.3). While conventional high-resolution NMR spectroscopy demands that the applied magnetic field be homogeneous so that slight differences in local fields associated with the unique environment of nuclear spins can be revealed in the NMR spectrum, magnetic resonance imaging makes use of the fundamental relationship in a rather different manner by requiring that the applied magnetic field be spatially dependent. If the spatial dependence of the field is known, the spatial dependence of NMR parameters, such as spin density and relaxation times, can be obtained from the frequency domain representation of the NMR signal. The spatial dependence of the magnetic field is usually achieved by superimposing a uniform magnetic field gradient on B_0. A field gradient is in general given by

$$
\begin{aligned}
G &= \nabla B_z \\
&= i\frac{\partial B_z}{\partial x} + j\frac{\partial B_z}{\partial y} + k\frac{\partial B_z}{\partial z} \\
&= iG_x + jG_y + kG_z,
\end{aligned}
\tag{1.22}
$$

where $G_x = \partial B_z/\partial x$, $G_y = \partial B_z/\partial y$ and $G_z = \partial B_z/\partial z$ are the x, y and z gradients, respectively. When such a gradient is applied, the z component of the total field at the location r becomes spatially dependent and is given by

$$
B_z(r) = B_0 + G \cdot r.
\tag{1.23}
$$

15

The transverse components of the gradient field, $B_x(\boldsymbol{r})$ and $B_y(\boldsymbol{r})$ are unimportant since they are perpendicular to the large main field $\boldsymbol{B_0}$.

Since NMR imaging was initially proposed in the early 1970s, many imaging methods, such as point, line, planar, and three-dimensional imaging, have been reported. In this section, so-called two-dimensional Fourier imaging [21] will be used as an example to illustrate the basic principle of MRI, since it is a widely used technique, which has been adopted on most commercial imaging systems, and is the basis on which many MRI protocols were developed.

In two-dimensional imaging, it is necessary to isolate a slice of the object to be imaged. This can be achieved by applying a selective 90° pulse in the presence of a uniform field gradient whose direction, say the z direction, is perpendicular to the slice. An ideal selective 90° pulse is one that rotates spins whose resonance frequencies lie in a narrow range of frequency, $\Delta\omega$ say, through 90°, but does not excite spins outside this range. That is, the representation of the pulse in the frequency domain is a rectangle which is centered at ω, the frequency of the rf field, and has a width of $\Delta\omega$. It is known from Fourier transform theory [22] that such a representation in the frequency domain requires the time domain signal to be a sinc function shown in Fig. 1.3a. Such a function is characterized by side-lobes extending out to infinity, and is therefore entirely inappropriate in practice. However, if the sinc function is multiplied by a gaussian function, the side-lobes of the sinc function will be suppressed, as illustrated in Fig. 1.3b, without seriously compromising the rectangular shape in the frequency domain.

After application of the selective 90° pulse in the presence of a uniform gradient G_z, all spins in a slice of thickness

$$\Delta z = \frac{\Delta\omega}{\gamma G_z} \tag{1.24}$$

16
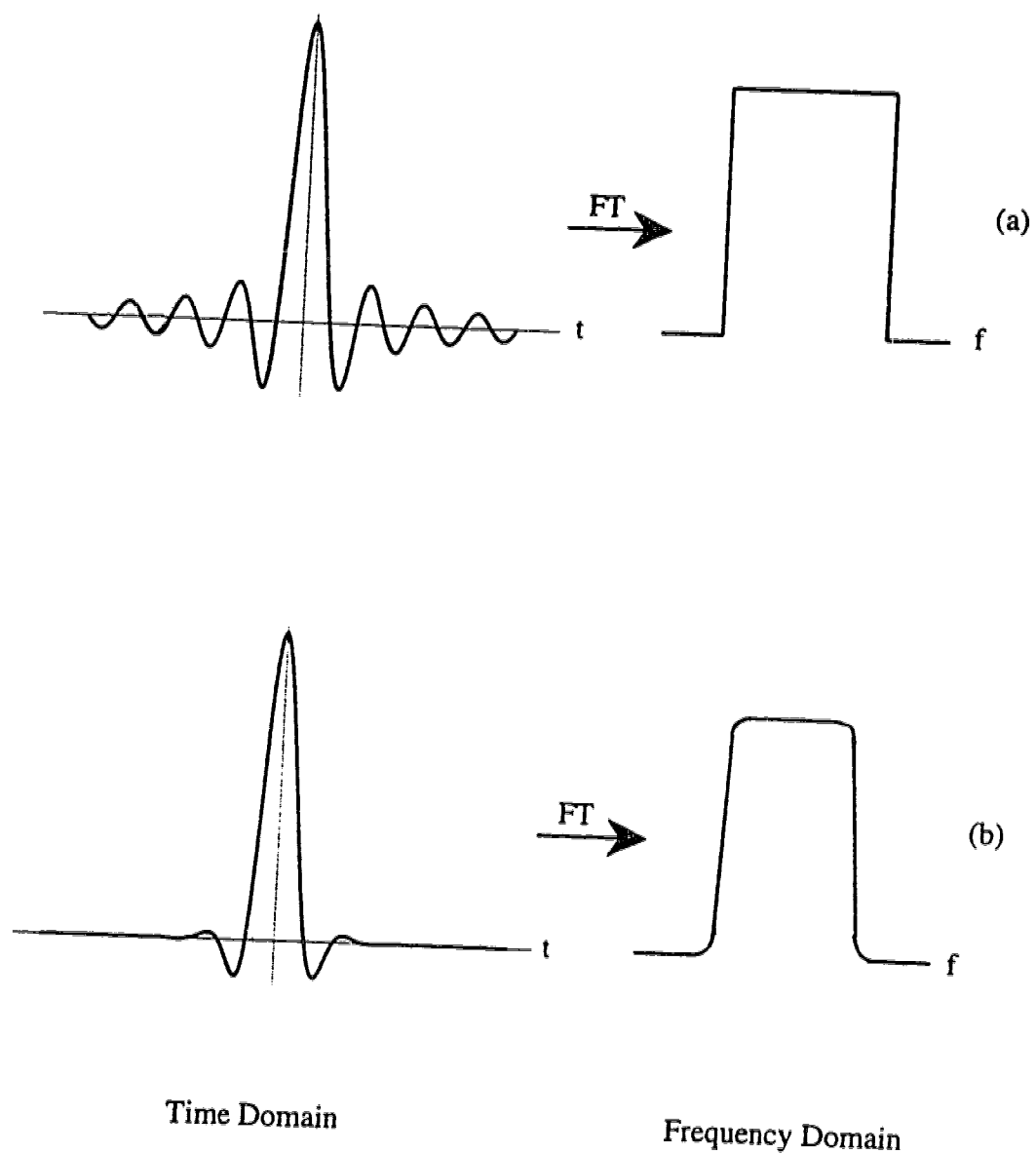
Figure 1.3: (a) A sinc function and its Fourier transform, and (b) a sinc function multiplied by a gaussian function and the corresponding Fourier transform.

normal to the z axis and centered at

$$z = \frac{\omega - \gamma B_0}{\gamma G_z} \qquad (1.25)$$

will have been rotated through 90° into the x-y plane, but will have accumulated different phases in the process. For all the spins except those experiencing the smallest gradient field offsets, the phase distribution is almost linearly dependent on the displacement from the central plane. The accumulated phase is therefore equivalent to that which would be acquired in the same gradient field as that applied during the slice selection, for a time equal to half the duration of the slice selection. Such spins can therefore be brought in phase by reversing the direction of the z gradient immediately after the selective pulse is switched off, and leaving the reversed gradient on for half the duration of the selective pulse, as shown in Fig. 1.4.

After slice selection has been achieved, the location of spins within the slice is encoded into the NMR signal by employing two orthogonal gradients which are perpendicular to the gradient used for the slice selection. If the slice is perpendicular to the z direction, then a gradient G_x, say, can be used to encode x positional information into the frequency of the NMR signal and a gradient G_y can be used to encode y positional information into the phase of the signal.

The frequency encoding in the x direction is achieved by acquiring the signal in the presence of G_x. Since spins with different x coordinates precess at different frequencies, their x coordinates are encoded into the frequency of the signal. To conform to the sampling theorem, the rate at which the signal is sampled must be at least twice as high as the highest frequency of the signal [22]. That is, the time interval, Δt say, between samplings of the signal must satisfy the following relation,

$$\Delta t \leq \frac{\pi}{\gamma G_x L_x}, \qquad (1.26)$$

where L_x is the extent of the slice in the x direction. The total number of sample
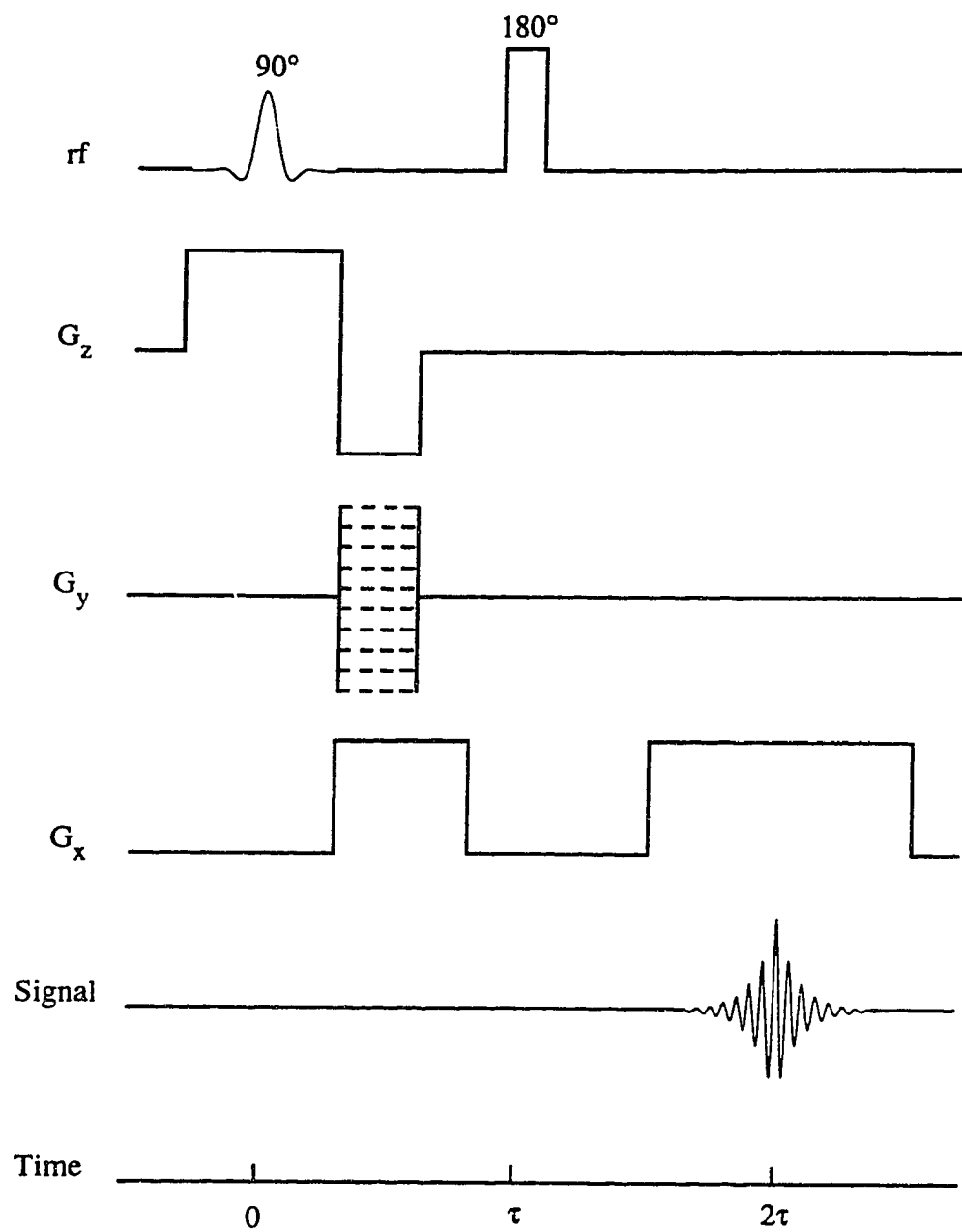
Figure 1.4: A pulse sequence for two-dimensional Fourier imaging.

points determines the spatial resolution in the so-called frequency-encoding direction.

Encoding the y positional information of the spins into the phase of the NMR signal is achieved by applying a y gradient pulse prior to acquisition of the signal, as shown in Fig. 1.4. By the end of the gradient pulse, spins with different y coordinates will have acquired different phases because they will have precessed at different frequencies during the gradient pulse. To obtain a two-dimensional image, the phase of the signal is incremented by repeating the imaging sequence while incrementing the amplitude of the y gradient pulse by a constant amount each time. A two-dimensional image can be obtained by two-dimensional Fourier transformation of the resulting time domain signals. The required increment in the amplitude of the gradient, G_{ymin}, is governed, according to the sampling theorem, by the following relation,

$$\gamma \int_0^{\tau_{phase}} G_{ymin}(t)dt \leq \frac{\pi}{L_y},\qquad(1.27)$$

where L_y is the extent of the slice in the y direction, and τ_{phase} is the duration of the y gradient pulse. The number of increments is determined by the desired resolution in the so-called phase-encoding direction.

The frequency encoding can, in principle, be achieved by applying only one gradient pulse and recording the time domain signal during the pulse, as was described earlier. However, dephasing of spins during the finite rise time of the gradient pulse causes serious loss of signal. To overcome this problem, two gradient pulses are applied in the frequency-encoding direction, as shown in Fig. 1.4, in combination with the spin-echo pulse sequence. In Fig. 1.4, the first x gradient pulse, called the read compensation gradient pulse, causes the spins to dephase. After the gradient is switched off, a 180° rf pulse is applied, followed by a second x gradient pulse, the so-called read gradient pulse, which has the same polarity as the first. This causes the spins to rephase and a spin echo to form at a time when the time

20

integral of the read gradient pulse is equal to that of the read compensation gradient pulse. By choosing the strength and duration of the read compensation gradient pulse appropriately, it can be arranged for the echo to be formed in a constant field gradient, well after the rise time of the read gradient pulse. An important requirement is that the echo be formed at the same time 2τ at which the echo is formed in the absence of gradient pulses. Otherwise, there will be a loss of signal due to inhomogeneity of the main magnetic field [10]. Since the spin-echo technique is used, this imaging protocol is often called spin-echo (SE) imaging.

References

[1] P.C. Lauterbur, *Nature, Lond.* **242**, 190 (1973).

[2] P. Mansfield and P.K. Grannell, *J. Phys. C: Solid State Phys.* **6**, L422 (1973).

[3] I.E. Tanner, *Rev. Sci. Instrum.* **36**, 1086 (1965).

[4] M.J.E. Golay, *Rev. Sci. Instrum.* **29**, 313 (1958).

[5] P. Mansfield and I.L. Pykett, *J. Magn. Reson.* **29**, 355 (1978).

[6] A. Haase, J. Frahm, D. Matthaei, W. Hänicke, and K.D. Merboldt, *J. Magn. Reson.* **67** 258 (1986).

[7] R. Turner, *J. Phys. D: Appl. Phys.* **19**, L147 (1986).

[8] R. Turner, *Magn. Reson. Imaging* **11**, 903 (1993).

[9] R.M. Henkelman and M.J. Bronskill, *Rev. Magn. Reson. Med.* **2**, 1 (1987).

[10] D.G. Hughes, S. Robertson, and P.S. Allen, *Magn. Reson. Med.* **25**, 167 (1992).

[11] R.J. Ordidge and I.D. Cresshull, *J. Magn. Reson.* **69**, 151 (1986).

[12] P. Mansfield and B. Chapman, *J. Phys. E: Sci. Instrum.* **19**, 540 (1986).

[13] B. Chapman, R. Turner, R.J. Ordidge, M. Doyle, M. Cawley, R. Coxon, P. Glover, and P. Mansfield, *Magn. Reson. Med.* **5**, 246 (1987).

[14] R. Turner, B. Chapman, A.M. Howseman, R.J. Ordidge, R. Coxon, P. Glover, and P. Mansfield, *J. Magn. Reson.* **80**, 248 (1988).

[15] S. Robertson, D.G. Hughes, Q. Liu, and P.S. Allen, *Magn. Reson. Med.* **25**, 158 (1992).

[16] Q. Liu, M.Sc. Thesis, University of Alberta, 1991.

[17] L.S. Petropoulos, M.A. Martens, R.W. Brown, M.R. Thompson, M.A. Morich, and J.L. Patrick, *Meas. Sci. Technol.* **4**, 349 (1993).

[18] C.P. Slichter, "The Principles of Magnetic Resonance," Springer-Verlag, New York, 1978.

[19] F. Bloch, W.W. Hansen, and M.E. Packard, *Phys. Rev.* **69**, 127 (1946).

[20] E.L. Hahn, *Phys. Rev.* **80**, 580 (1950).

[21] A. Kumar, D. Welti, and R.R. Ernst, *J. Magn. Reson.* **18**, 69 (1975).

[22] E.O. Brigham, "The Fast Fourier Transform," Prentice-Hall, Englewood Cliffs, New Jersey, 1974.

Chapter Two

QUANTITATIVE CHARACTERIZATION OF THE EDDY CURRENT FIELDS IN A 40 CM BORE SUPERCONDUCTING MAGNET[1]

2.1 Introduction

Slowly decaying eddy currents, induced in the structure of superconducting magnet systems by the switching of magnetic field gradients, have been found to cause intensity artifacts in MRI [1, 2] and phase and baseline artifacts in MRS [3, 4]. These can be especially troublesome in some smaller magnet systems manufactured in the 1980s.

In a preliminary study [5], we analysed the time dependent magnetic field generated by a rectangular gradient pulse in a 40 cm bore, 2.35 T Bruker magnet, manufactured in 1984. Using a small spherical sample of doped water situated at various locations in the sample space, measurements made with the pre-emphasis (eddy current compensation) unit activated were quite well fitted to a sum of five decaying exponentials. One was associated with the decay of the current in the gradient coil, two were caused by eddy currents generated in the magnet structure and two negative components were associated with the pre-emphasis itself. The fact that the time constants and amplitudes of the fields generated by the pre-emphasis were by no means equal to those of the eddy current fields, demonstrated the inadequacy of adjusting the pre-emphasis by monitoring the proton FID from an extended sample.

---

[1]A version of this chapter has been published. Q. Liu, D.G. Hughes, and P.S. Allen, *Magn. Reson. Med.* **31**, 73 (1994).

To determine the specifications of an active compensation protocol for eddy current fields, the spatial symmetries of the exponentially decaying components of these eddy current fields must be determined, as well as their amplitudes and time constants. In this chapter, we present accurate measurements of the spatial and temporal dependence of the eddy current fields caused by switching off a gradient with the pre-emphasis unit deactivated. The measurements were carried out for all three gradient directions. Some of the data have been presented earlier in preliminary form [6]. A very different approach using the proton FID obtained from an extended sample has been described by Boesch *et al.* [7].

2.2 Experimental

A hard (non-selective) 90° rf pulse was applied to a 13 mm diameter spherical sample of doped water at a variable time after switching off a long (10 s duration) gradient pulse. The long duration ensured that the eddy current field generated by switching on the gradient had already decayed before the gradient was switched off. The reference frequency of the phase-sensitive detector, f_{ref}, was set to the proton resonance frequency in the absence of a gradient pulse, so that the detected FID was a slowly decaying signal, the decay being mainly caused by the small field inhomogeneity across the sample. Any change in the magnetic field, caused by the switched gradient, would result in a change in the resonance frequency, and the detected FID would be a decaying oscillatory signal. The frequency of the oscillation, δf, is the difference between the resonance frequency and f_{ref}, and is called the offset frequency. Because of the proportionality of the NMR frequency and the magnetic field, given by Eq. (1.3), the eddy current field can be determined by measuring δf. Because the sample experiences a magnetic field gradient associated with the switched gradient, the detected FID is modulated, both in amplitude and frequency, as illustrated in Fig. 2.1. The offset frequency, δf, was determined
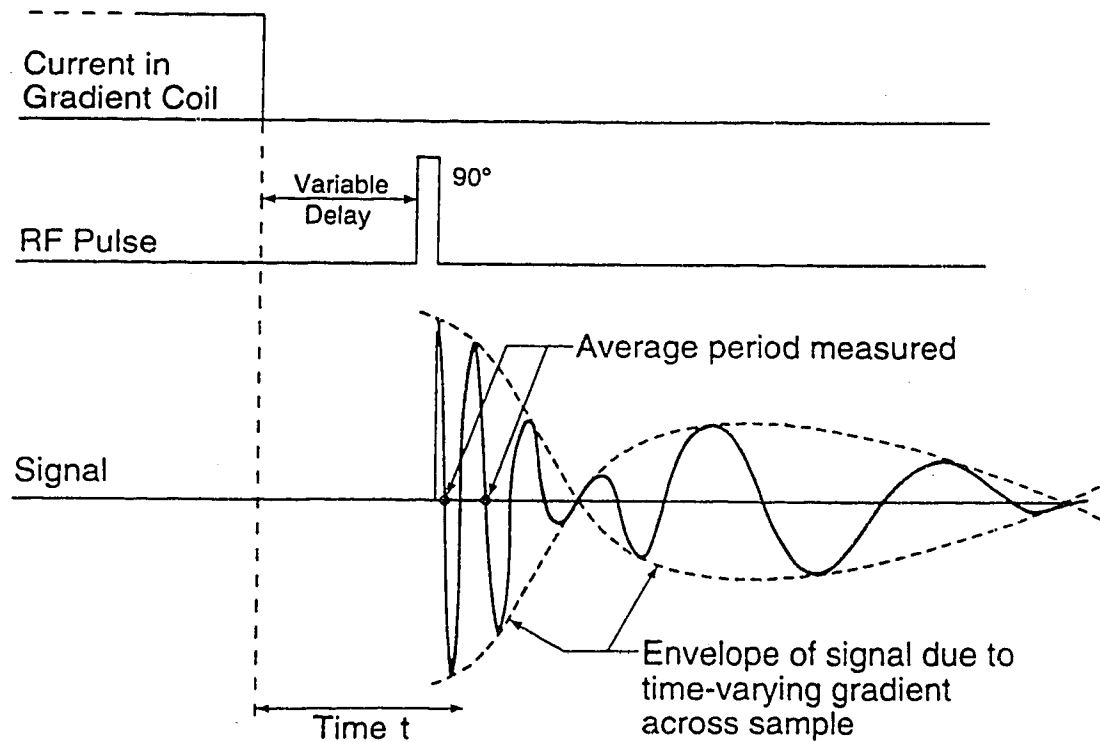
Figure 2.1: The pulse sequence used to measure the offset frequency of the proton resonance from a 13 mm diameter sample of doped water as a function of the time t after switching off a gradient.

by measuring the time between cross-over points as indicated in the figure. The procedure was then repeated, with the sample at the same location, using some sixty different time delays, following switch-off of the gradient, ranging from 0.5 ms to 3 s. The measurement of small offset frequencies, less than 100 Hz, was facilitated by offsetting the reference frequency of the detector so that, in every case, the two cross-over points occurred well before the first zero of the envelope of the FID (see Fig. 2.1).

Figure 2.2 shows offset frequency data obtained by switching off a -850 Hz/cm (-2.0×10^{-3} T/m) x gradient, when the center of the sample was located at $x = -4.0$ cm, $y = 0$, $z = 0$ relative to the (nominal) magnet isocentre. (In our coordinate system, the $+x$ axis was vertically upward.) The data were successfully fitted, using the BMDP subroutine [8] run on an Amdahl 5870 computer, to a sum of four decaying exponentials

$$\delta f = \sum_{i=0}^{3} A_i \exp\left(-t/\tau_i\right) + B \qquad (2.1)$$

where B is a time independent parameter which allows for a small departure from the exact "on resonance" condition. The data are in excellent agreement with Eq. (2.1) which is illustrated by the continuous curve in Fig. 2.2, thereby confirming that the offset frequency is a sum of exponential decays, notwithstanding the possibility of coupling between various eddy current loops [9]. The amplitudes A_i and the decay times τ_i of the curve shown in Fig. 2.2 are listed in Table 2.1, ordered so that $\tau_0 < \tau_1 < \tau_2 < \tau_3$. The sum of the amplitudes ($A_0 + A_1 + A_2 + A_3$) is (3440 ± 40) Hz, in excellent agreement with the offset frequency, (3460 ± 80) Hz, measured *during* the gradient pulse after the eddy currents caused by the switch-on had died away. This offset frequency is shown in Fig. 2.2 as a horizontal dotted line. The value of B was found to be (0.6 ± 0.2) Hz, showing only a small departure from the exact "on resonance" condition.

The measurements were repeated with the center of the sample at the loca-
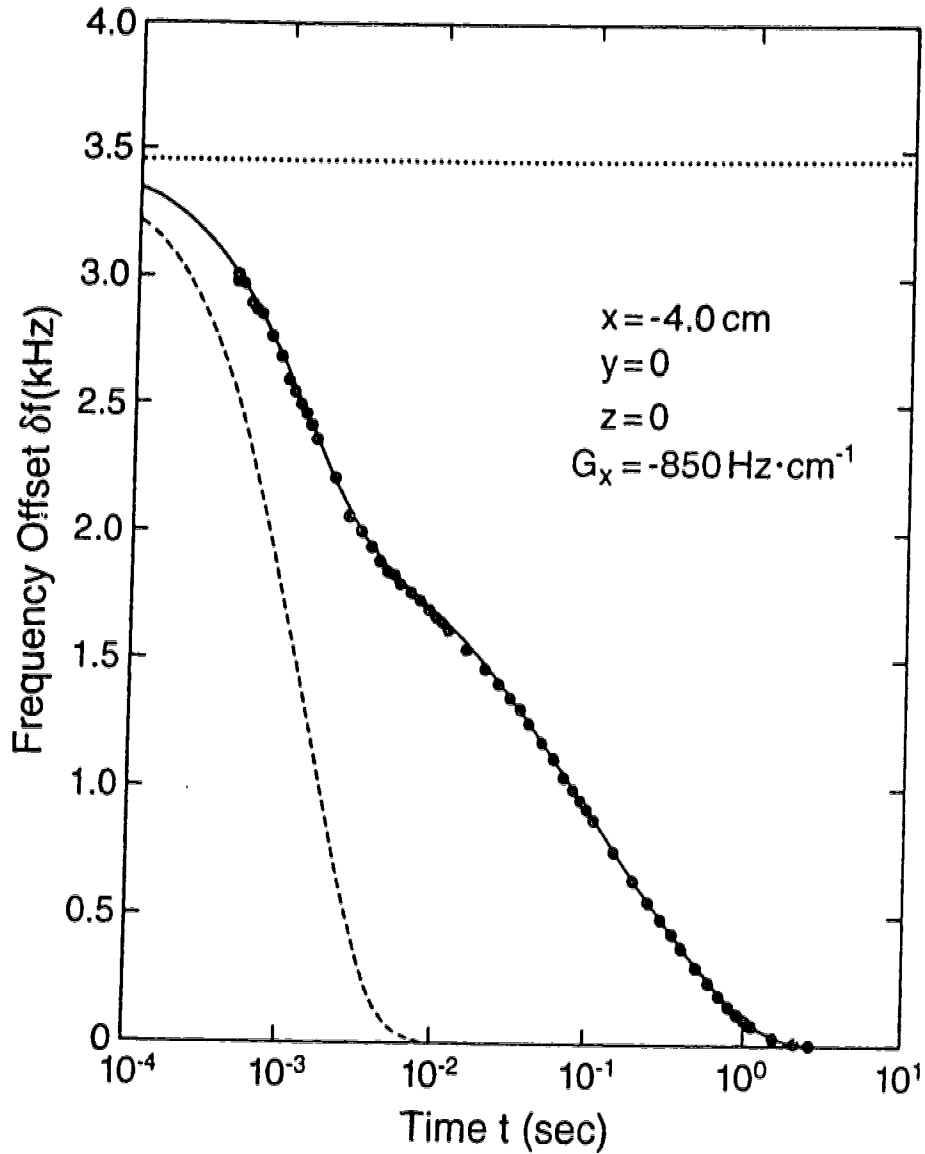
Figure 2.2: The offset frequency, δf, of the proton resonance obtained from a 13 mm diameter spherical sample of doped water situated at $x = -4$ cm, $y = 0$, $z = 0$, caused by switching off a -850 Hz/cm (-2.0×10^{-3} T/m) x gradient at time $t = 0$. The continuous curve shows a least squares fit of the data to Eq. (2.1). The horizontal dotted line shows the offset frequency measured during a long gradient pulse after eddy currents caused by the switch-on had died away. The broken curve shows the expected behaviour of δf in the absence of eddy currents.

Table 2.1: Amplitudes and decay times of the exponentially decaying components found by fitting the data obtained at $x = -4$ cm and shown in Fig. 2.2.

Component (i)	Amplitude A_i (Hz)	Decay time τ_i (ms)
0	1486 ± 17	1.36 ± 0.04
1	437 ± 25	16.8 ± 1.7
2	646 ± 25	93 ± 5
3	867 ± 11	492 ± 4

tions $x = -2, -1, 1, 2$, and 4 cm, $y = 0$, $z = 0$. With the exception of the $x = 1$ cm data, each data set was independently fitted to Eq. (2.1). The $x = 1$ cm data set was successfully fitted to a sum of *three* decaying exponentials rather than four. This was understood later when it was found that the amplitude of A_2 was coincidentally near zero at that location. During these measurements, it was found that to obtain robust fits to Eq. (2.1), the offset frequencies had to be measured with a precision of better than about 1%. This was accomplished without signal averaging so that each data set took only about one hour to acquire.

The value of the shortest decay time, τ_0, found at each location was approximately equal to the time constant of the x gradient coil, $L/R \simeq 1.3$ ms, and is evidently primarily associated with the decay of the current in the gradient coil itself. The corresponding values, τ_1, τ_2, and τ_3, found at each location were in agreement within the error limits generated by the fitting procedure (roughly $\pm 10\%$ for τ_1, $\pm 5\%$ for τ_2, and $\pm 1\%$ for τ_3). This evidence supports the very plausible assumption that the x gradient generates just three discrete eddy currents (the $i = 2$

Table 2.2: Decay times given by "global fits" of the data obtained by switching off -850 Hz/cm x, y, and z gradients.

	Decay times τ_i in ms for the		
Components (i)	x gradient	y gradient	z gradient
0	1.32 ± 0.01	1.32 ± 0.03	1.59 ± 0.04
1	14.9 ± 0.6	13.5 ± 1.8	13.8 ± 2.5
2	80.5 ± 1.4	77 ± 5	70 ± 5
3	481 ± 1	478 ± 3	362 ± 5

eddy current being masked by the effect of the pre-emphasis in earlier, less accurate, measurements [5]), and led us to process all the data sets together, constrained to be characterized by the *same* four decay times but a different set of amplitudes and a different value of B. Values of τ_i obtained from such a "global fit" to Eq. (2.1), conducted using a modified BMDP subroutine [8], are listed in the second column of Table 2.2 and the values of A_i are plotted in Fig. 2.3a as a function of x. In all cases, the values of B were $\lesssim 1$ Hz.

On the basis of the above, the data in Fig. 2.2 can be interpreted as follows. The broken curve, which corresponds to a single exponential decay with an amplitude of 3460 Hz and a decay time of 1.3 ms, illustrates the approximate behaviour expected in the absence of eddy currents. However, in practice, as the current in the x gradient coil falls to zero, the three eddy currents build up in accordance with Lenz's law, thereby generating, between them, an offset frequency of about 2000 Hz,
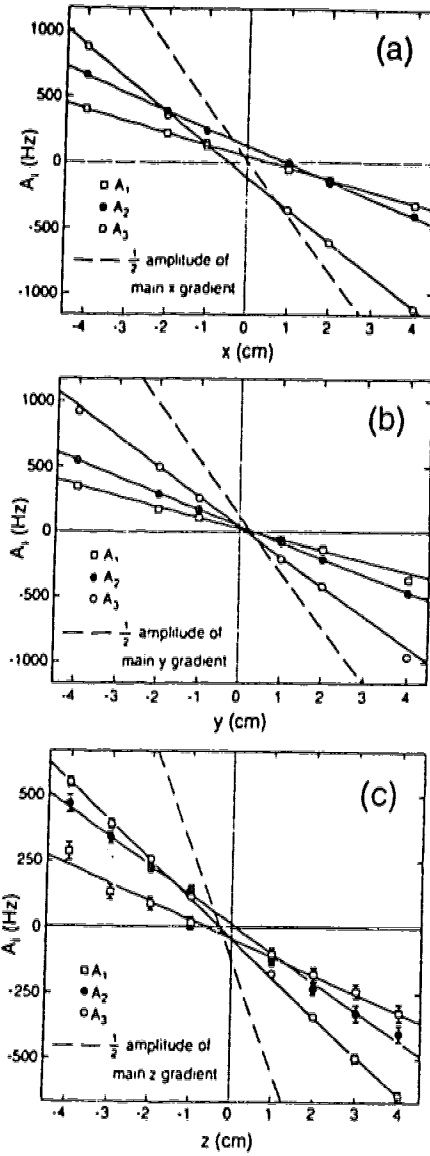
Figure 2.3: (a) Amplitudes A_1, A_2, and A_3 of the exponentially decaying components of the eddy current fields, generated by switching off a -850 Hz/cm $(-2.0 \times 10^{-3}$ T/m$)$ x gradient, plotted as a function of x. The solid lines are linear regressions of the data. The broken line shows half the amplitude of the x gradient, measured prior to the switch-off in the absence of eddy currents. (b) and (c) Corresponding graphs for the y and z gradients. (Note the different ordinate scale in (c).)

more than 50% of the main gradient. This offset frequency then slowly decays to zero.

Eddy current fields generated by the y and z gradients were measured in a similar manner by switching off y and z gradients of the same amplitude -850 Hz/cm (-2.0×10^{-3} T/m) as used for the x gradient. Each data set was successfully fitted to Eq. (2.1). The decay times obtained from "global fits" of the data are listed in the third and fourth columns of Table 2.2 and the amplitudes are plotted in Figs. 2.3b and 2.3c as a function of the corresponding coordinate.

The location of the true isocentre of the magnet, which is required for proper interpretation of the data, was found by measuring the gradient field (in the absence of eddy currents) as a function of the corresponding coordinate to be at

$$ x = (0.02 \pm 0.01)\text{cm}, \quad y = (0.31 \pm 0.01)\text{cm}, \quad z = (-0.28 \pm 0.04)\text{cm}, \quad (2.2) $$

relative to the nominal isocentre.

2.3 Discussion

Two important pieces of information about the eddy current fields can be determined from the data obtained, namely, the decay times and the amplitude distribution of the components. While both are necessary for the complete design of active compensation strategies, it is the amplitude characteristics which demonstrate the key insight that the eddy current fields in our magnet manifest themselves as field shifts and gradients.

The similarity between the decay times of the eddy current components induced by the x and y gradient fields (see Table 2.2), supports the view that these gradients induce eddy currents in the *same* set of conductors and that these conductors are essentially cylindrical and coaxial with the z axis of the magnet.

31

The shorter decay times and smaller amplitudes of the eddy current components induced by the z gradient are attributed to differences in the geometric coupling of the z coil to the cryostat structure, from those of the transverse gradient coils. The smaller error limits shown in Table 2.2 for the decay times associated with the x gradient arise because measurements for the x gradient were repeated several times in a search for a possible dependence of the decay times on the level of the cryogens in the magnet. No such dependence was found. The error limits associated with the decay times found for the z gradient are larger than those of the x and y gradients because of the smaller eddy currents generated by the z gradient.

The linear regression lines in Figs. 2.3a – 2.3c are in very good agreement with the amplitude data, clearly demonstrating that the eddy currents generate primarily uniform gradients, at least over a region extending 4 cm on either side of the nominal isocentre. However, it can be seen in Fig. 2.3a that the individual eddy currents induced by the x gradient generate zero field at locations ranging from −0.5 cm to 1.0 cm, showing that the gradients are accompanied by significant field shifts at the isocentre. The same is true to a lesser extent of the z gradient, while, for the y gradient, zero field occurs very near the true isocentre. Values of the individual gradients, G, and the accompanying field shifts, ΔB_0, measured at the location of the true isocentre (see Eq. (2.2)) are listed in Table 2.3.

The values of ΔB_0 seem to be associated with a small departure of the magnet cryostat from exact symmetry about the isocentre, since the cryostat is expected to be most symmetric about the vertical $y = 0$ (longitudinal) plane and least symmetric about the horizontal $x = 0$ plane, as observed.

Our finding that the eddy current field distribution due to each gradient is primarily composed of three gradient components plus accompanying zero order field shifts is different from the conclusions drawn by Boesch et al. [7, 10] on the basis of measurements made in a similar magnet to ours, but using an extended

Table 2.3: Gradient, G, and field shift, ΔB_0, at the true isocentre associated with each eddy current component.

Eddy current component		Inducing gradient		
		x	y	z
$i = 1$	G (Hz/cm)	-90.4 ± 1.0	-84.2 ± 3.1	-70.8 ± 3.6
	ΔB_0 (Hz)	39 ± 3	-8 ± 6	-26 ± 13
$i = 2$	G (Hz/cm)	-133 ± 1	-126 ± 3	-112 ± 3
	ΔB_0 (Hz)	120 ± 3	10 ± 6	39 ± 14
$i = 3$	G (Hz/cm)	-250 ± 1	-230 ± 1	-150 ± 2
	ΔB_0 (Hz)	-116 ± 2	43 ± 6	-4 ± 10

12 cm diameter spherical sample. The highly nonlinear (nonuniform) gradients observed by these workers may have been caused by eddy currents induced closer to the sample space, *e.g.* in rf shields.

In summary, our results show that for one type of magnet, namely, a Bruker 40 cm bore, 2.35 T, 1984 vintage magnet, B_0 shift compensation alone is unlikely to accommodate phase distortions brought about by eddy currents fields. However, they also show that a measure of active eddy current compensation might be achieved by feeding a combination of exponentially decaying currents to the z_0 shim

coil and to the appropriate gradient coils. In the case of the horizontal transverse (y) gradient, no B_0 shift would be required. This may well be the case for other types of magnet systems which display a high degree of symmetry about the vertical longitudinal mid-plane.

As shown by Jehenson *et al.* [9], the amplitudes and decay times of such compensating currents are different from those of the exponentially decaying components of the eddy current fields. However, they can be calculated from the amplitudes and decay times of those components. Feeding compensating currents to the higher order shim coils as suggested by Van Vaals and Bergman [11] would seem to be unnecessary in our magnet.

We believe that the kind of measurements described above could be used to determine the eddy current components in other types of magnets, provided the number of important eddy currents is small.

References

[1] R.M. Henkelman and M.J. Bronskill, *Rev. Magn. Reson. Med.* **2**, 1 (1987).

[2] D.G. Hughes, S. Robertson, and P.S. Allen, *Magn. Reson. Med.* **25**, 167 (1992).

[3] R.J. Ordidge and I.D. Cresshull, *J. Magn. Reson.* **69**, 151 (1986).

[4] U. Klose, *Magn. Reson. Med.* **14**, 26 (1990).

[5] S. Robertson, D.G. Hughes, Q. Liu, and P.S. Allen, *Magn. Reson. Med.* **25**, 158 (1992).

[6] D.G. Hughes, Q. Liu, and P.S. Allen, Proceedings, 11th Annual Meeting, Society of Magnetic Resonance in Medicine, 1992, Berlin, p.362.

[7] C.H. Boesch, R. Gruetter, and E. Martin, *Magn. Reson. Med.* **20**, 268 (1991).

[8] Procedure P3R from "BMDP Statistical Software" (W.J. Dixon, Ed.), p.290, University of California Press, Los Angeles, 1983.

[9] P. Jehenson, M. Westphal, and N. Schuff, *J. Magn. Reson.* **90**, 264 (1990).

[10] C.H. Boesch and E. Martin, *Magn. Reson. Med.* **15**, 357 (1990).

[11] J.J. Van Vaals and A.H. Bergman, *J. Magn. Reson.* **90**, 52 (1990).

Chapter Three

CONSTRUCTIONAL TOLERANCES OF SHIELDED GRADIENT COIL SETS IN RELATION TO ARTIFACTS IN MRI AND ERRORS IN *IN VIVO* MRS[1]

3.1 Introduction

Slowly decaying eddy currents, induced in the structure of superconducting magnet systems by the switching of magnetic field gradients, can cause serious artifacts in both magnetic resonance imaging [1, 2] and magnetic resonance spectroscopy (MRS) [3, 4]. Such eddy currents and hence the consequent artifacts can be greatly reduced by means of actively shielded gradient coils [5], in which a current flowing in an outer, shielding coil, cancels the fringe field generated by the current flowing in the inner, primary coil.

An important issue, since shielded gradient sets can be readily constructed by well equipped machine shops, is the required constructional tolerance relative to acceptable artifact trade-off for specific applications in MRI and MRS. This issue is addressed here by treating theoretically the effect of a relative axial displacement of the primary and shielding coils in a z gradient set which utilizes distributed currents flowing on two coaxial cylindrical surfaces. This is accomplished by evaluating the eddy currents induced in a surrounding coaxial conducting cylinder when the current in the gradient set is switched. This, in turn, allows the eddy current field on the z axis of the coil to be determined. Expressions are then derived which enable the maximum tolerable relative displacement of the primary and shielding coils to be

---

determined for different imaging and spectroscopic protocols. The consequences are illustrated by incorporating in these expressions typical numerical dimensions obtained for representative animal-size (Bruker) and whole body-size (GE) magnet systems and shielded z gradient coil sets of minimum inductance design [6].

3.2 Theory

We shall present the theory of magnetic shielding of cylindrical coils in the first two subsections. The derivation is based on what was briefly outlined by Turner and Bowley [7]. The results obtained will then be used in the last subsection to treat the problem of misregistration in the construction of shielded gradient sets, which has not been addressed previously.

3.2.1 The Magnetic Field Generated by a Current Distributed on the Surface of a Cylinder

Since the switching rate of the magnetic field gradient in MRI and MRS is low, of the order of a kiloHertz, displacement currents may be ignored.

We shall consider the current confined to the surface of a cylinder, and use a cylindrical coordinate system in which the z axis coincides with the axis of the cylinder. The coordinates of a point in space (ρ, ϕ, z) are thus related to its cartesian coordinates (x, y, z) by

$$
\begin{aligned}
\rho &= \sqrt{x^2 + y^2} \\
\tan \phi &= \frac{y}{x} \\
z &= z.
\end{aligned}
\tag{3.1}
$$

We suppose that a surface current of density $J(r')$ which vanishes at infinity flows on the surface of a cylinder of infinite length and of radius a. The three components

37

of the vector potential $A(r)$, caused by this surface current, are given by

$$A_\rho(r) = \frac{\mu_0 a}{4\pi} \int_{-\pi}^{\pi} d\phi' \sin(\phi - \phi') \int_{-\infty}^{\infty} dz' \frac{J_{\phi'}(r')}{|r - r'|} \qquad (3.2)$$

$$A_\phi(r) = \frac{\mu_0 a}{4\pi} \int_{-\pi}^{\pi} d\phi' \cos(\phi - \phi') \int_{-\infty}^{\infty} dz' \frac{J_{\phi'}(r')}{|r - r'|} \qquad (3.3)$$

$$A_z(r) = \frac{\mu_0 a}{4\pi} \int_{-\pi}^{\pi} d\phi' \int_{-\infty}^{\infty} dz' \frac{J_{z'}(r')}{|r - r'|}, \qquad (3.4)$$

where $\mu_0 = 4\pi \times 10^{-7}$ N/A^2 is the permeability of free space.

To derive the required expression for the current distribution, we use the Green's function expansion [8]

$$\frac{1}{|r - r'|} = \frac{2}{\pi} \sum_{m=-\infty}^{\infty} \int_0^{\infty} dk\, e^{im(\phi-\phi')} \cos k(z - z')\, I_m(k\rho_<) K_m(k\rho_>), \qquad (3.5)$$

where $I_m(x)$ and $K_m(x)$ are the mth order modified Bessel functions of the first and second kind, respectively, and $\rho_<$ $(\rho_>)$ is the smaller (larger) of ρ and a. If the trigonometrical function $\cos k(z - z')$ is expressed in terms of exponential functions, Eq. (3.5) can be written as [7, 9]

$$\frac{1}{|r - r'|} = \frac{1}{\pi} \sum_{m=-\infty}^{\infty} \int_{-\infty}^{\infty} dk\, e^{im(\phi-\phi')} e^{ik(z-z')} I_m(|k|\rho_<) K_m(|k|\rho_>). \qquad (3.6)$$

The Fourier transforms of the components of $J(r')$ are defined as follows [7]

$$J_\phi^m(k) = \frac{1}{2\pi} \int_{-\pi}^{\pi} d\phi'\, e^{-im\phi'} \int_{-\infty}^{\infty} dz'\, J_{\phi'}(a, \phi', z') e^{-ikz'} \qquad (3.7)$$

$$J_z^m(k) = \frac{1}{2\pi} \int_{-\pi}^{\pi} d\phi'\, e^{-im\phi'} \int_{-\infty}^{\infty} dz'\, J_{z'}(a, \phi', z') e^{-ikz'}, \qquad (3.8)$$

so that the inverse Fourier transforms are

$$J_{\phi'}(a, \phi', z') = \frac{1}{2\pi} \sum_{m=-\infty}^{\infty} \int_{-\infty}^{\infty} dk\, J_\phi^m(k) e^{im\phi'} e^{ikz'} \qquad (3.9)$$

$$J_{z'}(a, \phi', z') = \frac{1}{2\pi} \sum_{m=-\infty}^{\infty} \int_{-\infty}^{\infty} dk\, J_z^m(k) e^{im\phi'} e^{ikz'}. \qquad (3.10)$$

38

By substituting Eq. (3.6) into Eqs. (3.2) – (3.4), and using the definitions (3.7) and (3.8), one finds that the components of A inside the cylinder ($\rho < a$) are

$$A_\rho(r) = \frac{i\mu_0 a}{4\pi} \sum_{m=-\infty}^{\infty} \int_{-\infty}^{\infty} dk\, J_\phi^m(k) e^{im\phi} e^{ikz} \left[I_{m-1}(|k|\rho) K_{m-1}(|k|a) \right.$$
$$\left. - I_{m+1}(|k|\rho) K_{m+1}(|k|a) \right] \tag{3.11}$$

$$A_\phi(r) = \frac{\mu_0 a}{4\pi} \sum_{m=-\infty}^{\infty} \int_{-\infty}^{\infty} dk\, J_\phi^m(k) e^{im\phi} e^{ikz} \left[I_{m-1}(|k|\rho) K_{m-1}(|k|a) \right.$$
$$\left. + I_{m+1}(|k|\rho) K_{m+1}(|k|a) \right] \tag{3.12}$$

$$A_z(r) = \frac{\mu_0 a}{2\pi} \sum_{m=-\infty}^{\infty} \int_{-\infty}^{\infty} dk\, J_z^m(k) e^{im\phi} e^{ikz} I_m(|k|\rho) K_m(|k|a). \tag{3.13}$$

One can write similar expressions for the components of A outside the cylinder ($\rho > a$) by exchanging ρ and a in the integrands in Eqs. (3.11) – (3.13).

In order to obtain the expression for the magnetic field B, we use Eqs. (3.9) and (3.10) to derive an important relation between $J_\phi^m(k)$ and $J_z^m(k)$. In the absence of charge accumulation, the equation of continuity states

$$\nabla' \cdot J(r') = 0. \tag{3.14}$$

If the current flows only on the surface of a cylinder of radius a, Eq. (3.14) reduces to

$$\frac{1}{a}\frac{\partial J_{\phi'}}{\partial \phi'} + \frac{\partial J_{z'}}{\partial z'} = 0. \tag{3.15}$$

Substituting Eqs. (3.9) and (3.10) into Eq. (3.15) yields

$$\frac{i}{2\pi} \sum_{m=-\infty}^{\infty} \int_{-\infty}^{\infty} dk \left[\frac{m}{a} J_\phi^m(k) + k J_z^m(k) \right] e^{im\phi'} e^{ikz'} = 0. \tag{3.16}$$

For Eq. (3.16) to be satisfied, the sum of the two terms in the square brackets must vanish for each value of m. Thus, $J_\phi^m(k)$ and $J_z^m(k)$ are related as follows

$$J_z^m(k) = -\frac{m}{ka} J_\phi^m(k). \tag{3.17}$$

By taking the curl of the vector potential A and using Eq. (3.17) and the recurrence relations for modified Bessel functions, namely [10]

$$I_{m-1}(x) = I_m'(x) + \frac{m}{x} I_m(x) \tag{3.18}$$

39

$$I_{m+1}(x) = I'_m(x) - \frac{m}{x}I_m(x) \tag{3.19}$$

$$K_{m-1}(x) = K'_m(x) - \frac{m}{x}K_m(x) \tag{3.20}$$

$$K_{m+1}(x) = -K'_m(x) + \frac{m}{x}K_m(x) \tag{3.21}$$

where $I'_m(x)$ and $K'_m(x)$ are, respectively, derivatives of $I_m(x)$ and $K_m(x)$ with respect to x, the components of the magnetic field B inside the cylinder can be written as follows

$$B_\rho(\mathbf{r}) = \frac{i\mu_0 a}{2\pi} \sum_{m=-\infty}^{\infty} \int_{-\infty}^{\infty} k\, dk\, J_\phi^m(k)e^{im\phi}e^{ikz}I'_m(|k|\rho)K'_m(|k|a) \tag{3.22}$$

$$B_\phi(\mathbf{r}) = -\frac{\mu_0 a}{2\pi\rho} \sum_{m=-\infty}^{\infty} \int_{-\infty}^{\infty} \frac{k}{|k|}dk\, J_\phi^m(k)e^{im\phi}e^{ikz}mI_m(|k|\rho)K'_m(|k|a) \tag{3.23}$$

$$B_z(\mathbf{r}) = -\frac{\mu_0 a}{2\pi} \sum_{m=-\infty}^{\infty} \int_{-\infty}^{\infty} |k|\, dk\, J_\phi^m(k)e^{im\phi}e^{ikz}I_m(|k|\rho)K'_m(|k|a). \tag{3.24}$$

Exchanging ρ and a in the integrand in Eq. (3.22), and replacing $I_m(|k|\rho)K'_m(|k|a)$ by $I'_m(|k|a)K_m(|k|\rho)$ in the integrands in Eqs. (3.23) and (3.24), yield the components of B outside the cylinder.

3.2.2 Magnetic Shielding of Cylindrical Coils

A current confined to the surface of a cylinder of radius a produces a magnetic field both inside and outside the cylinder. To reduce the magnetic field to zero at a finite radius outside the cylinder, let us introduce a second current of density $j(b, \phi'', z'')$, which is confined to the surface of a cylinder of infinite length and of radius b, where $b > a$. According to the result obtained in Section 3.2.1, the components of the magnetic field B outside the cylinder of radius b, generated by the currents on the surfaces of both cylinders, can be written as

$$\begin{aligned}
B_\rho(\mathbf{r}) = \frac{i\mu_0}{2\pi} \sum_{m=-\infty}^{\infty} \int_{-\infty}^{\infty} k\, dk\, \Big[&aJ_\phi^m(k)I'_m(|k|a) \\
&+ bj_\phi^m(k)I'_m(|k|b)\Big] e^{im\phi}e^{ikz}K'_m(|k|\rho)
\end{aligned} \tag{3.25}$$

40

$$B_\phi(\mathbf{r}) = -\frac{\mu_0}{2\pi\rho} \sum_{m=-\infty}^{\infty} m \int_{-\infty}^{\infty} \frac{k}{|k|} dk \left[a J_\phi^m(k) I_m'(|k|a) \right.$$
$$\left. + b j_\phi^m(k) I_m'(|k|b) \right] e^{im\phi} e^{ikz} K_m(|k|\rho) \qquad (3.26)$$

$$B_z(\mathbf{r}) = -\frac{\mu_0}{2\pi} \sum_{m=-\infty}^{\infty} \int_{-\infty}^{\infty} |k| \, dk \left[a J_\phi^m(k) I_m'(|k|a) \right.$$
$$\left. + b j_\phi^m(k) I_m'(|k|b) \right] e^{im\phi} e^{ikz} K_m(|k|\rho) \qquad (3.27)$$

where $J_\phi^m(k)$ is given by Eq. (3.7), and $j_\phi^m(k)$ is defined similarly as

$$j_\phi^m(k) = \frac{1}{2\pi} \int_{-\pi}^{\pi} d\phi'' \, e^{-im\phi''} \int_{-\infty}^{\infty} dz'' \, j_{\phi''}(b, \phi'', z'') e^{-ikz''}. \qquad (3.28)$$

It can be seen from Eqs. (3.25), (3.26) and (3.27) that, for the magnetic field everywhere outside the larger cylinder to be zero, it is required that

$$a J_\phi^m(k) I_m'(|k|a) + b j_\phi^m(k) I_m'(|k|b) = 0 \qquad (3.29)$$

for all m, which leads to

$$j_\phi^m(k) = -\frac{a I_m'(|k|a)}{b I_m'(|k|b)} J_\phi^m(k). \qquad (3.30)$$

Using Eqs. (3.17) and (3.30) one obtains a relation between the Fourier transforms of $J_{z'}(a, \phi', z')$ and $j_{z''}(b, \phi'', z'')$, namely

$$j_z^m(k) = -\frac{a^2 I_m'(|k|a)}{b^2 I_m'(|k|b)} J_z^m(k) \qquad (3.31)$$

where $J_z^m(k)$ is given by Eq. (3.8), and $j_z^m(k)$ is defined as

$$j_z^m(k) = \frac{1}{2\pi} \int_{-\pi}^{\pi} d\phi'' e^{-im\phi''} \int_{-\infty}^{\infty} dz'' \, j_{z''}(b, \phi'', z'') e^{-ikz''}. \qquad (3.32)$$

Eqs. (3.30) and (3.31) can be used to find the current distribution on the outer cylinder that will magnetically shield a coaxial cylindrical coil of smaller diameter which carries a current of known distribution.

Using Eqs. (3.22) – (3.24) and Eq. (3.30), the components of the magnetic field inside the shielded coil are found to be

$$B_\rho(r) = \frac{i\mu_0 a}{2\pi} \sum_{m=-\infty}^{\infty} \int_{-\infty}^{\infty} k\,dk\, J_\phi^m(k) e^{im\phi} e^{ikz}$$
$$\cdot I_m'(|k|\rho) K_m'(|k|a)(1 - S_m), \tag{3.33}$$

$$B_\phi(r) = -\frac{\mu_0 a}{2\pi\rho} \sum_{m=-\infty}^{\infty} \int_{-\infty}^{\infty} \frac{k}{|k|} dk\, J_\phi^m(k) e^{im\phi} e^{ikz}$$
$$\cdot m I_m(|k|\rho) K_m'(|k|a)(1 - S_m), \tag{3.34}$$

$$B_z(r) = -\frac{\mu_0 a}{2\pi} \sum_{m=-\infty}^{\infty} \int_{-\infty}^{\infty} |k|\,dk\, J_\phi^m(k) e^{im\phi} e^{ikz}$$
$$\cdot I_m(|k|\rho) K_m'(|k|a)(1 - S_m), \tag{3.35}$$

where

$$S_m = \frac{I_m'(|k|a) K_m'(|k|b)}{I_m'(|k|b) K_m'(|k|a)}. \tag{3.36}$$

It can be seen that if the S_m term is set to zero, Eqs. (3.33), (3.34) and (3.35) reduce to Eqs. (3.22), (3.23) and (3.24), respectively. Since the radius b is assumed to be greater than the radius a, both $I_m'(|k|a)/I_m'(|k|b)$ and $K_m'(|k|b)/K_m'(|k|a)$ are less than one. Also, since $I_m'(|k|a)/I_m'(|k|b)$ and $K_m'(|k|b)/K_m'(|k|a)$ are positive, S_m falls between 0 and 1. Therefore, shielding a coil, while maintaining the same current distribution in it, reduces the magnetic field inside it. This is reasonable because the magnetic field generated by the current in the inner or primary coil is partially cancelled by that generated by the current in the outer or shielding coil.

The S_m term naturally varies with b for fixed k and a. If b is equal to a, i.e., if the shielding coil coincides with the primary coil, S_m becomes unity and the magnetic field vanishes everywhere in space. In this case, we know, from Eqs. (3.30) and (3.31), that the required current in the shielding coil has the same distribution as the current in the primary coil, but flows in the opposite sense. If b is allowed to go to infinity, which is equivalent to removal of the shielding coil, then S_m goes to zero, $j(b, \phi'', z'')$ becomes zero, and the magnetic field given by Eqs. (3.33) – (3.35) is identical to that produced by the current in the primary coil, as expected.

3.2.3 Eddy Current Fields Caused by Misregistration in the Construction of Shielded Gradient Sets

We consider a shielded z gradient coil set, consisting of a primary coil cylinder of radius a and a shielding coil cylinder of radius b, each carrying a surface current. The set is located coaxially within a *single* long conducting cylinder of inner radius c. This configuration will give rise to just one eddy current distribution, whereas several eddy currents of different amplitudes and decay times are normally found in practice [11, 12, 13]. Nevertheless, this simple model, by representing the most significant eddy current, should provide a reasonable estimate of their effect. We shall first evaluate the initial magnitude of the residual eddy current field as a function of the relative displacement of the primary and shielding coils.

The magnetic field generated by a z gradient coil is independent of the azimuthal angle ϕ. Thus, only the $m = 0$ term exists in the expressions for the magnetic field given in Sections 3.2.1 and 3.2.2. Moreover, the axial component of the current density vanishes according to Eq. (3.17). Since the axial component of the magnetic field is antisymmetric about the $z = 0$ plane, the azimuthal component of the current density must also be antisymmetric about that plane. That is, the current density is an odd function of z. The Fourier transform of the current density must have the same symmetry property with respect to k. By taking the above constraints into account, the z component of the magnetic field, B_z^{prim}, generated at an external point (ρ, ϕ, z), where $\rho > a$, by a current flowing in the primary coil alone can be written as

$$B_z^{\text{prim}}(\rho, z) = -\frac{i\mu_0 a}{\pi} \int_0^\infty k\,dk\, J_\phi^0(k) \sin kz\, I_0'(ka) K_0(k\rho), \qquad (3.37)$$

where $J_\phi^0(k)$ is the Fourier transform of $J_\phi(z')$, the current density in the primary coil, defined as

$$J_\phi^0(k) = \int_{-\infty}^\infty dz'\, J_\phi(z') e^{-ikz'}. \qquad (3.38)$$

43

The field at a point within the primary coil is given by Eq. (3.37) with $I_0'(ka)K_0(k\rho)$ replaced by $I_0(k\rho)K_0'(ka)$. Using the identities $I_0'(z) = I_1(z)$ and $K_0'(z) = -K_1(z)$ [10], the magnetic field on the z axis, generated by a perfectly shielded z gradient coil, can be expressed as

$$B_z(z) = \frac{i\mu_0 a}{\pi} \int_0^\infty k\, dk\, J_\phi^0(k) \sin kz\, K_1(ka)(1 - S_0), \qquad (3.39)$$

where

$$S_0 = \frac{I_1(ka)K_1(kb)}{I_1(kb)K_1(ka)}. \qquad (3.40)$$

If the primary gradient coil is displaced in the z direction by a small distance Δz from its proper location in the shielded configuration, B_z^{prim} will become

$$B_z^{\mathrm{prim}}(\rho, z - \Delta z) = -\frac{i\mu_0 a}{\pi} \int_0^\infty k\, dk\, J_\phi^0(k) \sin k(z - \Delta z)\, I_0'(ka)K_0(k\rho). \qquad (3.41)$$

To a first approximation, B_z^{prim} is given by

$$B_z^{\mathrm{prim}}(\rho, z - \Delta z) = B_z^{\mathrm{prim}}(\rho, z) - \Delta z \frac{\partial B_z^{\mathrm{prim}}(\rho, z)}{\partial z}, \qquad (3.42)$$

where

$$\frac{\partial B_z^{\mathrm{prim}}(\rho, z)}{\partial z} = -\frac{i\mu_0 a}{\pi} \int_0^\infty k^2 dk\, J_\phi^0(k) \cos kz\, I_0'(ka)K_0(k\rho). \qquad (3.43)$$

Since the field generated by the current in the shielding coil cancels $B_z^{\mathrm{prim}}(\rho, z)$ in the region $\rho > b$, switching on a current in the shielded gradient set will cause the z component of the fringe field outside the shielding coil to increase from zero to

$$\Delta B_z^{\mathrm{prim}}(\rho, z) = -\Delta z \frac{\partial B_z^{\mathrm{prim}}(\rho, z)}{\partial z}. \qquad (3.44)$$

This change in field will induce an azimuthal eddy current in the surrounding conducting cylinder, which will generate a magnetic field with the same spatial symmetry as the fringe field $\Delta B_z^{\mathrm{prim}}(\rho, z)$. To evaluate the magnitude of this eddy current, we assume perfect passive shielding [7] and an eddy current that is essentially confined to the inner surface of the cylinder. Thus, the z component of the magnetic

field produced in the region $\rho > c$ by the eddy current density, $\sigma_{\phi'}(z')$ say, is given by

$$B_z^{\text{eddy}}(\rho, z) = -\frac{\mu_0 c}{\pi} \int_0^\infty k\, dk\, \sigma_\phi^0(k) \cos kz\, I_0'(kc) K_0(k\rho), \qquad (3.45)$$

where

$$\sigma_\phi^0(k) = \int_{-\infty}^\infty dz'\, \sigma_{\phi'}(z') e^{-ikz'}. \qquad (3.46)$$

Since this field, $B_z^{\text{eddy}}(\rho, z)$, totally cancels the fringe field given by Eq. (3.44) in the region $\rho > c$, the eddy current density must satisfy the condition

$$\sigma_\phi^0(k) = ik\Delta z \frac{aI_0'(ka)}{cI_0'(kc)} J_\phi^0(k). \qquad (3.47)$$

The assumption of perfect passive shielding presupposes that the characteristic decay time of the eddy current induced in the surrounding cylinder due to resistive losses, is much longer than the time scale which characterizes the switching of the current in the shielded gradient set. This condition is usually well satisfied in practice. The assumption that the eddy current is essentially confined to the inner surface of the conducting cylinder also presupposes that the electrical conductivity of the surrounding cylinder is sufficiently large that the skin depth at the frequencies associated with the gradient switching sequence is both small compared to the thickness of the cylinder and much smaller than its radius c. This may well be a good approximation for fast imaging modalities such as echo planar [14] where bipolar gradients are switched at a frequency ~ 1 kHz, but for switched gradients possessing a substantial dc component such as those used for slice selection, this is not the case. Nevertheless, in these latter situations, Eq. (3.47) should provide an upper limit for the initial eddy current density.

Since the initial amplitude of the z component of the magnetic field in the region $\rho < c$, generated by the eddy current, is given by

$$B_z^{\text{eddy}}(\rho, z) = -\frac{\mu_0 c}{\pi} \int_0^\infty k\, dk\, \sigma_\phi^0(k) \cos kz\, I_0(k\rho) K_0'(kc), \qquad (3.48)$$

it follows from Eq. (3.47) that the initial amplitude of the eddy current field on the axis of the shielded gradient set is given by

$$B_z^{\text{eddy}}(z) = \frac{i\mu_0 a}{\pi}\Delta z \int_0^\infty k^2 dk\, J_\phi^0(k)\cos kz\, K_1(kc)\frac{I_1(ka)}{I_1(kc)}. \tag{3.49}$$

In the absence of any further gradient switching, $B_z^{\text{eddy}}(z)$ will decay to zero because of resistive losses.

In most practical cases, $J_\phi^0(k)$ is significant over the range $0 < k \lesssim 2\pi/a$. Thus, provided z^2/a^2 is much smaller than unity, $\sin kz$ and $\cos kz$ can be replaced by kz and $1 - (kz)^2/2$, respectively. In that case, from Eq. (3.39), the field gradient produced by the shielded gradient set, when the primary coil current is $J_\phi^0(k)$, is given by

$$\begin{aligned}
G_z &= B_z(z)/z \\
&= \frac{i\mu_0 a}{\pi}\int_0^\infty k^2\, dk\, J_\phi^0(k)K_1(ka)(1 - S_0). \tag{3.50}
\end{aligned}$$

Moreover, the initial amplitude of the eddy current field, caused by switching on $J_\phi^0(k)$, is of the form

$$B_z^{\text{eddy}}(z) \simeq P\left[1 - \eta\left(\frac{z}{a}\right)^2\right], \tag{3.51}$$

where the homogeneous part of the eddy current field, P, is given by

$$P = \frac{i\mu_0 a}{\pi}\Delta z \int_0^\infty k^2 dk\, J_\phi^0(k)K_1(kc)\frac{I_1(ka)}{I_1(kc)}, \tag{3.52}$$

and the dimensionless inhomogeneity factor, η, is given by

$$\eta = \frac{a^2 \int_0^\infty k^4 dk\, J_\phi^0(k)K_1(kc)I_1(ka)/I_1(kc)}{2\int_0^\infty k^2 dk\, J_\phi^0(k)K_1(kc)I_1(ka)/I_1(kc)}. \tag{3.53}$$

The $\eta(z/a)^2$ term in Eq. (3.51) will usually be unimportant, so that the predominant effect of displacing the primary coil along the z axis from its correct position is to generate a fairly uniform "B_0 shift". In most of what follows, we shall neglect the z dependence of $B_z^{\text{eddy}}(z)$ but will need to take its time dependence into account.

Accordingly, we shall characterize the seriousness of the misregistration by the initial amplitude of the eddy current field, which we shall denote by $(B_z^{\text{eddy}})_0$, caused by switching *on* the gradient field. It follows from Eqs. (3.50) – (3.52) that

$$(B_z^{\text{eddy}})_0 = RG_z\Delta z, \tag{3.54}$$

where

$$R = \frac{\int_0^\infty k^2 dk\, J_\phi^0(k) K_1(kc) I_1(ka)/I_1(kc)}{\int_0^\infty k^2 dk\, J_\phi^0(k) K_1(ka)(1 - S_0)}. \tag{3.55}$$

The ratio R depends upon the design of the shielded gradient set, and, for any particular design, upon the ratios b/a and c/a. However, it is independent of the scale of the gradient coils and the surrounding conducting cylinder.

3.3 Application to Some Imaging Protocols

For imaging sequences based on the two-dimensional Fourier transform method [15], it is necessary to consider separately the switching of the slice selection, phase encoding, and frequency encoding or read gradients, G_{slice}, G_{phase} and G_{read}, respectively, as their effects are different. In each case, the artifact caused by the gradient switching is determined by the *change* in the eddy current field, denoted by δB_z^{eddy}, which occurs during a particular time interval. However, δB_z^{eddy} is linearly dependent upon $(B_z^{\text{eddy}})_0$, the initial amplitude of the eddy current field caused by switching on the z gradient, so that one can write

$$\delta B_z^{\text{eddy}} = \alpha (B_z^{\text{eddy}})_0. \tag{3.56}$$

The parameter α will naturally depend upon the pulse sequence being considered. However, it will also depend upon the role played by G_z in that sequence, *i.e.*, whether G_z is the slice selection, the phase encoding, or the read gradient.

For simplicity, we shall assume, in what follows, that the switching of G_z is instantaneous. Derivation of the expressions for α in the rest of this chapter is given in Appendix A.

3.3.1 Effect of the Eddy Current Field Caused by Switching G_{slice}

The eddy current field generated during slice selection by the switching of G_{slice}, i.e., G_z, will not only affect the slice selection but will also affect processes occurring at later times due to the slow decay of the eddy current field. The effect on slice selection will be to displace the slice from its "true" position while at the same time modifying its profile. Because of the *decaying*, homogeneous eddy current field, the slice will be thicker than the desired one, but spins near the two faces of the slice will not be fully excited. Thus, the slice profile will be broader at the bottom and narrower at the top. In many applications, a small displacement of the slice is not a serious problem. However, changing the profile of the slice constitutes a real artifact. We shall suppose that $(\delta B_z^{\text{eddy}})_{\text{max}}$, the maximum tolerable change in the eddy current field during slice selection, is a fraction β of the width of the slice, expressed in field units, so that

$$(\delta B_z^{\text{eddy}})_{\text{max}} = \beta G_z(\text{slice thickness}). \tag{3.57}$$

It follows from Eqs. (3.54), (3.56), and (3.57) that $(\Delta z)_{\text{max}}$, the maximum allowable misregistration of the primary and shielding coils in a shielded gradient set, is given by

$$(\Delta z)_{\text{max}} = (\beta/\alpha)\frac{(\text{slice thickness})}{R}, \tag{3.58}$$

where

$$\alpha = 1 - e^{-\tau_{\text{slice}}/\tau}, \tag{3.59}$$

τ_{slice} is the duration of the slice selection gradient, and τ is the decay time of the eddy current. Since the inhomogeneity in the eddy current field is small in most practical cases, the eddy current field which is present during the refocussing interval of the slice selection gradient, will have little effect upon the refocussing.

In considering artifacts in the phase encoding direction, associated with eddy currents generated by G_{slice}, it is important to distinguish between multishot and

single-shot imaging techniques. In multishot imaging where phase encoding is achieved by incrementally changing the amplitude of the gradient pulse between each shot [16], the eddy current field generated by the slice selection gradient has no consequence, since the phase shift due to the eddy current field is the same in each "shot". However, in "single shot" imaging such as echo planar, where the time dependent phase shift imposed by the slice selection gradient is sampled sequentially at different times, the phase shift is different at each sampling.

Consider, for example, the MBEST version of echo-planar imaging [17], whose pulse timing diagram is shown in Fig. 3.1a. If we postulate that $(\delta B_z^{\text{eddy}})_{\text{max}}$, the maximum allowable change in the eddy current field, which occurs during the entire acquisition period due to switching G_{slice}, is equal to the field increment corresponding to the digital resolution in the phase encoding direction, then

$$(\delta B_z^{\text{eddy}})_{\text{max}} = \frac{G_{\text{phase}} L_{\text{phase}} \tau_3}{\mathcal{N}_{\text{phase}} \tau_2}, \tag{3.60}$$

where τ_3 and G_{phase} are, respectively, the duration and amplitude of each gradient blip, and L_{phase} and $\mathcal{N}_{\text{phase}}$ are, respectively, the field of view (FOV) and the number of sampled points, in the phase encoding direction. Also, τ_2 is the duration of each read gradient pulse. It follows from Eqs. (3.54), (3.56), and (3.60) that the maximum allowable misregistration of the primary and shielding coils is given by

$$(\Delta z)_{\text{max}} = \frac{G_{\text{phase}} L_{\text{phase}} \tau_3}{\mathcal{N}_{\text{phase}} R |\alpha| G_{\text{slice}} \tau_2}, \tag{3.61}$$

where α is in this case given by [18]

$$\alpha = \left(1 + e^{-3\tau_{\text{slice}}/2\tau} - 2e^{-\tau_{\text{slice}}/2\tau}\right)\left(1 - e^{-n\tau_2/\tau}\right) e^{-[\tau_1 + (\tau_2/2)]/\tau} \tag{3.62}$$

and n ($= \mathcal{N}_{\text{phase}}$) is the total number of echoes. Here τ_1 is the duration of the prepulse in the phase encoding direction.

The artifact in the frequency encoding direction, caused by switching G_{slice}, is much smaller than that caused by switching either G_{phase} or G_{read} and will therefore be neglected.

49
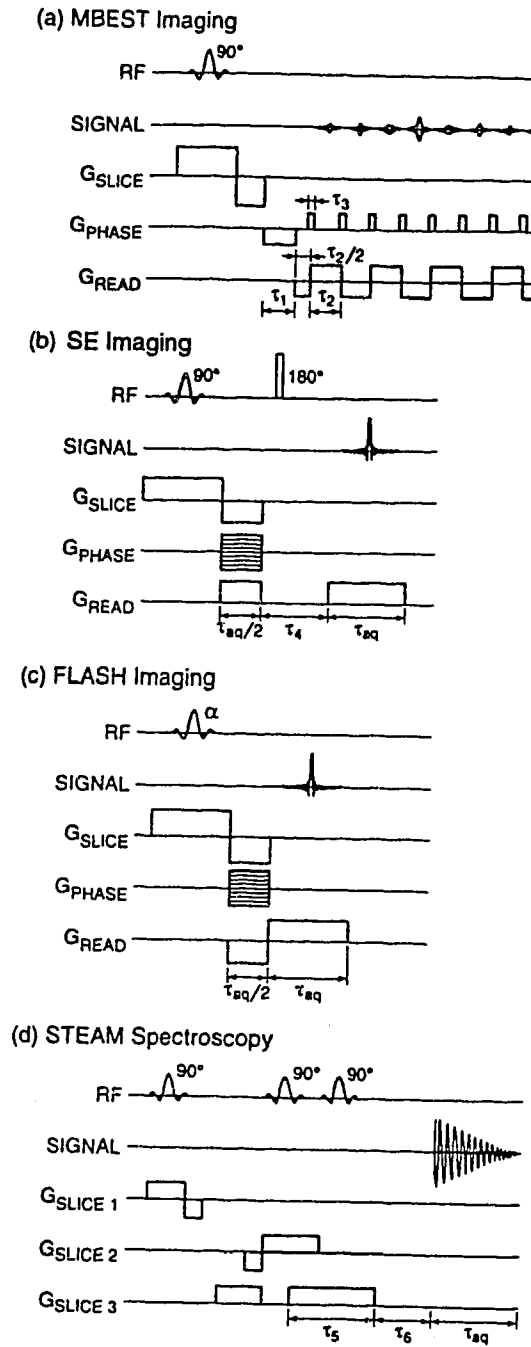
Figure 3.1: Pulse timing diagram for (a) MBEST imaging, (b) SE imaging, (c) FLASH imaging, and (d) STEAM spectroscopy. In (c), α denotes a small flip angle.

3.3.2 Effect of the Eddy Current Field Caused by Switching G_{phase}

In multishot imaging where the amplitude of G_{phase} is incremented, the eddy current field caused by switching G_{phase} has no effect in the phase encoding direction, other than to shift the image, because the eddy current field itself is incremented in proportion to G_{phase}. On the other hand, in MBEST imaging, the same criterion as before, namely that δB_z^{eddy} is equal to the field increment corresponding to the digital resolution in the phase encoding direction, leads to

$$(\Delta z)_{\max} = \frac{L_{\text{phase}}\tau_3}{\mathcal{N}_{\text{phase}}R|\alpha|\tau_2}.$$ (3.63)

Here α is given by

$$\alpha = \left[\left(1 - e^{-\tau_1/\tau}\right)u^{1/2} - \frac{\tau_3}{\tau}\right](1 - u^n) + \frac{\tau_3 u\left(1 - u^{n-1}\right)}{\tau(1 - u)},$$ (3.64)

where $u = \exp\left(-\tau_2/\tau\right)$. In deriving Eq. (3.64), it has been assumed that $\tau_3/\tau \ll 1$, and that the prepulse and the blips comprising G_{phase} all possess the same amplitude.

The artifact in the frequency encoding direction, caused by switching G_{phase}, is much smaller than that caused by switching G_{read} and will therefore be neglected.

3.3.3 Effect of the Eddy Current Field Caused by Switching G_{read}

The maximum tolerable misregistration of the primary and shielding coils, governed by the acceptability of artifacts generated by the switching of G_{read}, is given by

$$(\Delta z)_{\max} = \frac{L_{\text{read}}}{\mathcal{N}_{\text{read}}|\alpha|R},$$ (3.65)

when δB_z^{eddy} during the (read) acquisition period is set equal to the field increment corresponding to the digital resolution in the frequency encoding direction. In Eq. (3.65), L_{read} and $\mathcal{N}_{\text{read}}$ are the FOV and the number of sampled points, respectively. For spin-echo (SE) imaging, a multishot technique whose pulse timing

diagram is shown in Fig. 3.1b, α in Eq. (3.65) is given by

$$\alpha = \left[1 - \left(1 - e^{-\tau_{aq}/2\tau}\right)e^{-\tau_4/\tau}\right]\left(1 - e^{-\tau_{aq}/\tau}\right), \tag{3.66}$$

where τ_{aq} is the duration of the read gradient pulse, and τ_4 is the interval between switch-off of the read compensation gradient and switch-on of the read gradient. For FLASH imaging [19], which is an example of a rapid-scan multishot technique and whose pulse timing diagram is shown in Fig. 3.1c, α is given by

$$\alpha = \left(2 - e^{-\tau_{aq}/2\tau}\right)\left(1 - e^{-\tau_{aq}/\tau}\right). \tag{3.67}$$

For MBEST imaging, α, characteristic of δB_z^{eddy} during the first echo, is $[2 - \exp\left(-\tau_2/2\tau\right)][1 - \exp\left(-\tau_2/\tau\right)]$. However, a more appropriate expression is

$$\alpha = \frac{2\left(1 - e^{-\tau_2/\tau}\right)}{1 + e^{-\tau_2/\tau}}, \tag{3.68}$$

which is characteristic of δB_z^{eddy} during each of the later echoes when a "steady state" has been achieved.

3.3.4 Numerical Estimates of $(\Delta z)_{\text{max}}$

The above relations were applied to two different shielded z gradient systems, whose dimensions, a, b, and c, together with their ratios b/a and c/a, are listed in Table 3.1. System 1, installed in a 40 cm bore, 2.35 T Bruker magnet, is a shielded gradient set of minimum inductance design [6], which was constructed using discrete wires in our machine shop. The value of c was taken to be 0.22 m, the radius of the first (i.e. closest to the sample space) cryogenic shield in the magnet (Bruker Canada, private communication). System 2 is based on the 1.5 T, whole-body GE magnet that is widely used in clinical MRI studies. Here, again, c ($= 0.49$ m) was taken to be the radius of the first (80 K) cryogenic shield (GE Medical Systems, private communication). The values of a and b, used in the whole body case, were the same

Table 3.1: Values and ratios of a, b, and c which characterize the two shielded gradient systems considered in the text[a]

System	Magnet	a (m)	b (m)	c (m)	b/a	c/a	R
1	2.35 T 40 cm bore Bruker	0.13 m	0.17 m	0.22 m	1.31	1.69	0.288
2	1.5 T whole-body GE	0.30 m	0.42 m	0.49 m	1.40	1.62	0.294

[a]Also shown are the corresponding values of R derived using Eq. (3.55).

as those employed in some shielded gradient sets supplied by GE for their 1.5 T magnets. For purposes of calculation, we assumed that the current distribution in the primary coil of System 2 was an appropriately scaled version of that of System 1.

It is first necessary to evaluate R using Eq. (3.55). Since the current is carried by discrete wires, at known locations $\pm z_j'$, $J_\phi(z')$ is given by

$$J_\phi(z') = \sum_{j=1}^{N} I \left[\delta(z' - z_j') - \delta(z' + z_j') \right], \tag{3.69}$$

where I is the magnitude of the current flowing in each turn and N is the number of turns in each half of the coil. It therefore follows from Eq. (3.38) that

$$J_\phi^0(k) = -2iI \sum_{j=1}^{N} \sin k z_j'. \tag{3.70}$$

By evaluating the integrals in Eq. (3.55) with the aid of Eq. (3.70) and as a function of c/a, the graphs shown in Fig. 3.2 were obtained for Systems 1 and 2. As expected, R falls off rapidly with increasing values of c/a, i.e. with increasing radius of the conducting cylinder in which the eddy current is induced. The two dots on the curves locate the parameters of the two systems being considered, the values of
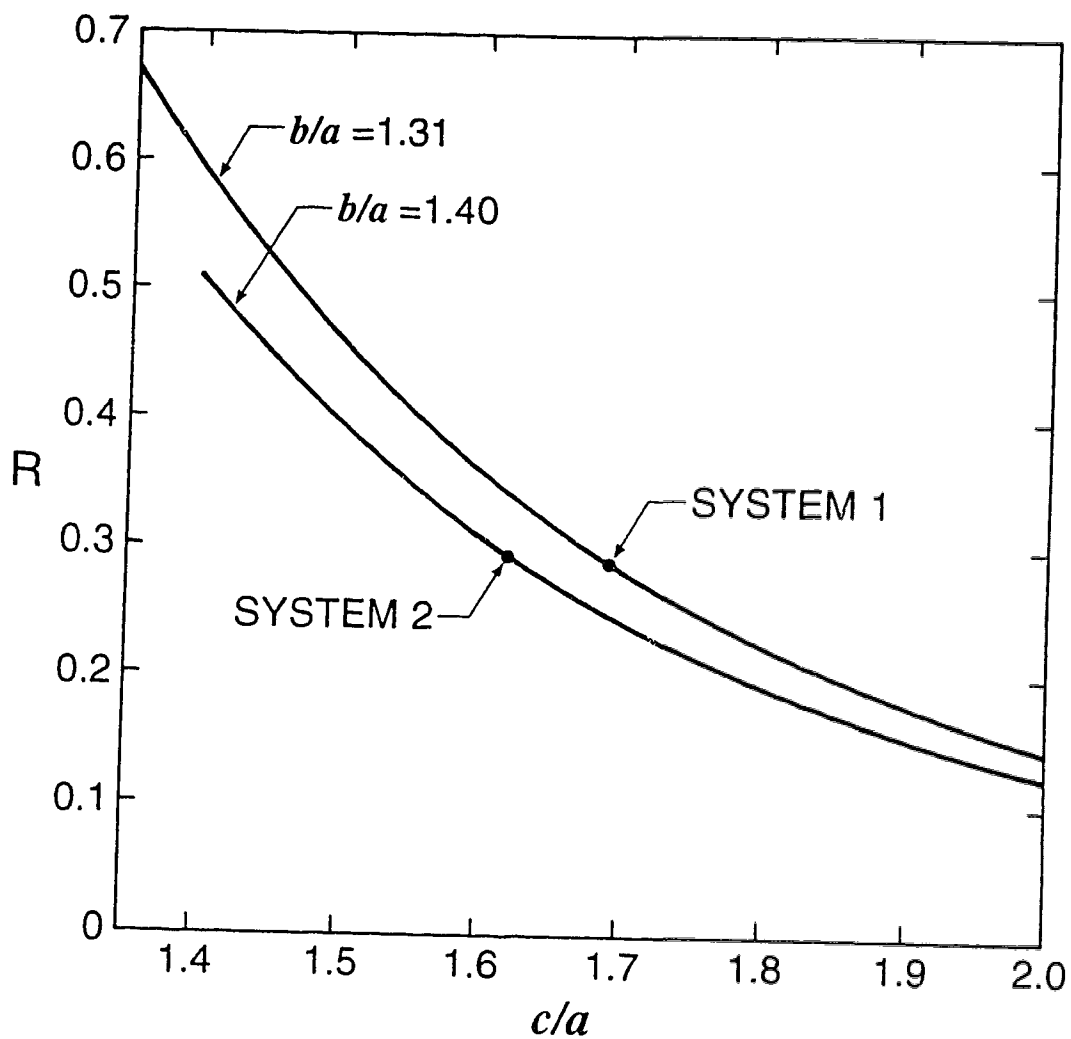
Figure 3.2: The ratio R, defined in Eq. (3.55), plotted as a function of c/a for $b/a = 1.31$ and 1.40. The two solid circles refer to Systems 1 and 2, described in the text.

R being given in Table 3.1. Because of the competing demands of high coil efficiency and large usable sample volumes, the b/a ratio of most shielded gradient sets used in MRI is likely to lie between the two examples chosen, namely 1.31 and 1.40. Since R varies relatively little with b/a in the range $b/a = 1.31$ to 1.40, for a given c/a, an approximate value of R for shielded gradient sets of minimum inductance design with values of b/a in this range, can be found by linear interpolation between the two curves in Fig. 3.2.

In order to determine values of $(\Delta z)_{max}$ for the SE, FLASH, and MBEST protocols, we used the typical experimental parameters listed in Table 3.2. (The timings for MBEST are similar to those given in Ref. [17].) The effect of the eddy current field generated by a switched gradient depends very strongly on the decay time τ of the eddy current. Analysis of the eddy current fields generated by switching the z gradient in our 40 cm bore 2.35 T Bruker magnet showed three distinct eddy currents with decay times of (13.8 ± 2.5) ms, (70 ± 5) ms, and (362 ± 5) ms [13]. Decay times of 17.5 ms, 29.7 ms, and 267 ms were found by Jehenson *et al.* [12] in a 60 cm bore 3 T Bruker magnet. Since the decay time of an eddy current induced in a shield depends on parameters which vary with magnet design such as the thickness, temperature, and material composing the shield, we consider two values of τ, namely 10 ms and 100 ms. These values are representative of a rapidly decaying and a slowly decaying eddy current, respectively.

We first consider System 1, which is characterized by $R = 0.288$. The value of $(\Delta z)_{max}$, corresponding to the slice-profile artifact caused by the slice selection gradient, is found by first determining α using Eq. (3.59). For an eddy current with $\tau = 10$ ms, α is 0.375. If β is assumed to be 0.1, implying that the maximum tolerable value of δB_z^{eddy} during the slice selection period is 10% of the typical slice thickness expressed in field units, then Eq. (3.58) yields $(\Delta z)_{max} = 1.9$ mm. If τ is taken to be 100 ms, α is 0.046, giving $(\Delta z)_{max} = 15$ mm. These values of $(\Delta z)_{max}$,

Table 3.2: Parameters used to calculate $(\Delta z)_{max}$ for System 1 using SE, FLASH and MBEST[a]

(a) SE[b]

$G_{slice} = 1$ G/cm, $\tau_{slice} = 4.7$ ms, Slice Thickness $= 2$ mm.

$G_{read} = 1$ G/cm, $L_{read} = 10$ cm, $\mathcal{N}_{read} = 256$, $\tau_{aq} = 6$ ms, $\tau_4 = 5$ ms.

(b) FLASH[b]

Same slice selection parameters as in SE

$G_{read} = 1$ G/cm, $L_{read} = 10$ cm, $\mathcal{N}_{read} = 256$, $\tau_{aq} = 4$ ms.

(c) MBEST

Same slice selection parameters as in SE

$G_{phase} = 0.23$ G/cm, $L_{phase} = 10$ cm, $\mathcal{N}_{phase} = n = 64$.

$G_{read} = 2.3$ G/cm, $L_{read} = 10$ cm, $\mathcal{N}_{read} = 128$, $\tau_1 = 3.2$ ms,

$\tau_2 = 1.0$ ms, $\tau_3 = 0.1$ ms

---

[a]The parameters used for System 2 are the same, except that L_{phase} and L_{read} are 20 cm, the slice thickness is 4 mm, and G_{slice}, G_{phase} and G_{read} are reduced by a factor of two.

[b]Parameters for the phase encoding gradient are not required for SE and FLASH.

which are listed in Table 3.3, are characteristic of all three protocols, SE, FLASH, and MBEST, since the same slice selection pulse sequence is assumed in each case.

Values of $(\Delta z)_{max}$, associated with artifacts in the phase encoding and frequency encoding directions, caused by switching each of the three gradients, are found in a similar manner and are listed in Table 3.3. Where there are no entries, the artifact is either negligible, corresponding to a very large value of $(\Delta z)_{max}$, or totally absent as in the case of the phase encoding direction when switching G_{slice} or G_{phase} in the multishot protocols.

It is evident from Table 3.3 that an eddy current with $\tau = 10$ ms requires much more accurate shielding, and hence registration of the primary and shielding coils, than does an eddy current with $\tau = 100$ ms. This is because τ_{slice}, τ_{phase}, and τ_{aq} are all ~ 10 ms. If $\tau \sim 100$ ms, there is substantial cancellation of the eddy current fields generated by the switch-on and switch-off of the gradient pulses.

For System 2, we take the FOV and the slice thickness to be a factor of two larger than the values used for System 1 (see Table 3.2). The gradient amplitudes are assumed to be a factor of two smaller than those used for System 1, thereby maintaining the same timings and hence the same values of α as before. Since R for System 2 is, coincidentally, almost the same as that for System 1, it follows that the $(\Delta z)_{max}$ values for System 2 are approximately a factor of two larger than for System 1. They are therefore not listed.

3.4   Application to Proton Spectroscopy

To illustrate the effect of a misregistration of the primary and shielding coils in the proton spectroscopy of uncoupled spins, we consider the stimulated echo (STEAM) spectroscopy sequence [20] in which volume selection is achieved by applying three selective 90° pulses successively in the presence of each of three orthogonal gradients,

Table 3.3: Values of $(\Delta z)_{max}$, evaluated for System 1 and for two different values of τ, the decay time of the eddy current, for the imaging protocols considered in the text[a]

Switched Gradient	Artifact Direction	Protocol	τ (ms)	$(\Delta z)_{max}$ (mm)
G_{slice}	Slice	All	10	1.9
			100	15
G_{slice}	Phase	MBEST	10	2.1
			100	13
G_{phase}	Phase	MBEST	10	1.5
			100	8.8
G_{read}	Read	SE	10	3.6
			100	24
G_{read}	Read	FLASH	10	3.5
			100	34
G_{read}	Read	MBEST	10	27

[a]Values of $(\Delta z)_{max}$ for System 2 are approximately a factor of two larger than those shown for System 1.

as shown in Fig. 3.1d.

Since the three slice selection gradients are usually of equal amplitude, we shall only consider the effect of the second G_{slice3} pulse which we shall assume to be G_z. It follows from Eqs. (3.54) and (3.56) that

$$(\Delta z)_{\text{max}} = \frac{(\delta B_z^{\text{eddy}})_{\text{max}}}{R|\alpha|G_z}. \tag{3.71}$$

The eddy current field caused by the second G_{slice3} pulse will almost completely decay during the data acquisition period, since acquisition is usually of the order of several hundred milliseconds. Thus, α in Eq. (3.71) is given by

$$\alpha = \left(1 - e^{-\tau_5/\tau}\right) e^{-\tau_6/\tau}, \tag{3.72}$$

where τ_5 is the duration of the second G_{slice3} pulse, and τ_6 is the interval between the switch-off of the second G_{slice3} pulse and the beginning of acquisition.

A reasonable value for $(\delta B_z^{\text{eddy}})_{\text{max}}$ in $in\ vivo$ proton spectroscopy is 3 Hz or 7×10^{-4} G, the smallest linewidth observed in studies of the brain [21]. By taking typical values $G_z = 1$ G/cm for the excitation of a small, $1 \times 1 \times 1$ cm, VOI in System 1 and $G_z = 0.5$ G/cm for the excitation of a small, $2 \times 2 \times 2$ cm, VOI in System 2, with $\tau_5 = 20$ ms and $\tau_6 = 15$ ms in both cases, it is found that $\alpha = 0.19$ for $\tau = 10$ ms and 0.16 for $\tau = 100$ ms. Substituting values of $(\delta B_z^{\text{eddy}})_{\text{max}}$, G_z, α, and R in Eq. (3.71) yields $(\Delta z)_{\text{max}}$ for System 1 equal to 0.13 mm for $\tau = 10$ ms, and 0.16 mm for $\tau = 100$ ms. For System 2, the values of $(\Delta z)_{\text{max}}$ are essentially twice as large, reflecting the difference in the dimensions of the VOI. It should be noted that, in contrast to the imaging situation, the tolerances are roughly similar for eddy currents with short and long decay times. This is because of the long acquisition times and gradient pulses used in proton spectroscopy.

Ordidge and Cresshull proposed a correction method for a time-dependent change in the homogeneous component of the eddy current field by phase correction

59

in the time domain [3]. Firstly, the phase of an on-resonance signal from a sample of single resonance, such as water, is measured as it evolves following a gradient pulse sequence. This phase evolution is then subtracted from all subsequent time domain signals obtained by the use of the same sequence in order to remove the effect of homogeneous eddy current fields. However, even if the eddy current field effect is reduced by an order of magnitude by this means, it is evident that an accuracy of about 1 mm is still required in assembling a z gradient set for System 1. For System 2, the required accuracy would be about 2 mm.

If the homogeneous component of the eddy current field could be totally eliminated by a correction method, an artifact would still be caused by the inhomogeneous component, represented by the $\eta(z/a)^2$ term in Eq. (3.51). Evaluation of the integrals in Eq. (3.53) shows that $\eta = 0.565$ and 0.573 for Systems 1 and 2, respectively, so that the inhomogeneous component is almost the same in both cases, for equal values of z/a. For an assumed worst case scenario of chemical shift imaging over a region extending from $z/a = -0.25$ to $z/a = 0.25$, the inhomogeneous component of the eddy current field is 3.6% of the uncorrected homogeneous component for each system. Thus, the inhomogeneous component of the eddy current field, if uncompensated, would require $(\Delta z)_{max}$ to be $0.13/0.036 \sim 3.5$ mm for $\tau = 10$ ms and $0.16/0.036 \sim 4.4$ mm for $\tau = 100$ ms, in System 1. In System 2, the values of $(\Delta z)_{max}$ would be twice as large.

We have confined ourselves here to considering the STEAM spectroscopy sequence. However, similar results are obtained for the PRESS [22] and ISIS [23] sequences.

3.5   Summary

The demands of *in vivo* proton spectroscopy require tolerances of order 0.1 mm in the assembly and, by inference, the construction of shielded z gradient sets for

both animal-size and whole-body-size magnet systems. Corresponding tolerances for systems to be used for SE, FLASH, and MBEST imaging are more modest, being roughly 1 mm if the eddy currents have decay times of the same order as the duration of the gradient pulses. If the eddy currents have much longer decay times, the tolerances are significantly relaxed.

We note that a z gradient set can be aligned in the z direction by, for example, plotting the fields generated by the primary and shielding coils separately as a function of z, and ensuring that the centers of the two gradient fields coincide. However, alignment to better than about 1 mm may not be easy to achieve in practice.

References

[1] R.M. Henkelman and M.J. Bronskill, *Rev. Magn. Reson. Med.* **2**, 1 (1987).

[2] D.G. Hughes, S. Robertson, and P.S. Allen, *Magn. Reson. Med.* **25**, 167 (1992).

[3] R.J. Ordidge and I.D. Cresshull, *J. Magn. Reson.* **69**, 151 (1986).

[4] U. Klose, *Magn. Reson. Med.* **14**, 26 (1990).

[5] P. Mansfield and B. Chapman, *J. Phys. E: Sci. Instrum.* **19**, 540 (1986).

[6] R. Turner, *J. Phys. E: Sci. Instrum.* **21**, 948 (1988).

[7] R. Turner and R.M. Bowley, *J. Phys. E: Sci. Instrum.* **19**, 876 (1986).

[8] J.D. Jackson, "Classical Electrodynamics," Wiley, New York, 1962.

[9] Q. Liu, M.Sc. Thesis, University of Alberta, 1991.

[10] F.W.J. Olver, *in* "Handbook of Mathematical Functions" (M. Abramowitz and I.A. Stegun, eds.), p. 355, Dover, New York, 1972.

[11] T.H. Mareci, private communication, 1986.

[12] P. Jehenson, M. Westphal, and N. Schuff, *J. Magn. Reson.* **90**, 264 (1990).

[13] Q. Liu, D.G. Hughes, and P.S. Allen, *Magn. Reson. Med.* **31**, 73 (1994).

[14] P. Mansfield and I.L. Pykett, J. Magn. Reson. **29**, 355 (1978).

[15] A. Kumar, D. Welti, and R.R. Ernst, *J. Magn. Reson.* **18**, 69 (1975).

[16] W.A. Edelstein, J.M.S. Hutchison, G. Johnson, and T.W. Redpath, *Phys. Med. Biol.* **25**, 751 (1980).

[17] M.J. Stehling, A.M. Howseman, R.J. Ordidge, B. Chapman, R. Turner, R. Coxon, P. Glover, P. Mansfield, and R.E. Coupland, *Radiology* **170**, 257 (1989).

[18] S. Robertson, D.G. Hughes, Q. Liu, and P.S. Allen, *Magn. Reson. Med.* **25**, 158 (1992).

[19] J. Frahm, A. Haase, and D. Matthaei, *Magn. Reson. Med.* **3**, 321 (1986).

[20] J. Frahm, K.R. Merboldt, and W. Hanicke, *J. Magn. Reson.* **72**, 508 (1987).

[21] R. Kreis, T. Ernst, and B.D. Ross, *J. Magn. Reson. B* **102**, 9 (1993).

[22] R.E. Gordon and R.J. Ordidge, Proceedings, 3rd Annual Meeting, Society of Magnetic Resonance in Medicine, 1984, New York, p.272.

[23] R.J. Ordidge, A. Connelly, and J.A.B. Lohman, *J. Magn. Reson.* **66**, 283 (1986).

Chapter Four

DESIGN AND CONSTRUCTION OF A LOW POWER DISSIPATION, CYLINDRICAL Z^4 SHIM COIL FOR A WIDE BORE NMR MAGNET[1]

4.1   Introduction

An important feature of superconducting solenoids used for NMR is the compensation of the variation of the magnetic field strength in the z direction, arising from the "end effects" associated with the finite length of the solenoid. Such compensation is in practice imperfect, so that shim coils, either superconducting or room temperature, are required to cancel the remaining variation in the z direction. Shim coils are also required to compensate the field variations in the transverse directions, though these are expected to be smaller.

The variation of the field strength in the transverse directions in our 40 cm bore Bruker magnet of 1984 vintage could be quite accurately compensated using low order shims (cf. Refs. [1, 2]) with a power dissipation of roughly five watts. In sharp contrast, the axial variation, which is predominantly fourth order in the z coordinate, could only be one-third compensated using the z^4 shim coil provided by the manufacturer, the associated power dissipation being about 100 watts leading to temperature increases in the sample space of up to 12°C in one hour, depending upon the equipment located therein. This defect seems to be shared by several other animal-size magnets manufactured during the 1980s.

To overcome the problem, we designed and constructed a replacement z^4 shim coil which allows full compensation of the z^4 field variation with a power dissipation of only 21 watts. The reduced power dissipation can be partly attributed to the smaller size of the replacement shim coil. However, a significant reduction stems from the design of the coil itself.

Romeo and Hoult [3] have proposed a z^4 shim coil design. However, they did not consider factors which affect the power dissipation. In this chapter, we shall show how various design parameters affect the power dissipation and field profile accuracy of z^4 shim coils wound on a cylindrical former. While such shim coils could be designed using the distributed current, target field approach [4], our discussion is restricted to simpler configurations based on a small number of current-carrying rings, along the lines pioneered by Golay [5] and developed by others [3, 6]. We first consider the design characteristics of z^4 shim coils which generate no z^0 (field shift) and z^2 components, calling this type of shim coil Type 1. However, because of their lower power consumption, we also consider z^4 shim coils, called Type 2, which generate no z^2 and z^6 components but can generate a significant z^0 component.

4.2 Theoretical Considerations

4.2.1 Design of Type 1, z^4 Shim Coils for Which the z^0, z^2, and All Odd Power Terms Are Zero

The magnetic field at a point z on the axis of a circular ring of radius a, situated at z_1 and carrying a current I_1, is given by

$$B_z(z) = \frac{\mu_0 I_1}{2a} \left[1 + \left(\frac{z - z_1}{a} \right)^2 \right]^{-3/2}. \tag{4.1}$$

A pair of such rings, located at $z = \pm z_1$ and carrying identical currents I_1, would generate an axial field, all of whose odd derivatives are zero at the origin [3]. To

64

obtain an axial field satisfying the conditions

$$(B_z)_{z=0} = 0 \tag{4.2}$$

$$\left(d^2 B_z/dz^2\right)_{z=0} = 0 \tag{4.3}$$

which imply that the z^0 and z^2 terms are zero, an additional pair of rings of radius a with z coordinates of $\pm z_2$, say, is required, each carrying identical currents I_2. The magnetic field on the z axis generated by the two pairs of current rings is given by

$$B_z(z) = \frac{\mu_0}{2a} \left\{ \frac{I_1}{\left[1 + (z - z_1)^2/a^2\right]^{3/2}} + \frac{I_1}{\left[1 + (z + z_1)^2/a^2\right]^{3/2}} \right. $$
$$\left. + \frac{I_2}{\left[1 + (z - z_2)^2/a^2\right]^{3/2}} + \frac{I_2}{\left[1 + (z + z_2)^2/a^2\right]^{3/2}} \right\}. \tag{4.4}$$

Substituting Eq. (4.4) into Eqs. (4.2) and (4.3) yields

$$\frac{1}{[1 + (z_1/a)^2]^{3/2}} I_1 + \frac{1}{[1 + (z_2/a)^2]^{3/2}} I_2 = 0 \tag{4.5}$$

$$\frac{1 - 4(z_1/a)^2}{[1 + (z_1/a)^2]^{7/2}} I_1 + \frac{1 - 4(z_2/a)^2}{[1 + (z_2/a)^2]^{7/2}} I_2 = 0. \tag{4.6}$$

Each of Eqs. (4.5) and (4.6) gives rise to an independent condition on I_2/I_1, which if simultaneously applied, can be solved to give the following relations between design parameters:

$$z_2/a = \left[\frac{(z_1/a)^2 + 6}{4(z_1/a)^2 - 1} \right]^{1/2} \tag{4.7}$$

$$z_1/a = \frac{1}{2} \left[5 (I_1/I_2)^{2/3} + 1 \right]^{1/2} \tag{4.8}$$

$$z_2/a = \frac{1}{2} \left[5 (I_2/I_1)^{2/3} + 1 \right]^{1/2}. \tag{4.9}$$

The relation between z_1/a and z_2/a, i.e. Eq. (4.7), is plotted as a broken curve in Fig. 4.1, together with representative values of I_2/I_1. The curve is symmetric
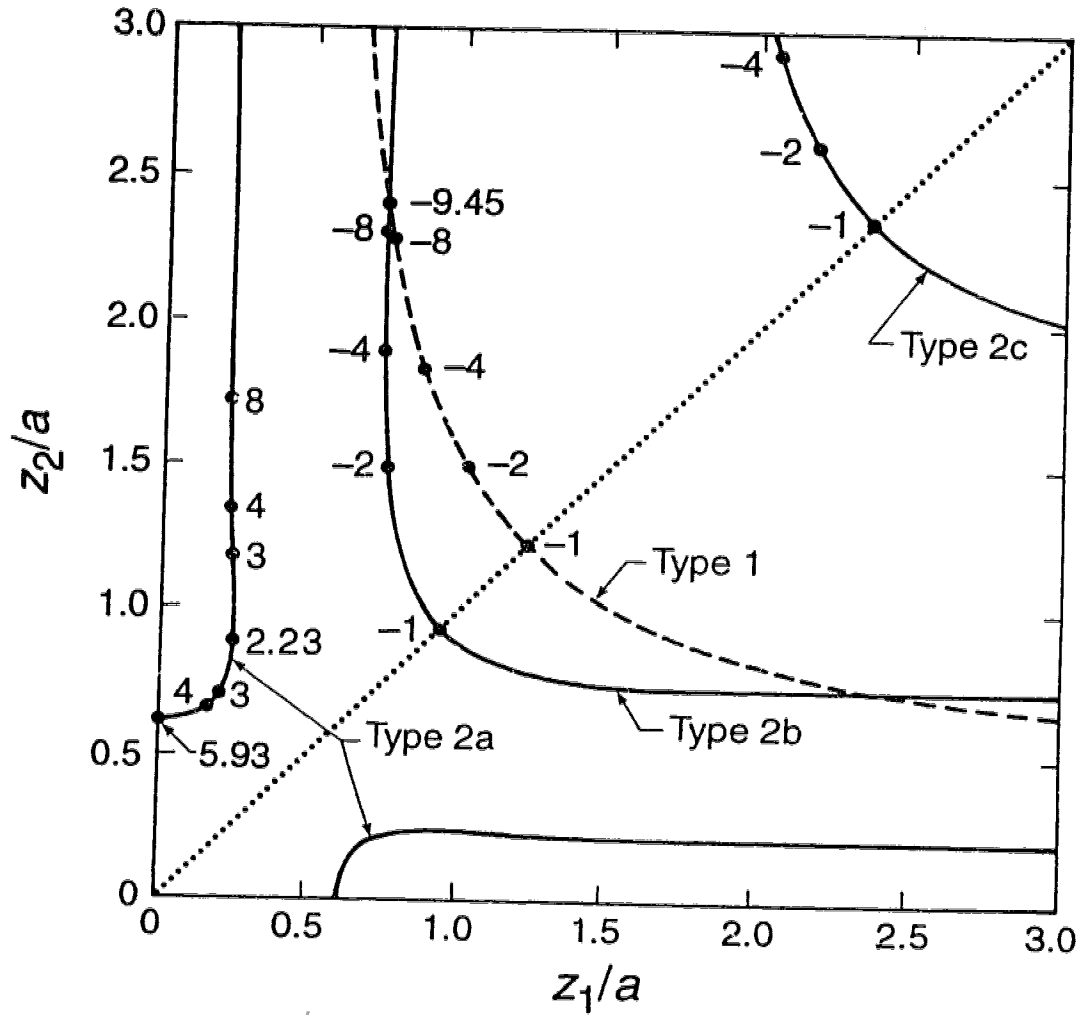
Figure 4.1: The broken curve shows conjugate values of z_1/a and z_2/a for Type 1, z^4 shim coils, *i.e.* those which generate no z^0 and z^2 components. The solid curves, denoted by Type 2a, 2b, and 2c, show conjugate values of z_1/a and z_2/a for Type 2, z^4 shim coils, *i.e.* those which generate no z^2 and z^6 components. The points and associated numbers show some representative values of I_2/I_1. The graph is symmetric about the diagonal dotted line for which $z_1/a = z_2/a$.

about the dotted line representing $z_1/a = z_2/a$ and possesses two asymptotes at $z_1/a = 0.5$ and $z_2/a = 0.5$.

It is evident from Eq. (4.7) that a symmetrical three-ring arrangement, e.g. one in which $z_1 = 0$, gives rise to an imaginary solution and is therefore not tenable. Thus, the minimum number of rings for a Type 1 shim coil is four, a result which is at variance with Romeo and Hoult's assertion [3] that systems which provide a variation as z^p in B_z (while all lower orders are zero) comprise $(p + 1)$ rings.

A design which satisfies the condition

$$I_2/I_1 \simeq -n_2/n_1, \tag{4.10}$$

where n_1 and n_2 are small, positive, even integers can be conveniently implemented by winding two pairs of coils at $\pm z_1$ and $\pm z_2$, with each pair consisting of n_1 and n_2 turns, respectively. A z^4 shim field will be generated by passing the same current I, say, through the two pairs of coils, connected in series opposition so as to accommodate the negative sign in Eq. (4.10).

In order to compare the power dissipation of z^4 shim coils of different design, it is necessary to identify the parameters which govern the power dissipation of a z^4 shim coil of *given* design, *i.e.* characterized by particular values of I_2/I_1, z_1/a, and z_2/a. We first consider the effect of scaling the linear dimensions of the coil, as well as the wire (including its diameter) comprising it, by a factor λ, say. The z^4 field generated by a given current is scaled by a factor λ^{-5} [3]. Thus, to obtain the same z^4 field, the current I would have to be scaled by a factor λ^5. However, since the coil resistance R would scale as λ^{-1}, the power dissipated, I^2R, in generating a particular z^4 field would scale as λ^9, a very strong dependence.

For a four-coil z^4 shim coil, the power dissipation is given in terms of the current I flowing in the coil, by

$$P = \frac{2\pi a \rho}{A} \left(n_1 + n_2\right) I^2, \tag{4.11}$$

where ρ and A are, respectively, the resistivity and cross-sectional area of the wire, and where the resistance of the leads and interconnections has been neglected. By introducing the total or integrated cross-sectional area of all the turns of wire given by

$$A_{tot} = (n_1 + n_2) A, \qquad (4.12)$$

Eq. (4.11) can be rewritten as

$$P = \frac{2\pi a \rho}{A_{tot}} \left[(n_1 + n_2) I \right]^2, \qquad (4.13)$$

where we note that A_{tot} is a good measure of the space taken up by the windings. Since, for a given design, in particular for a given ratio n_2/n_1, the amplitude of the shim field is proportional to $(n_1 + n_2)I$, it can be seen that the power dissipation depends on A_{tot}, a, ρ and the amplitude of the shim field. It should be noted that the power dissipated in generating a shim field of given amplitude is independent of the cross-sectional area A or gauge of the wire, provided A_{tot} is fixed. Any change in A requires a compensating change in $(n_1 + n_2)$ to keep A_{tot} fixed. That, in turn, requires a compensating change in the current I to generate the same shim field, the net result being that the power dissipation remains unchanged.

This result, which does not seem to be widely appreciated, allows a meaningful comparison of the power dissipation of z^4 shim coils of *different* design to be made by requiring that A_{tot}, in addition to a, ρ, and the amplitude of the shim field, be the same in each case. Imposing this condition on A_{tot} amounts to keeping the space occupied by the windings the same, and different designs should be compared on that basis, since space for the windings is in many cases the limiting factor. It should be noted that the power dissipation of z^4 shim coils of different design, but characterized by the same values of A_{tot}, a, ρ, and shim field amplitude, will nevertheless vary because of the influence of the $[(n_1 + n_2)I]^2$ term in Eq. (4.13). (This term is constant for a given shim field amplitude only if n_1/n_2 remains fixed.)

68

To obtain the relationship between the power dissipation and I_2/I_1, the amplitude of the z^4 field, $(d^4 B_z/dz^4)_{z=0}$, needs to be determined. From Eq. (4.4), $(d^4 B_z/dz^4)_{z=0}$ is found to be given by

$$\left(\frac{d^4 B_z}{dz^4}\right)_{z=0} = \frac{45\mu_0 I_1}{a^5} \left\{ \frac{1 - 12(z_1/a)^2 + 8(z_1/a)^4}{[1 + (z_1/a)^2]^{11/2}} + \left(\frac{I_2}{I_1}\right) \frac{1 - 12(z_2/a)^2 + 8(z_2/a)^4}{[1 + (z_2/a)^2]^{11/2}} \right\}. \tag{4.14}$$

If $(d^4 B_z/dz^4)_{z=0}$ and a are the same in the different designs, we have

$$I_1 \propto \left\{ \frac{1 - 12(z_1/a)^2 + 8(z_1/a)^4}{[1 + (z_1/a)^2]^{11/2}} + \left(\frac{I_2}{I_1}\right) \frac{1 - 12(z_2/a)^2 + 8(z_2/a)^4}{[1 + (z_2/a)^2]^{11/2}} \right\}^{-1}. \tag{4.15}$$

Substituting Eqs. (4.8) and (4.9) into the above expression, and noting $I_2/I_1 = -n_2/n_1 = -|I_2/I_1|$, we obtain

$$I_1 \propto \frac{\left(1 + |I_2/I_1|^{2/3}\right)^{11/2}}{3|I_2/I_1| + 20|I_2/I_1|^{5/3} - 20|I_2/I_1|^3 - 3|I_2/I_1|^{11/3}}. \tag{4.16}$$

Combining Expression (4.16) and Eq. (4.13) yields a relationship between the power dissipation and $|I_2/I_1|$ given by

$$P \propto \frac{(1 + |I_2/I_1|)^2 \left(1 + |I_2/I_1|^{2/3}\right)^{11}}{(3|I_2/I_1| + 20|I_2/I_1|^{5/3} - 20|I_2/I_1|^3 - 3|I_2/I_1|^{11/3})^2}. \tag{4.17}$$

The dependence of the power dissipation on $|I_2/I_1|$ for Type 1, z^4 shim coils is illustrated by the broken curve in Fig. 4.2 where it has been assumed that $z_2 > z_1$ so that $|I_2/I_1| > 1$. The curve possesses an asymptote at $I_2/I_1 = -1$, since, in that limit, the two pairs of coils coincide and exactly cancel each other. It can be seen that the most efficient configuration is one where $I_2/I_1 \simeq -4$, i.e. where $n_2/n_1 \simeq 4$, the corresponding values of z_1/a and z_2/a, from Eqs. (4.8) and (4.9), being 0.864 and 1.84. Such a configuration would have a power dissipation 40% less than that proposed by Romeo and Hoult [3] for which $I_2/I_1 = -9$.

A second important criterion in assessing the performance of a shim coil is the spatial region over which the field closely approximates the desired functional
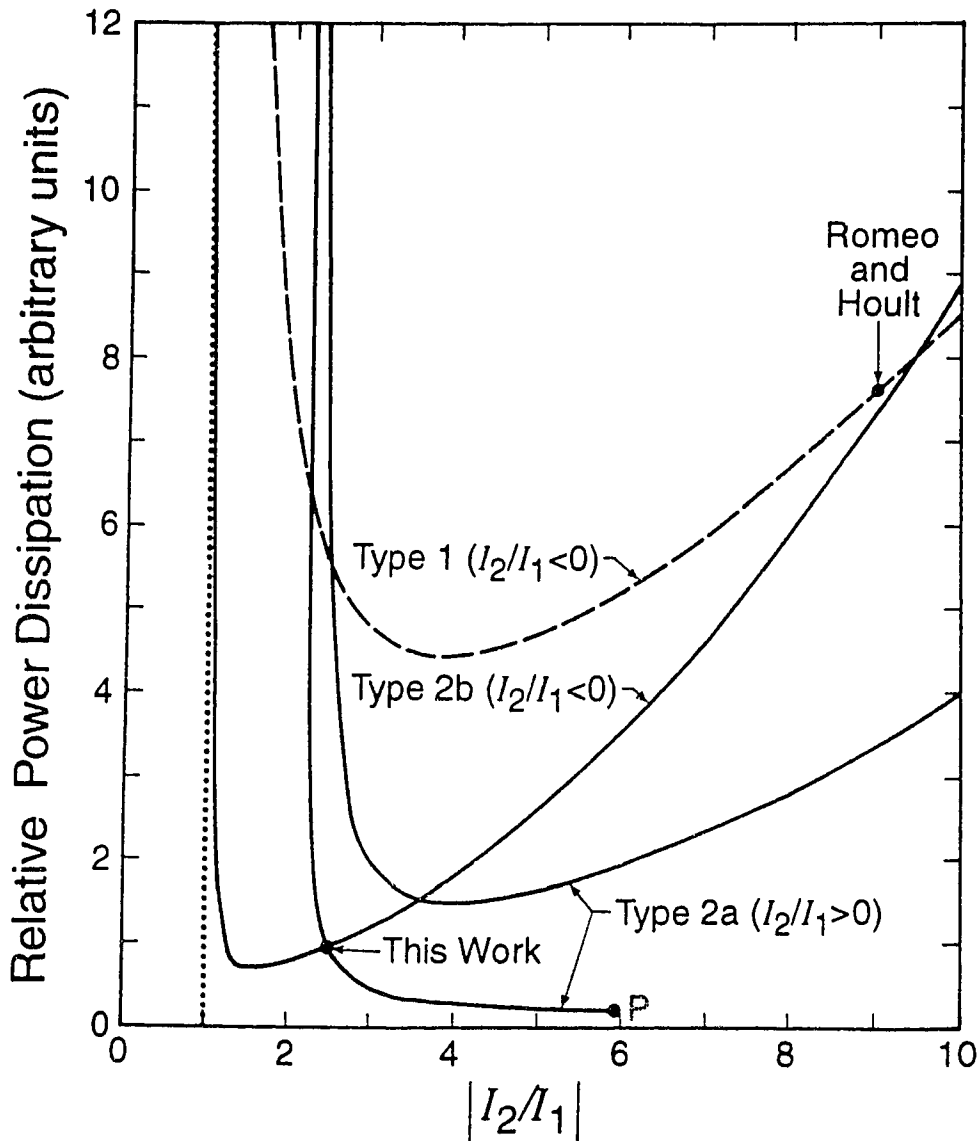
Figure 4.2: The broken curve shows the power, expressed in arbitrary units, dissipated by Type 1, z^4 shim coils, plotted as a function of $|I_2/I_1|$. The solid curves are corresponding graphs for Type 2a and 2b z^4 shim coils. The dotted line shows the asymptote $(I_2/I_1 = -1)$ of the curves corresponding to Type 1 and Type 2b shim coils. The end point P of the lower branch of the Type 2a graph represents a three-ring design where $z_1/a = 0$. The replacement shim coil was constructed following the Type 2b design indicated on the graph. Romeo and Hoult's Type 1 design is also shown.

form. The linear dimensions of this region obviously scale with the radius of the coil. Figure 4.3a shows the actual shim field and the ideal z^4 behaviour, fitted at the origin, for three different design parameters, namely $I_2/I_1 = -2, -4$, and -8. The range of $|z|/a$ over which the shim field deviates from the ideal z^4 behaviour, first, by less than 5% and, second, by less than 10% of the ideal are listed in Table 4.1 for these three designs. While the shim field generated by a $I_2/I_1 = -8$ design (and the Romeo and Hoult $I_2/I_1 = -9$ design [3]) follows closely the z^4 behaviour for $|z|/a < 0.5$, the shim field generated by the $I_2/I_1 = -4$ design is a better approximation over the range $|z|/a < 1$. Since this configuration is also the most efficient in terms of power dissipation, it would seem to be the best Type 1, z^4 shim coil, especially if a z^4 field is required over a large region. Even though, as will be seen later, the Romeo and Hoult design is close to satisfying the condition $(d^6 B_z/dz^6)_{z=0} = 0$, in addition to those in Eqs. (4.2) and (4.3), it generates a significant z^8 component. The $I_2/I_1 = -4$ design, on the other hand, generates a smaller z^8 component which is largely cancelled by a z^6 component of opposite sign.

4.2.2 Design of Type 2, z^4 Shim Coils for Which the z^2, z^6, and All Odd Power Terms Are Zero

In practice, it is not usually essential for the constant (z^0) field to be zero. We therefore relax this condition and, instead, examine Type 2, z^4 shim coil designs which satisfy the conditions

$$\left(\frac{d^2 B_z}{dz^2}\right)_{z=0} = 0 \tag{4.18}$$

$$\left(\frac{d^6 B_z}{dz^6}\right)_{z=0} = 0. \tag{4.19}$$

As before, we consider two pairs of rings, one pair at $z = \pm z_1$ carrying a current I_1, the other pair at $z = \pm z_2$ carrying a current I_2. The field on the z axis is therefore

71
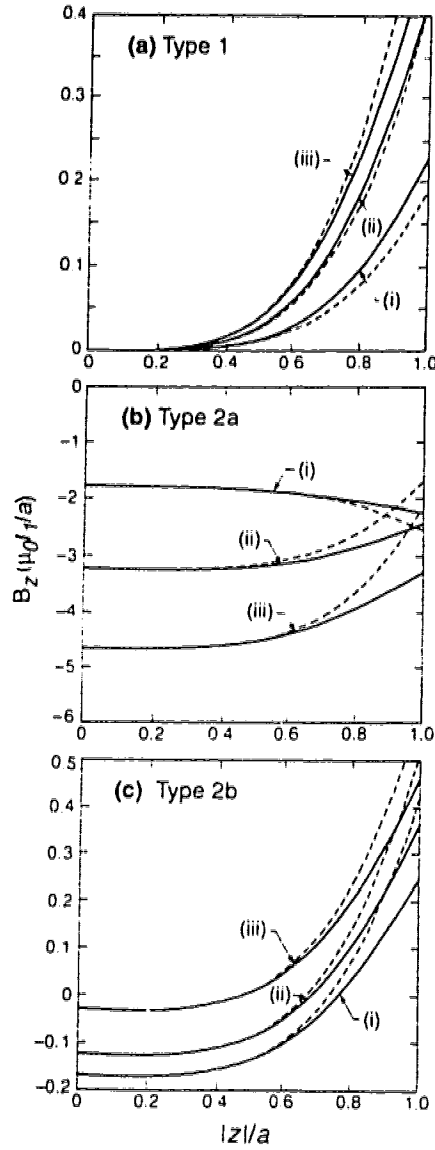
Figure 4.3: (a) The solid curves show the axial field B_z, expressed in units of $(\mu_0 I_1/a)$, generated by Type 1, z^4 shim coils, plotted as a function of $|z|/a$ for the case where I_2/I_1 is equal to (i) -2, (ii) -4, and (iii) -8. The broken curves show the corresponding ideal z^4 behaviour. (b) Corresponding curves for Type 2a, z^4 shim coils where I_2/I_1 is equal to (i) 4 on the upper branch in Fig. 4.2, (ii) 4 on the lower branch in Fig. 4.2, (iii) 5.93 on the lower branch in Fig. 4.2, corresponding to a three-ring design. (c) Corresponding curves for Type 2b, z^4 shim coils where I_2/I_1 is equal to (i) -2, (ii) -4, and (iii) -8.

72

Table 4.1: Values of $|z|/a$, < 1.0, where deviations of the shim field from the ideal z^4 functional form are, first, less than 5% and, second, less than 10% of the ideal field for some representative Type 1, 2a, and 2b configurations

Coil type	I_2/I_1	Values of $|z|/a$ where deviations from the ideal z^4 functional form are:		Shim field displayed as curve in figure
		$< 5\%$	$< 10\%$	
Type 1	-2	< 0.296	< 0.430	4.3a (i)
Type 1	-4	$< 0.408, > 0.911$	everywhere	4.3a (ii)
Type 1	-8	< 0.688	< 0.818	4.3a (iii)
Type 2a[a]	4	< 0.470	< 0.581	4.3b (i)
Type 2a[b]	4	< 0.500	< 0.610	4.3b (ii)
Type 2a[c]	5.93	< 0.457	< 0.562	4.3b (iii)
Type 2b	-2	< 0.579	< 0.704	4.3c (i)
Type 2b	-4	< 0.599	< 0.735	4.3c (ii)
Type 2b	-8	< 0.602	< 0.740	4.3c (iii)

[a]Upper branch in Fig. 4.2.
[b]Lower branch in Fig. 4.2.
[c]Three-ring configuration.

73

given by Eq. (4.4). Substituting Eq. (4.4) into Eqs (4.18) and (4.19) yields

$$-\frac{I_2}{I_1} = \frac{\left[4\left(z_1/a\right)^2 - 1\right]\left[1 + \left(z_2/a\right)^2\right]^{7/2}}{\left[4\left(z_2/a\right)^2 - 1\right]\left[1 + \left(z_1/a\right)^2\right]^{7/2}} \tag{4.20}$$

$$-\frac{I_2}{I_1} = \frac{\left[64\left(z_1/a\right)^6 - 240\left(z_1/a\right)^4 + 120\left(z_1/a\right)^2 - 5\right]\left[1 + \left(z_2/a\right)^2\right]^{15/2}}{\left[64\left(z_2/a\right)^6 - 240\left(z_2/a\right)^4 + 120\left(z_2/a\right)^2 - 5\right]\left[1 + \left(z_1/a\right)^2\right]^{15/2}}. \tag{4.21}$$

Combining the two equations to eliminate I_2/I_1 leads to an equation of fifth order in $(z_1/a)^2$ and $(z_2/a)^2$, whose solutions significant to our problem form three distinct branches, which are referred to as Type 2a, 2b, and 2c, and are shown in Fig. 4.1, together with representative values of I_2/I_1. The minimum value of I_2/I_1 for the Type 2a branch is 2.23. Solutions corresponding to Type 2a and 2b have been presented in somewhat different form by Bobrov and Punchard [6]. However, these workers did not discuss the relative merits of different designs corresponding to the various solutions.

In Fig. 4.1, the curves representing Type 1 and Type 2b designs intersect at the point $z_1/a = 0.728$, $z_2/a = 2.41$, the corresponding value of I_2/I_1 being -9.45. A design with these parameters therefore satisfies all three conditions $(B_z)_{z=0} = 0$, $(d^2 B_z/dz^2)_{z=0} = 0$, and $(d^6 B_z/dz^6)_{z=0} = 0$. However, as was shown earlier, such a design, and that of Romeo and Hoult [3] which approximates it, is not the optimum for minimizing power dissipation.

The solid curves in Fig. 4.2 show the power dissipated by Type 2a and 2b shim coils in generating a z^4 field of the same amplitude as that chosen for the Type 1 designs. Thus, the solid and broken curves can be directly compared. The power dissipated by Type 2c shim coils is two orders of magnitude too large to be shown on the graph and this design therefore receives no further consideration. The graph representing Type 2a shim coils consists of two branches which merge at $I_2/I_1 = 2.27$ where the z^4 compone   .⸴ges sign and the power dissipated becomes infinite. The lower branch terminates at the point P where $I_2/I_1 = 5.93$,

74

the corresponding values of z_1/a and z_2/a being zero and 0.617, respectively. This point therefore represents a three-ring system. All other designs in Figs. 4.1 and 4.2 involve four rings.

It can be seen that Type 2a designs dissipate the least amount of power over much of the range considered, when generating a given z^4 component. This can be attributed to the fact that, for such designs, I_1 and I_2 are of the same sign so that the axial fields generated by the individual rings add rather than subtract, as they do for Type 1 and Type 2b.

The fields generated by three representative Type 2a shim coils are shown in Fig. 4.3b, together with the ideal z^4 behaviour. It can be seen that they generate large z^0 shifts which may be unacceptable in some applications. The fields generated by three representative Type 2b shim coils are displayed in Fig. 4.3c. The range of $|z|/a$ over which the actual shim field deviates from the ideal z^4 behaviour, first, by less than 5% and, second, by less than 10% are listed in Table 4.1 for these six Type 2 designs.

4.3   Construction and Evaluation of a z^4 Shim Coil

The replacement z^4 shim coil was constructed following a Type 2b design with the parameter $I_2/I_1 = -2.5$ (see Fig. 4.2, where the design coincidentally lies at the intersection of the lower Type 2a curve and the Type 2b curve), the corresponding values of z_1/a and z_2/a being 0.740 and 1.63, respectively. This design was selected because it was expected to generate the most accurate z^4 shim field, while causing a temperature rise of no more than 2°C in one hour in the sample space of our magnet. Moreover, the predicted z^0 shift was small enough to be easily accommodated.

Each inner and outer coil consisted of 18 and 45 turns, respectively, of 14 AWG copper wire, closely wound in four layers giving an average coil radius

a of 13.9 cm, a value of A_{tot} of 2.6 cm^2, and a resistance of 0.97 Ω at room tempera-
ture. Values of $\delta a/a$, $\delta z_1/z_1$, and $\delta z_2/z_2$, where δa, δz_1, and δz_2 are half the spread
in the values of a, z_1, and z_2 associated with the finite size of the wire, are a measure
of the departure of a real z^4 shim coil from an ideal delta function configuration.
For our coil, $\delta a/a$, $\delta z_1/z_1$, and $\delta z_2/z_2$, are 0.022, 0.042, and 0.045, respectively.

The magnetic field generated by the replacement shim coil was measured by
feeding a 1 A, 500 Hz sinusoidal current through the coil and measuring the voltage
induced in a small cylindrical search coil, which was placed at various points on the
axis of the shim coil. The search coil, approximately 10 mm in length and diameter,
was wound with 100 turns of 32 AWG copper wire. The area-turns of the search
coil is 9.08×10^{-3} m^2. Values of the magnetic field were obtained by converting
measured voltage data using the following relation

$$B_z = \frac{V}{2\pi f A_s N_s},$$ (4.22)

where V is the voltage induced in the search coil, f is the frequency of the sinusoidal
current, and the product $A_s N_s$ is the area-turns of the search coil.

The data points in Fig. 4.4 show the axial field per unit current generated by
the shim coil, plotted as a function of z. A least squares fit of the data in Fig. 4.4
to a polynomial of the form $A + B(z/a)^2 + C(z/a)^4$ gives

$$\frac{B_z}{I} = -(26.64 \pm 0.04) + (4.6 \pm 0.7)\left(\frac{z}{13.9}\right)^2 + (94 \pm 2)\left(\frac{z}{13.9}\right)^4,$$ (4.23)

where B_z/I is in (mT/A) and z is in cm. The fit is shown as the curve in Fig. 4.4.
This is predominantly a z^4 variation but there is a small z^2 component. While it
would be possible to eliminate the z^2 component by a small readjustment of the
locations of the inner or outer pairs of coils, this was judged not to be necessary since
it could be compensated using the existing z^2 shim coil with an additional power
dissipation of only 0.6 watts. There was no evidence of any other components up
to and including z^8. The z^4 component for an ideal Type 2b, $I_2/I_1 = -2.5$ design
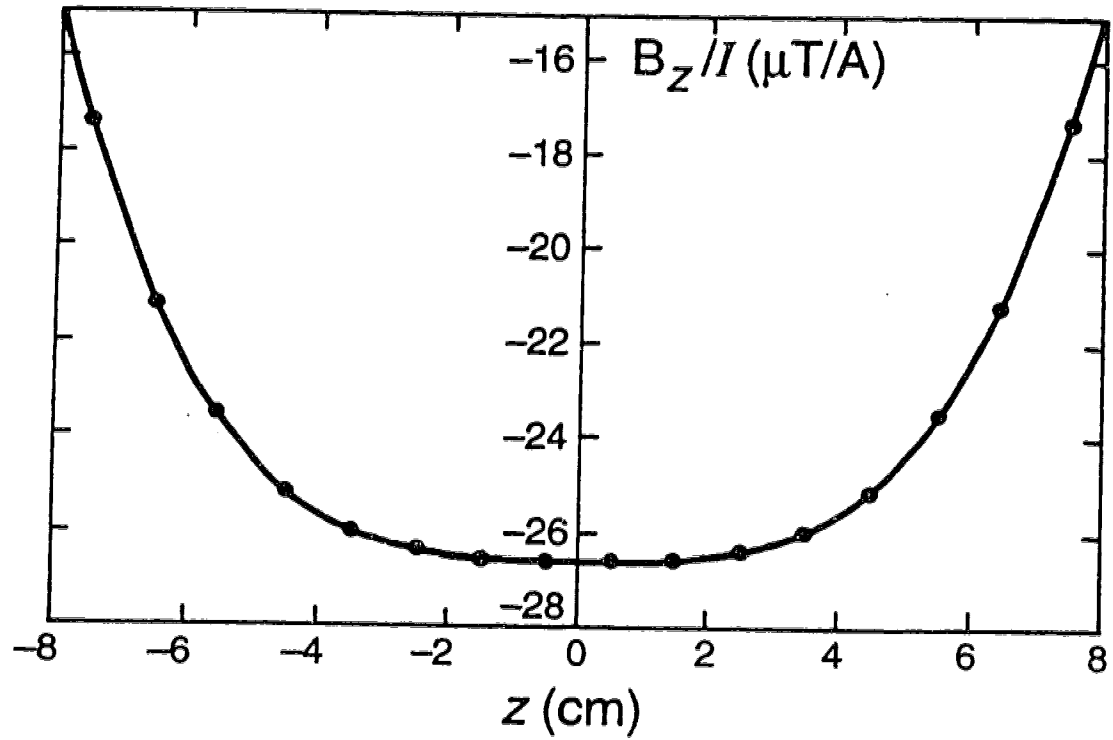
Figure 4.4: The data points show the measured axial field per unit current, B_z/I, in μT/A, generated by the replacement z^4 shim coil, plotted as a function of z. The curve represents a least squares fit of the data (see Eq. (4.23)).

of radius 13.9 cm, is $103(z/13.9)^4$ (mT/A). The presence of the z^2 component and the discrepancy of 8.4% between the experimental and theoretical z^4 components is attributed to deviations from the ideal delta function configuration.

Since the radius of the replacement shim coil is 13.9 cm, whereas that of the original Bruker z^4 shim coil is approximately 18.75 cm, the effect of simply scaling down the Bruker coil to a radius of 13.9 cm would be to reduce the power dissipation by a factor $(18.75/13.9)^9 = 14.8$, according to the relation of the power dissipation to the coil dimensions derived in the previous section. The power dissipated in the replacement shim coil when the z^4 field variation of the Bruker magnet is fully compensated is 21 watts. This is a factor of 43 smaller than the power that would need to be dissipated in the Bruker shim coil if full compensation was to be achieved. The remaining factor, $43/14.8 \simeq 3$, must be attributed either to a difference in the integrated conductor cross-sectional area (suitably scaled) or to a difference in the design of the two coils.

4.4 Discussion

The magnetic field in several animal-size magnets manufactured in the 1980s is believed to exhibit a substantial z^4 variation. Fully compensating such a variation should greatly improve the magnet homogeneity over an extended region. However, it may not be possible to achieve full compensation using the manufacturer's z^4 shim coil, without excessive power dissipation and heating of the sample space. While a substantial reduction in the power dissipation can be achieved by reducing the size of the z^4 shim coil, this approach is limited by the need to maintain adequate sample space. Other approaches may therefore be required.

In this chapter, the influence of the design parameters of simple four-coil z^4 shim coils on the power dissipation, accuracy of the z^4 shim field, and magnitude of the z^0 shift, have been determined. This should enable the most appropriate design

78

to be chosen in individual cases. The method used to compare the power dissipation of different coil designs is not restricted to four-coil z^4 shim coils. However, its most likely application is in the design of high order z^n shim coils in wide bore NMR magnets.

References

[1] S.R. Thomas, J.L. Ackerman, and J.G. Kereiakes, *Magn. Reson. Imaging* **2**, 341 (1984).

[2] S. Yamamoto, T. Yamada, M. Morita, T. Matsuda, and M. Iwamoto, IEEE Trans. Magn. **MAG-21**, 698 (1985).

[3] F. Romeo and D.I. Hoult, *Magn. Reson. Med.* **1**, 44 (1984).

[4] R. Turner, *J. Phys. D: Appl. Phys.* **19**, L147 (1986).

[5] M.J.E. Golay, *Rev. Sci. Instrum.* **29**, 313 (1958).

[6] E.S. Bobrov and W.F.B. Punchard, *IEEE Trans. Magn.* **24**, 533 (1988).

Chapter Five

DESIGN OF ELLIPTIC CYLINDER GRADIENT COILS OF MINIMUM INDUCTANCE[1]

5.1 Introduction

Magnetic resonance imaging (MRI) and magnetic resonance spectroscopy (MRS) normally require the generation of three linear, mutually orthogonal, magnetic field gradients. For some applications, such as fast imaging [1, 2], strong gradients ~ 100 mT/m, capable of being switched on or off in a time ~ 100 μs, are required. A major advance in gradient coil technology that enabled such specifications to be achieved, was the development of the target field approach by Turner [3]. This development allows one to determine the current distribution on a cylindrical surface which will not only generate a magnetic field with specific values at a few target field points, but will also minimize the power dissipation or the stored energy, which in turn minimizes the switching speed [4, 5].

The power dissipation and stored energy associated with a given gradient strength are strongly dependent upon the volume contained within the gradient coil. For example, for circular cylinder coils, the power dissipation and stored energy vary as the fourth and fifth powers of the radius, respectively [5, 6]. Because the aspect ratio of a typical human body at its largest cross-section is significantly different from unity, coils which are more elliptical than circular in cross-section can be advantageous in *in vivo* NMR since they allow a better "filling factor" to be

achieved, thereby reducing the power dissipation as well as the rise and fall times of gradient pulses.

The design of elliptic cylinder gradient coils using the target field approach [3] requires knowledge of the magnetic field generated by a current flowing on the surface of an elliptical cylinder. Petropoulos *et al.* [7] have derived an expression for the longitudinal (z) magnetic field inside an elliptic cylinder when a distributed current on its surface is restricted to azimuthal flow, and they have used this expression to design z gradient coils of minimum inductance. In this chapter, we shall derive general expressions for the magnetic field and stored energy of an elliptic cylinder coil where the current flows in both the axial and azimuthal directions. These expressions can be used to design elliptic cylinder coils which generate not only uniform gradients but also other field profiles such as a uniform field or higher order shim fields [8]. When specialized to purely azimuthal flow, our expression for the magnetic field differs in an important respect from that of Petropoulos *et al.* This stems from an error in their derivation.

A problem that has not been studied in any detail is the nonuniformity of the longitudinal magnetic field of a z gradient coil in the transverse (x and y) directions, that is associated with the elliptical geometry. We address this issue by expanding, in ascending powers of x and y, the magnetic field associated with a purely azimuthal current. It is then shown that the nonuniformity in the transverse directions can be largely eliminated by allowing the current to flow axially as well as azimuthally. The considerable improvement in the uniformity of the field in the transverse directions comes at the expense of a small increase in the stored energy, which nevertheless remains well below that of the corresponding circular cylinder coil. It is shown that the expressions obtained by expanding the magnetic field in powers of x and y are easily modified to cover the case where the current flows axially as well as azimuthally.

It is found that, even when the current is restricted to azimuthal flow, the nonuniformity of the magnetic field in the transverse directions in a z gradient coil of minimum inductance is considerably smaller than that reported by Petropoulos et al. [7]. We believe that this is mainly caused by the error in their expression for the magnetic field.

5.2 Theory

We shall consider a current confined to the surface of an elliptic cylinder, and use elliptic cylinder coordinates so that the current density on the elliptical surface possesses at most two components. The target field approach [3] will be used to find the optimal current distribution which will minimize the stored energy, and hence the inductance of an elliptic coil. To do so, it is necessary to obtain the expansion of Green's function [3]. This, in turn, involves solving Laplace's equation, the solutions of which, in elliptic cylinder coordinates, are expressed in terms of Mathieu functions [9].

We begin by describing elliptic cylinder coordinates and Mathieu functions. We then derive the expansion of Green's function which enables general expressions for the magnetic field and stored energy of an elliptic cylinder coil to be determined. These expressions are used to obtain the current density distribution on an elliptic cylinder z gradient coil of minimum inductance, firstly when the current is restricted to the azimuthal direction, and secondly when this restriction is lifted.

5.2.1 Description of Elliptic Cylinder Coordinates

Largely adopting the notation of McLachlan [9], the elliptic cylinder coordinates, ξ, η and z, are related to cartesian coordinates by

$$x = c \cosh \xi \cos \eta$$

$$y = c \sinh \xi \sin \eta \tag{5.1}$$

$$z = z$$

with domains of ξ, η and z being

$$0 \le \xi < \infty, \qquad -\pi \le \eta \le \pi, \qquad -\infty < z < \infty. \tag{5.2}$$

From the relations involving x and y, the following two equations can be derived,

$$\frac{x^2}{c^2 \cosh^2 \xi} + \frac{y^2}{c^2 \sinh^2 \xi} = 1 \tag{5.3}$$

$$\frac{x^2}{c^2 \cos^2 \eta} - \frac{y^2}{c^2 \sin^2 \eta} = 1. \tag{5.4}$$

Equation (5.3) represents a family of confocal ellipses with semi-major axes $a = c \cosh \xi$, semi-minor axes $b = c \sinh \xi$, and common foci at $x = \pm c$, $y = 0$, as illustrated in Fig. 5.1. The eccentricity of each ellipse, e, is $1/\cosh \xi$. Equation (5.4), on the other hand, represents a family of confocal hyperbolae with the same foci as the ellipses. The two families of curves intersect orthogonally. It can be seen in Fig. 5.1 that η is a measure of angular position in the azimuthal direction, and is related to the azimuthal angle $\phi = \tan^{-1}(y/x)$ in cylindrical coordinates by

$$\tan \phi = \tanh \xi \tan \eta. \tag{5.5}$$

When $e \to 1$, $\xi \to 0$, and the ellipse reduces to a straight line joining the two foci (see Fig. 5.1). On the other hand, if $e \to 0$ with a constant, $\xi \to \infty$, and the ellipse tends to a circle of radius a. In this case, $c \cosh \xi$ and $c \sinh \xi$ tend to a, and η tends to ϕ.

The three components of any vector $\mathcal{V}$ in elliptic cylinder coordinates, $\mathcal{V}_\xi$, $\mathcal{V}_\eta$ and $\mathcal{V}_z$, are related to the three components of the vector in cartesian coordinates, $\mathcal{V}_x$, $\mathcal{V}_y$ and $\mathcal{V}_z$, by

$$\mathcal{V}_\xi = \mathcal{V}_x \frac{\sinh \xi \cos \eta}{\sqrt{\sinh^2 \xi + \sin^2 \eta}} + \mathcal{V}_y \frac{\cosh \xi \sin \eta}{\sqrt{\sinh^2 \xi + \sin^2 \eta}} \tag{5.6}$$
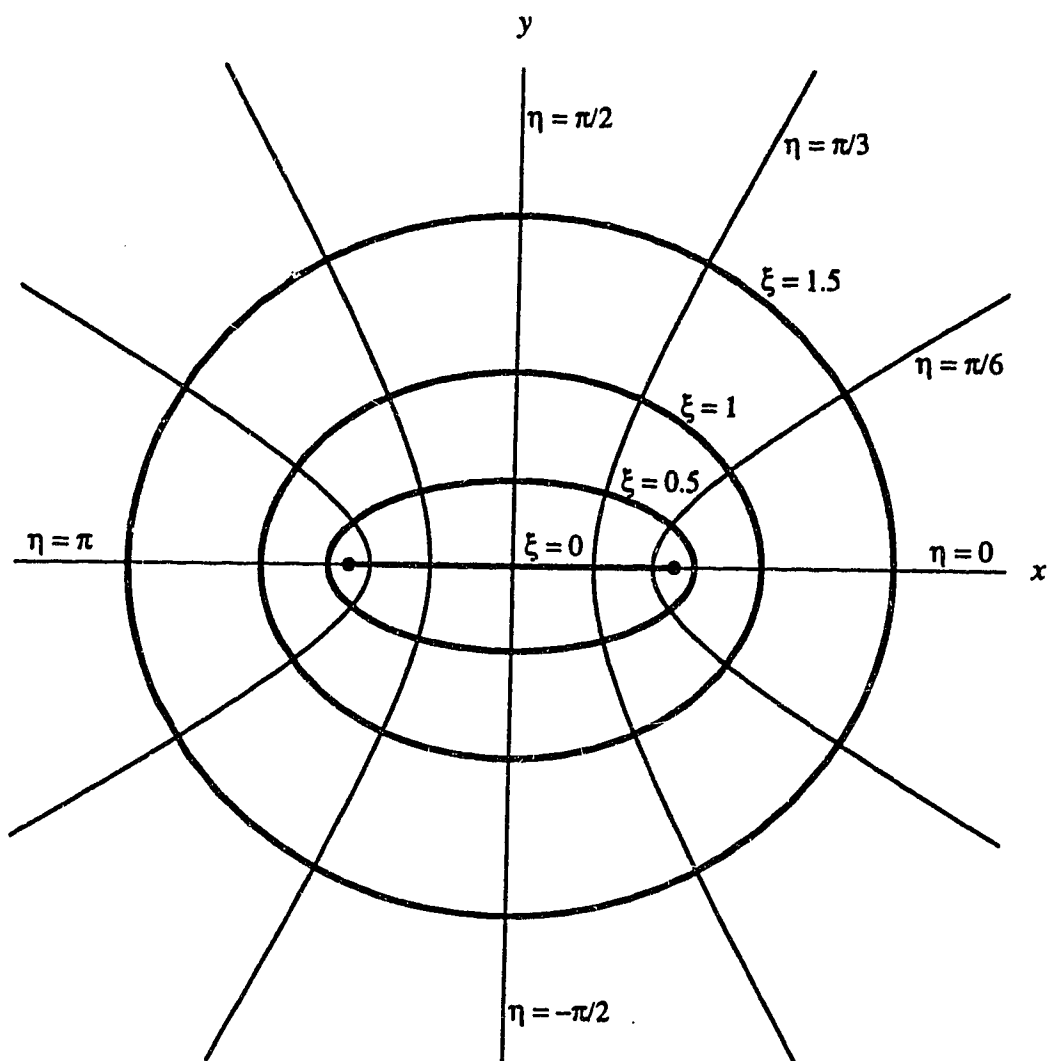
Figure 5.1: Illustration of elliptical coordinates. The bold curves are confocal ellipses corresponding to ξ = 0.5, 1.0, and 1.5. The light curves are confocal hyperbolae, corresponding to η = $\pi/6$, $\pi/3$, $\pi/2$, etc., each possessing the same foci as the ellipses.

$$\mathcal{V}_\eta' = -\mathcal{V}_x \frac{\cosh \xi \sin \eta}{\sqrt{\sinh^2 \xi + \sin^2 \eta}} + \mathcal{V}_y \frac{\sinh \xi \cos \eta}{\sqrt{\sinh^2 \xi + \sin^2 \eta}} \qquad (5.7)$$

$$\mathcal{V}_x = \mathcal{V}_\xi \frac{\sinh \xi \cos \eta}{\sqrt{\sinh^2 \xi + \sin^2 \eta}} - \mathcal{V}_\eta \frac{\cosh \xi \sin \eta}{\sqrt{\sinh^2 \xi + \sin^2 \eta}} \qquad (5.8)$$

$$\mathcal{V}_y = \mathcal{V}_\xi \frac{\cosh \xi \sin \eta}{\sqrt{\sinh^2 \xi + \sin^2 \eta}} + \mathcal{V}_\eta \frac{\sinh \xi \cos \eta}{\sqrt{\sinh^2 \xi + \sin^2 \eta}} \qquad (5.9)$$

$$\mathcal{V}_z = \mathcal{V}_z. \qquad (5.10)$$

5.2.2 Mathieu Functions

Let us consider a function $\psi(\boldsymbol{r})$ which satisfies Laplace's equation, so that

$$\nabla^2 \psi(\boldsymbol{r}) = 0. \qquad (5.11)$$

In elliptic cylinder coordinates, Eq. (5.11) can be written as [9]

$$\frac{\partial^2 \psi}{\partial \xi^2} + \frac{\partial^2 \psi}{\partial \eta^2} + \frac{c^2}{2}(\cosh 2\xi - \cos 2\eta)\frac{\partial^2 \psi}{\partial z^2} = 0. \qquad (5.12)$$

Separation of variables in Eq. (5.12) by substituting $\psi = U(\xi)V(\eta)W(z)$ leads to the following three equations,

$$\frac{d^2 U}{d\xi^2} - (h + 2q\cosh 2\xi)U = 0 \qquad (5.13)$$

$$\frac{d^2 V}{d\eta^2} + (h + 2q\cos 2\eta)V = 0 \qquad (5.14)$$

$$\frac{d^2 W}{dz^2} + k^2 W = 0, \qquad (5.15)$$

where h and k are separation constants, and $q = c^2 k^2/4$.

Equation (5.15) is the same as the differential equation with respect to z in cylindrical coordinates. Thus, its solutions are of the form $\exp(\pm ikz)$. Equation (5.14) and its solutions are called Mathieu's equation and Mathieu functions for $-q$, respectively. Similarly, Eq. (5.13) and its solutions are called Mathieu's modified equation and modified Mathieu functions for $-q$, respectively. The usual

form of Mathieu's equation and Mathieu's modified equation, encountered in the literature [9, 10], contain $(h - 2q \cos 2\eta)$ and $(h - 2q \cosh 2\xi)$, respectively. However, the solutions of Eqs. (5.13) and (5.14) can be obtained from the solutions of those equations by replacing q by $-q$. We discuss the solutions of Eqs. (5.14) and (5.13), in turn.

The solutions of Mathieu's equation, Eq. (5.14), take different forms according to the values of h and q. For our application, the solutions of Eq. (5.14) must be periodic functions of η so that $V(2p\pi + \eta) = V(\eta)$, where p is an integer. Such solutions are called periodic Mathieu functions of integral order for $-q$ (or Mathieu functions for brevity). They consist of four functions, corresponding to four characteristic values of h, usually expressed as [9]

$$\mathrm{ce}_{2n}(\eta, -q) = (-1)^n \sum_{r=0}^{\infty} (-1)^r A_{2r}^{(2n)} \cos 2r\eta, \qquad (h = a_{2n}) \quad (5.16)$$

$$\mathrm{ce}_{2n+1}(\eta, -q) = (-1)^n \sum_{r=0}^{\infty} (-1)^r B_{2r+1}^{(2n+1)} \cos (2r+1)\eta, \quad (h = b_{2n+1}) \quad (5.17)$$

$$\mathrm{se}_{2n+1}(\eta, -q) = (-1)^n \sum_{r=0}^{\infty} (-1)^r A_{2r+1}^{(2n+1)} \sin (2r+1)\eta, \quad (h = a_{2n+1}) \quad (5.18)$$

$$\mathrm{se}_{2n+2}(\eta, -q) = (-1)^n \sum_{r=0}^{\infty} (-1)^r B_{2r+2}^{(2n+2)} \sin (2r+2)\eta, \quad (h = b_{2n+2}) \quad (5.19)$$

where a_m and b_m ($m = 2n$, $2n + 1$ or $2n + 2$) are the characteristic values, and $n = 0, 1, 2, \ldots$. With this choice of subscripts, each of the above functions has n real zeros in the range $0 < \eta < \pi/2$.

The Mathieu functions for $-q$ are related to their counterparts for $+q$ by [9]

$$\mathrm{ce}_{2n}(\eta, -q) = (-1)^n \mathrm{ce}_{2n}\left(\frac{\pi}{2} - \eta, q\right) \qquad (5.20)$$

$$\mathrm{ce}_{2n+1}(\eta, -q) = (-1)^n \mathrm{se}_{2n+1}\left(\frac{\pi}{2} - \eta, q\right) \qquad (5.21)$$

$$\mathrm{se}_{2n+1}(\eta, -q) = (-1)^n \mathrm{ce}_{2n+1}\left(\frac{\pi}{2} - \eta, q\right) \qquad (5.22)$$

$$\mathrm{se}_{2n+2}(\eta, -q) = (-1)^n \mathrm{se}_{2n+2}\left(\frac{\pi}{2} - \eta, q\right). \qquad (5.23)$$

Their orthonormal properties are the same as those of the Mathieu functions for $+q$ [9], and are given by

$$\frac{1}{\pi} \int_{-\pi}^{\pi} d\eta \; \mathrm{ce}_m(\eta, -q) \, \mathrm{ce}_n(\eta, -q) \;=\; \delta_{m,n} \qquad (5.24)$$

$$\frac{1}{\pi} \int_{-\pi}^{\pi} d\eta \; \mathrm{se}_m(\eta, -q) \, \mathrm{se}_n(\eta, -q) \;=\; \delta_{m,n} \qquad (5.25)$$

$$\frac{1}{\pi} \int_{-\pi}^{\pi} d\eta \; \mathrm{ce}_m(\eta, -q) \, \mathrm{se}_n(\eta, -q) \;=\; 0. \qquad (5.26)$$

Thus, the Mathieu functions (5.16) – (5.19) form a complete, orthonormal basis set.

In Eqs. (5.16) – (5.19), the coefficients $A_p^{(m)}$ and $B_p^{(m)}$, as well as the characteristic values a_m and b_m, are functions of q, and can be determined using the normalization of the Mathieu functions, given by Eqs. (5.24) and (5.25), and recurrence relations among the coefficients. These recurrence relations are obtainable by substituting each series (5.16) – (5.19) in Eq. (5.14). For example, substituting the series (5.16) in Eq. (5.14) yields

$$\sum_{r=0}^{\infty} (-1)^r (h - 4r^2) A_{2r}^{(2n)} \cos 2r\eta + q \sum_{r=0}^{\infty} (-1)^r A_{2r}^{(2n)} \left[\cos(2r-2)\eta + \cos(2r+2)\eta \right] = 0.$$
$$(5.27)$$

By equating coefficients for $\cos 2r\eta$ of the same order in Eq. (5.27), the recurrence relations among the coefficients of the series (5.16) are found to be

$$h A_0^{(2n)} - q A_2^{(2n)} = 0,$$

$$(h - 4) A_2^{(2n)} - q \left[2 A_0^{(2n)} + A_4^{(2n)} \right] = 0, \qquad (5.28)$$

$$(h - 4r^2) A_{2r}^{(2n)} - q \left[A_{2r-2}^{(2n)} + A_{2r+2}^{(2n)} \right] = 0, \quad r \geq 2$$

Some low-order Mathieu functions, corresponding to $q = 1$ and $q = 10$, are shown in Fig. 5.2 as a function of η.

Since the Mathieu functions form a complete basis set, any periodic function $f(\eta)$ with a period π or 2π can be expressed in terms of Mathieu functions as

$$f(\eta) = \sum_{m=0}^{\infty} C_m(q) \, \mathrm{ce}_m(\eta, -q) + \sum_{m=1}^{\infty} D_m(q) \, \mathrm{se}_m(\eta, -q) \qquad (5.29)$$
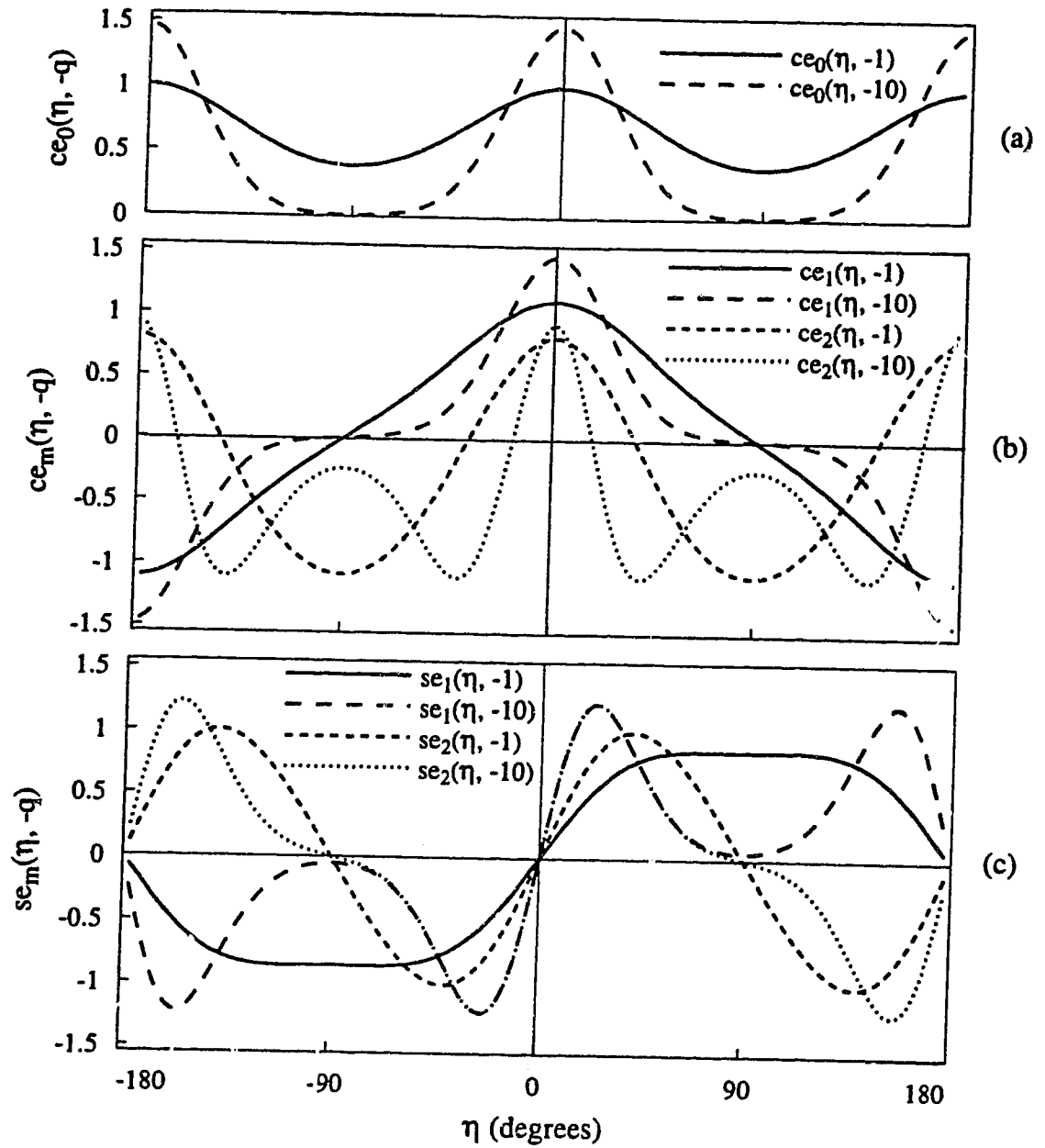
Figure 5.2: Graphs of the Mathieu functions (a) $ce_0(\eta, -1)$ and $ce_0(\eta, -10)$, (b) $ce_1(\eta, -1)$, $ce_1(\eta, -10)$, $ce_2(\eta, -1)$ and $ce_2(\eta, -10)$, and (c) $se_1(\eta, -1)$, $se_1(\eta, -10)$, $se_2(\eta, -1)$ and $se_2(\eta, -10)$, plotted as a function of η. Note the overlap of $se_1(\eta, -10)$ and $se_2(\eta, -10)$ in the region $-\pi/2 < \eta < \pi/2$.

88

with

$$C_m(q) = \frac{1}{\pi} \int_{-\pi}^{\pi} d\eta \, f(\eta) \, \mathrm{ce}_m(\eta, -q) \tag{5.30}$$

$$D_m(q) = \frac{1}{\pi} \int_{-\pi}^{\pi} d\eta \, f(\eta) \, \mathrm{se}_m(\eta, -q). \tag{5.31}$$

Turning now to Eq. (5.13), Mathieu's modified equation, its two independent solutions are called modified Mathieu functions of the first and second kind, respectively. The modified Mathieu functions can be expressed in different forms [9]. To achieve quick convergence in numerical computation, the modified Mathieu functions of the first kind can be expressed as

$$\mathrm{Ce}_{2n}(\xi, -q) = (-1)^n \sum_{r=0}^{\infty} (-1)^r A_{2r}^{(2n)} \cosh 2r\xi \tag{5.32}$$

$$\mathrm{Ce}_{2n+1}(\xi, -q) = (-1)^n \sum_{r=0}^{\infty} (-1)^r B_{2r+1}^{(2n+1)} \cosh (2r+1)\xi \tag{5.33}$$

$$\mathrm{Se}_{2n+1}(\xi, -q) = (-1)^n \sum_{r=0}^{\infty} (-1)^r A_{2r+1}^{(2n+1)} \sinh (2r+1)\xi \tag{5.34}$$

$$\mathrm{Se}_{2n+2}(\xi, -q) = (-1)^n \sum_{r=0}^{\infty} (-1)^r B_{2r+2}^{(2n+2)} \sinh (2r+2)\xi, \tag{5.35}$$

and the modified Mathieu functions of the second kind can be expressed as

$$\mathrm{Fek}_{2n}(\xi, -q) = \frac{M_{2n}^c}{\pi A_0^{(2n)}} \sum_{r=0}^{\infty} A_{2r}^{(2n)} I_r(\sqrt{q}\, e^{-\xi}) K_r(\sqrt{q}\, e^{\xi}) \tag{5.36}$$

$$\mathrm{Fek}_{2n+1}(\xi, -q) = \frac{M_{2n+1}^c}{\pi B_1^{(2n+1)}} \sum_{r=0}^{\infty} B_{2r+1}^{(2n+1)} \left[I_r(\sqrt{q}\, e^{-\xi}) K_{r+1}(\sqrt{q}\, e^{\xi}) \right.$$
$$\left. - I_{r+1}(\sqrt{q}\, e^{-\xi}) K_r(\sqrt{q}\, e^{\xi}) \right] \tag{5.37}$$

$$\mathrm{Gek}_{2n+1}(\xi, -q) = \frac{M_{2n+1}^s}{\pi A_1^{(2n+1)}} \sum_{r=0}^{\infty} A_{2r+1}^{(2n+1)} \left[I_r(\sqrt{q}\, e^{-\xi}) K_{r+1}(\sqrt{q}\, e^{\xi}) \right.$$
$$\left. + I_{r+1}(\sqrt{q}\, e^{-\xi}) K_r(\sqrt{q}\, e^{\xi}) \right] \tag{5.38}$$

$$\mathrm{Gek}_{2n+2}(\xi, -q) = \frac{M_{2n+2}^s}{\pi B_2^{(2n+2)}} \sum_{r=0}^{\infty} B_{2r+2}^{(2n+2)} \left[I_r(\sqrt{q}\, e^{-\xi}) K_{r+2}(\sqrt{q}\, e^{\xi}) \right.$$
$$\left. - I_{r+2}(\sqrt{q}\, e^{-\xi}) K_r(\sqrt{q}\, e^{\xi}) \right], \tag{5.39}$$

corresponding to the characteristic values a_{2n}, b_{2n+1}, a_{2n+1} and b_{2n+2}, respectively. In Eqs. (5.32) − (5.39), $A_p^{(m)}$ and $B_p^{(m)}$ are the same as those appearing in Eqs. (5.16) −

(5.19), $I_r(x)$ and $K_r(x)$ are, respectively, modified Bessel functions of the first and second kind, and M_m^c and M_m^s are given by

$$M_{2n}^c = \frac{(-1)^n}{A_0^{(2n)}} \, \mathrm{ce}_{2n}(0, -q) \, \mathrm{ce}_{2n}(\frac{\pi}{2}, -q) \tag{5.40}$$

$$M_{2n+1}^c = \frac{(-1)^{n+1}}{\sqrt{q} \, B_1^{(2n+1)}} \, \mathrm{ce}_{2n+1}(0, -q) \, \mathrm{ce}_{2n+1}'(\frac{\pi}{2}, -q) \tag{5.41}$$

$$M_{2n+1}^s = \frac{(-1)^n}{\sqrt{q} \, A_1^{(2n+1)}} \, \mathrm{se}_{2n+1}'(0, -q) \, \mathrm{se}_{2n+1}(\frac{\pi}{2}, -q) \tag{5.42}$$

$$M_{2n+2}^s = \frac{(-1)^{n+1}}{q B_2^{(2n+2)}} \, \mathrm{se}_{2n+2}'(0, -q) \, \mathrm{se}_{2n+2}'(\frac{\pi}{2}, -q), \tag{5.43}$$

where the primes in $\mathrm{ce}_m'(\eta, -q)$ and $\mathrm{se}_m'(\eta, -q)$ signify derivatives with respect to η. The graphs of some low-order modified Mathieu functions are shown in Fig. 5.3, plotted as a function of ξ, and in Fig. 5.4, plotted as a function of q.

When the fundamental ellipse reduces to a circle, $A_p^{(m)}$ and $B_p^{(m)}$ tend to zero, unless $p = m$, in which case $A_m^{(m)}$ and $B_m^{(m)}$ tend to unity if $m \geq 1$, and $A_0^{(0)}$ tends to $2^{-1/2}$. It follows that Mathieu functions and modified Mathieu functions in that case reduce to

$$\mathrm{ce}_0(\eta, -q) \rightarrow \frac{1}{\sqrt{2}} \tag{5.44}$$

$$\mathrm{ce}_m(\eta, -q) \rightarrow \cos m\phi \quad (m \geq 1) \tag{5.45}$$

$$\mathrm{se}_m(\eta, -q) \rightarrow \sin m\phi \quad (m \geq 1) \tag{5.46}$$

$$\mathrm{Ce}_m(\xi, -q) \rightarrow M_m^c I_m(|k|\rho) \quad (m \geq 0) \tag{5.47}$$

$$\mathrm{Se}_m(\xi, -q) \rightarrow M_m^s I_m(|k|\rho) \quad (m \geq 1) \tag{5.48}$$

$$\mathrm{Fek}_m(\xi, -q) \rightarrow \frac{M_m^c}{\pi} K_m(|k|\rho) \quad (m \geq 0) \tag{5.49}$$

$$\mathrm{Gek}_m(\xi, -q) \rightarrow \frac{M_m^s}{\pi} K_m(|k|\rho) \quad (m \geq 1) \tag{5.50}$$

where ρ is the radius of the circle.

Throughout this chapter, the arguments of the Mathieu functions always contain $-q$. With this understood, we shall henceforth omit the $-q$.
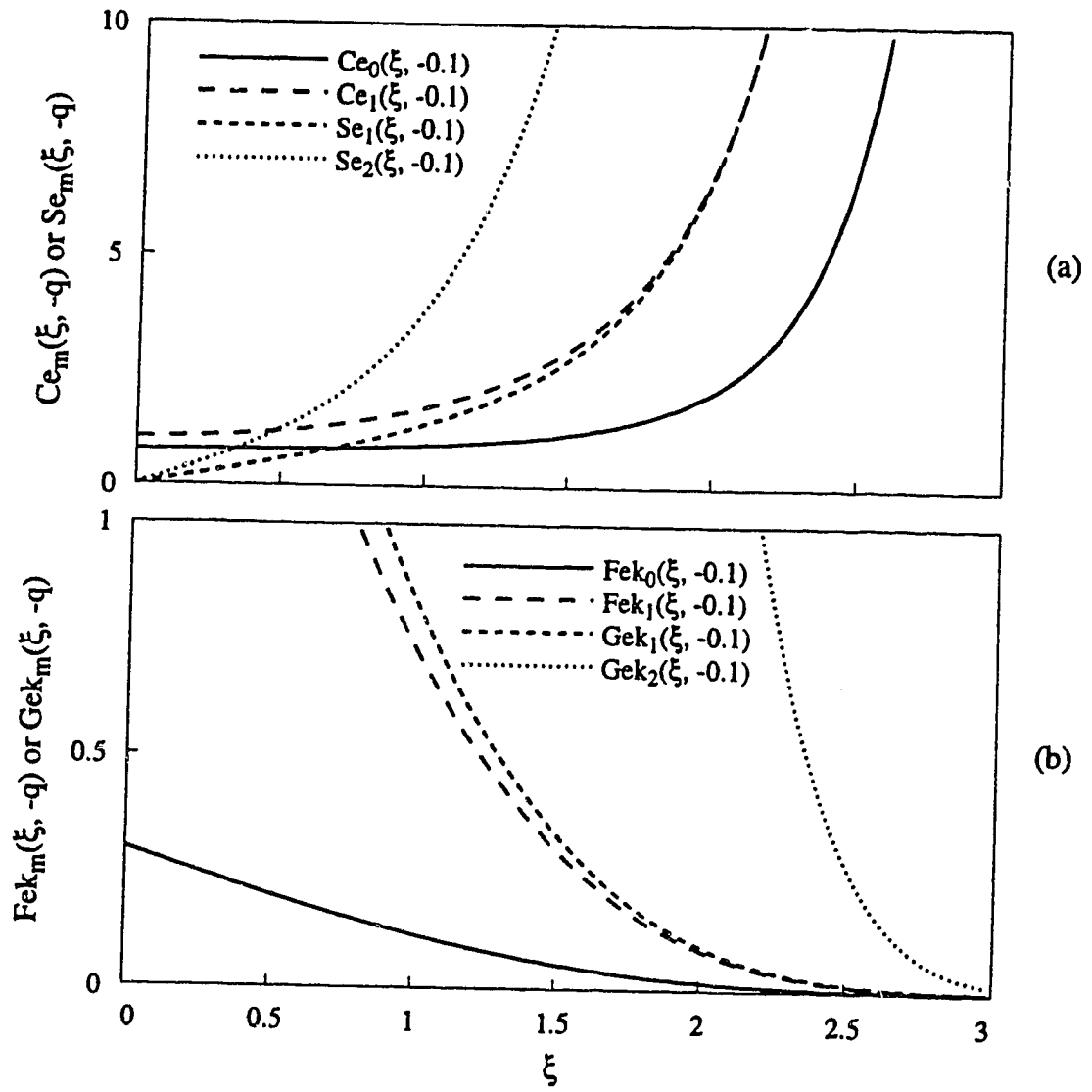
Figure 5.3: Graphs of the modified Mathieu functions (a) $Ce_0(\xi, -0.1)$, $Ce_1(\xi, -0.1)$, $Se_1(\xi, -0.1)$ and $Se_2(\xi, -0.1)$, and (b) $Fek_0(\xi, -0.1)$, $Fek_1(\xi, -0.1)$, $Gek_1(\xi, -0.1)$ and $Gek_2(\xi, -0.1)$, plotted as a function of ξ.
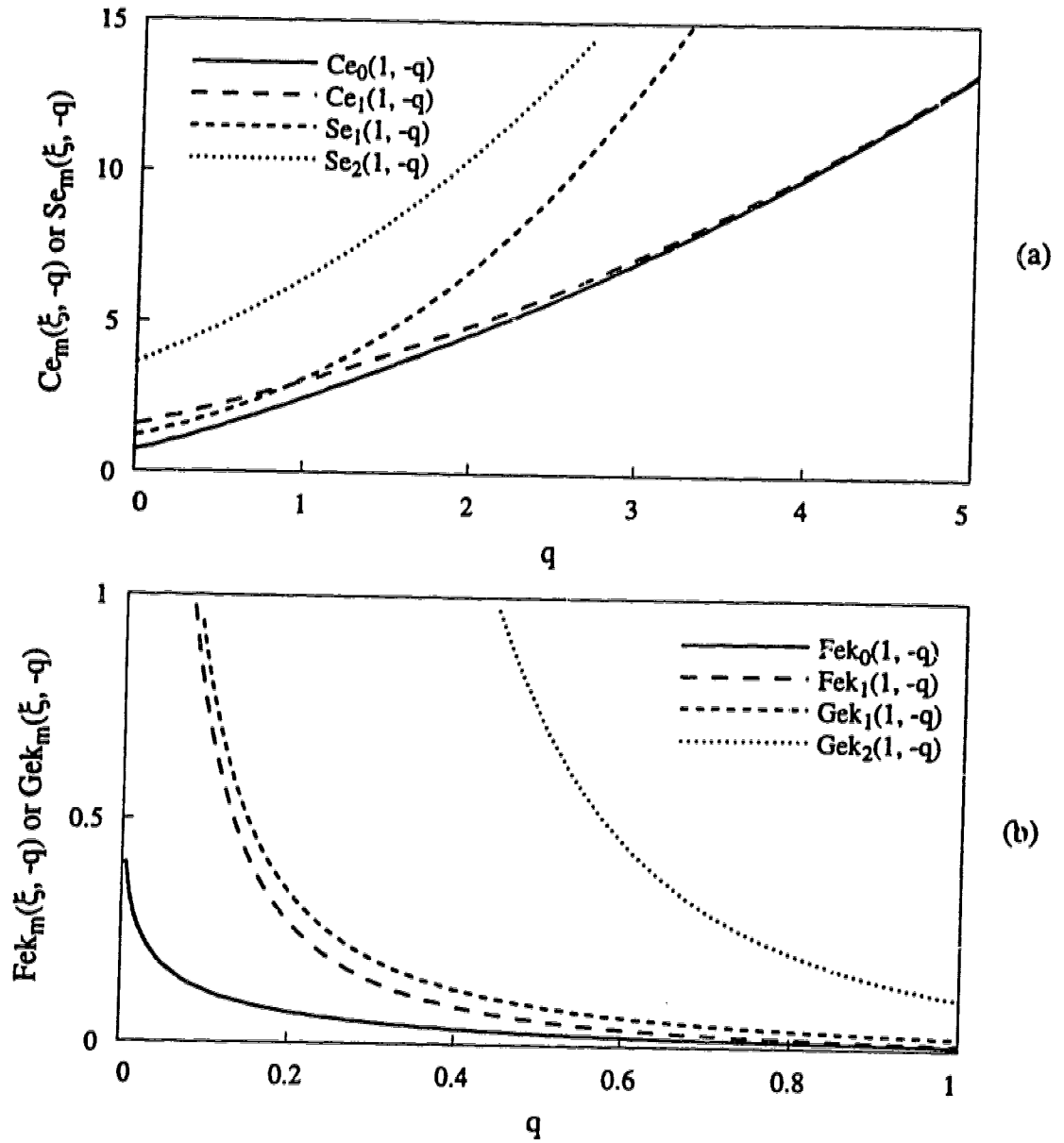
Figure 5.4: Graphs of the modified Mathieu functions (a) $Ce_0(1, -q)$, $Ce_1(1, -q)$, $Se_1(1, -q)$ and $Se_2(1, -q)$, and (b) $Fek_0(1, -q)$, $Fek_1(1, -q)$, $Gek_1(1, -q)$ and $Gek_2(1, -q)$, plotted as a function of q. Note the different abscissa scales in (a) and (b).

5.2.3 Expansion of Green's Function in Elliptic Cylinder Coordinates

The general method of expanding Green's function in different coordinate systems is well established [11]. However, the expansion in elliptic cylinder coordinates is not trivial. Although Petropoulos *et al.* [7] addressed this issue, they only quoted the final result. As will become apparent later in this thesis, we discovered several errors in the work of Petropoulos *et al.*, and so we present, in full, our derivation of the expansion of Green's function in elliptic cylinder coordinates.

Green's function $G(r, r') = |r - r'|^{-1}$ satisfies the equation

$$\nabla^2 G(r, r') = -4\pi\delta(r - r').$$ (5.51)

In elliptic cylinder coordinates, $\delta(r - r')$ can be written as

$$\delta(r - r') = N(r)\delta(\xi - \xi')\delta(\eta - \eta')\delta(z - z'),$$ (5.52)

where $N(r)$ can be determined using the normalization condition for $\delta(r - r')$

$$\int_V \delta(r - r')\, dV' = 1.$$ (5.53)

The volume element dV' in Eq. (5.53) is given by

$$dV' = c^2(\sinh^2\xi' + \sin^2\eta')\, d\xi'\, d\eta'\, dz'$$ (5.54)

in elliptic cylinder coordinates. Substituting Eqs. (5.52) and (5.54) in Eq. (5.53) and evaluating the integral yield

$$c^2(\sinh^2\xi + \sin^2\eta)N(r) = 1,$$ (5.55)

which leads to

$$N(r) = \frac{1}{c^2(\sinh^2\xi + \sin^2\eta)}.$$ (5.56)

By substituting Eq. (5.56) in Eq. (5.52), and using the identity

$$(\sinh^2\xi + \sin^2\eta) = \frac{1}{2}(\cosh 2\xi - \cos 2\eta),$$ (5.57)

$\delta(r - r')$ is found to be given by

$$\delta(r - r') = \frac{2}{c^2(\cosh 2\xi - \cos 2\eta)}\delta(\xi - \xi')\delta(\eta - \eta')\delta(z - z'). \qquad (5.58)$$

The z and η delta functions can be expressed in terms of orthonormal functions as follows

$$\delta(z - z') = \frac{1}{2\pi}\int_{-\infty}^{\infty} dk\, e^{ik(z-z')} \qquad (5.59)$$

$$\delta(\eta - \eta') = \frac{1}{\pi}\left[\sum_{m=0}^{\infty} \mathrm{ce}_m(\eta')\,\mathrm{ce}_m(\eta) + \sum_{m=1}^{\infty} \mathrm{se}_m(\eta')\,\mathrm{se}_m(\eta)\right]. \qquad (5.60)$$

Because of the symmetry of Green's function with respect to interchanging r and r', its expansion in elliptic cylinder coordinates can be written as

$$\begin{aligned}
G(r, r') &= \int_{-\infty}^{\infty} dk\, e^{ik(z-z')}\left[\sum_{m=0}^{\infty} g_m^c(\xi, \xi')\,\mathrm{ce}_m(\eta')\,\mathrm{ce}_m(\eta)\right.\\
&\quad \left. + \sum_{m=1}^{\infty} g_m^s(\xi, \xi')\,\mathrm{se}_m(\eta')\,\mathrm{se}_m(\eta)\right],
\end{aligned} \qquad (5.61)$$

where $g_m^c(\xi, \xi')$ and $g_m^s(\xi, \xi')$ are radial Green's functions. Substituting for $G(r, r')$ and the delta function in Eq. (5.51) using Eqs. (5.58) – (5.61), and noting that $\mathrm{ce}_m(\eta)$ and $\mathrm{se}_m(\eta)$ satisfy Mathieu's equation, yields

$$\begin{aligned}
&\int_{-\infty}^{\infty} dk\, e^{ik(z-z')}\left\{\sum_{m=0}^{\infty}\left[\frac{d^2 g_m^c}{d\xi^2} - (h_m^c + 2q\cosh 2\xi)g_m^c\right]\mathrm{ce}_m(\eta')\,\mathrm{ce}_m(\eta)\right.\\
&\quad \left. + \sum_{m=1}^{\infty}\left[\frac{d^2 g_m^s}{d\xi^2} - (h_m^s + 2q\cosh 2\xi)g_m^s\right]\mathrm{se}_m(\eta')\,\mathrm{se}_m(\eta)\right\}\\
&= \int_{-\infty}^{\infty} dk\, e^{ik(z-z')}\left\{\sum_{m=0}^{\infty}\left(-\frac{2}{\pi}\right)\delta(\xi - \xi')\,\mathrm{ce}_m(\eta')\,\mathrm{ce}_m(\eta)\right.\\
&\quad \left. + \sum_{m=1}^{\infty}\left(-\frac{2}{\pi}\right)\delta(\xi - \xi')\,\mathrm{se}_m(\eta')\,\mathrm{se}_m(\eta)\right\},
\end{aligned} \qquad (5.62)$$

where $h_m^c = a_m$ and $h_m^s = b_m$ if m is even, and $h_m^c = b_m$ and $h_m^s = a_m$ if m is odd. By equating the coefficients of $\mathrm{ce}_m(\eta)$ and $\mathrm{se}_m(\eta)$, the following differential equations for the radial Green's functions, $g_m^c(\xi, \xi')$ and $g_m^s(\xi, \xi')$, are obtained:

$$\frac{d^2 g_m^c}{d\xi^2} - (h_m^c + 2q\cosh 2\xi)g_m^c = -\frac{2}{\pi}\delta(\xi - \xi') \qquad (5.63)$$

$$\frac{d^2 g_m^s}{d\xi^2} - (h_m^s + 2q\cosh 2\xi)g_m^s = -\frac{2}{\pi}\delta(\xi - \xi'). \qquad (5.64)$$

94

Since Eqs. (5.63) and (5.64) are Mathieu's modified equations when $\xi \neq \xi'$, the radial Green's functions are of the form

$$g_m(\xi, \xi') = \varphi_1(\xi_<)\varphi_2(\xi_>), \qquad (5.65)$$

where φ_1 and φ_2 are two independent solutions of Mathieu's modified equation, and $\xi_<$ ($\xi_>$) is the smaller (larger) of ξ and ξ'. By substituting for g_m^c in Eq. (5.63) or for g_m^s in Eq. (5.64), and then integrating both sides with respect to ξ over the range $\xi' - \Delta \leq \xi \leq \xi' + \Delta$ with $\Delta \to 0$, the following discontinuity condition at $\xi = \xi'$ is obtained

$$\varphi_1(\xi')\varphi_2'(\xi') - \varphi_1'(\xi')\varphi_2(\xi') = -\frac{2}{\pi}, \qquad (5.66)$$

which is satisfied for all values of ξ'. Since $g_m(\xi, \xi')$ must be finite at ξ or $\xi' = 0$, and must vanish as ξ or $\xi' \to \infty$, it follows from the properties of modified Mathieu functions that $\varphi_1(\xi_<) = A\,\mathrm{Ce}_m(\xi_<)$ and $\varphi_2(\xi_>) = \mathrm{Fek}_m(\xi_>)$, or $\varphi_1(\xi_<) = B\,\mathrm{Se}_m(\xi_<)$ and $\varphi_2(\xi_>) = \mathrm{Gek}_m(\xi_>)$, where A and B are constants to be determined from Eq. (5.66). By substituting for φ_1 and φ_2 and then evaluating the left side of Eq. (5.66) as $\xi' \to \infty$, it is found that

$$A\,\mathrm{Ce}_m(\xi')\,\mathrm{Fek}_m'(\xi') - A\,\mathrm{Ce}_m'(\xi')\,\mathrm{Fek}_m(\xi') = -\frac{A}{\pi}(M_m^c)^2 \qquad (5.67)$$

$$B\,\mathrm{Se}_m(\xi')\,\mathrm{Gek}_m'(\xi') - B\,\mathrm{Se}_m'(\xi')\,\mathrm{Gek}_m(\xi') = -\frac{B}{\pi}(M_m^s)^2, \qquad (5.68)$$

so that Eq. (5.66) becomes

$$-\frac{A}{\pi}(M_m^c)^2 = -\frac{2}{\pi} \quad \text{and} \quad -\frac{B}{\pi}(M_m^s)^2 = -\frac{2}{\pi}. \qquad (5.69)$$

From Eq. (5.69), A and B are found to be

$$A = \frac{2}{(M_m^c)^2} \quad \text{or} \quad B = \frac{2}{(M_m^s)^2}. \qquad (5.70)$$

Thus, the radial Green's functions are given by

$$g_m^c(\xi, \xi') = \frac{2}{(M_m^c)^2}\,\mathrm{Ce}_m(\xi_<)\,\mathrm{Fek}_m(\xi_>) \qquad (5.71)$$

$$g_m^s(\xi, \xi') = \frac{2}{(M_m^s)^2}\,\mathrm{Se}_m(\xi_<)\,\mathrm{Gek}_m(\xi_>). \qquad (5.72)$$

95

Substituting for $g_m^c(\xi, \xi')$ and $g_m^s(\xi, \xi')$ in Eq. (5.61) using Eqs. (5.71) and (5.72) yields the expansion of Green's function in elliptic coordinates

$$G(\boldsymbol{r}, \boldsymbol{r}') = 2 \int_{-\infty}^{\infty} dk \, e^{ik(z-z')} \left[\sum_{m=0}^{\infty} \frac{1}{(M_m^c)^2} \, ce_m(\eta) \, ce_m(\eta') \, Ce_m(\xi_<) \, Fek_m(\xi_>) \right.$$
$$\left. + \sum_{m=1}^{\infty} \frac{1}{(M_m^s)^2} \, se_m(\eta) \, se_m(\eta') \, Se_m(\xi_<) \, Gek_m(\xi_>) \right]. \tag{5.73}$$

This expression is in agreement with the Green's function expansion given by Petropoulos *et al.* [7], except that $(s'_{2n+1})^2$ in the last term of their expression should read $(s'_{2n+2})^2$, obviously a typographical error.

5.2.4 Magnetic Field Generated by an Elliptic Cylinder Coil

We shall ignore displacement currents since the switching rate of magnetic field gradients in MRI and MRS is only of the order of kiloHertz. The vector potential at $\boldsymbol{r}$ due to a current density $\boldsymbol{J}(\boldsymbol{r}')$ at $\boldsymbol{r}'$ on the surface of an elliptic cylinder is therefore given by the volume integral

$$\boldsymbol{A}(\boldsymbol{r}) = \frac{\mu_0}{4\pi} \int_V \frac{\boldsymbol{J}(\boldsymbol{r}') \, dV'}{|\boldsymbol{r} - \boldsymbol{r}'|}. \tag{5.74}$$

Since the current is confined to the surface of an elliptical cylinder characterized by $\xi' = \xi_0$, say, $\boldsymbol{J}(\boldsymbol{r}')$ can be expressed as

$$\boldsymbol{J}(\boldsymbol{r}') = \boldsymbol{j}(\eta', z') \frac{\delta(\xi' - \xi_0)}{c(\sinh^2 \xi' + \sin^2 \eta')^{1/2}}, \tag{5.75}$$

where $\boldsymbol{j}(\eta', z')$ is the surface current density. In cartesian coordinates, the surface current density has all the three components, $j_{x'}$, $j_{y'}$ and $j_{z'}$, whereas in elliptic cylinder coordinates, it has only two, namely

$$\boldsymbol{j}(\eta', z') = j_{\eta'}(\eta', z') \boldsymbol{e}_{\eta'} + j_{z'}(\eta', z') \boldsymbol{e}_{z'} \tag{5.76}$$

where $\boldsymbol{e}_{\eta'}$ and $\boldsymbol{e}_{z'}$ are unit vectors in the η' and z' directions, and $j_{\eta'}(\eta', z')$ and $j_{z'}(\eta', z')$ are the azimuthal and axial components. Substituting for dV' and $\boldsymbol{J}(\boldsymbol{r}')$

in Eq. (5.74) using Eqs. (5.54)and (5.75) yields

$$A(r) = \frac{\mu_0 c}{4\pi} \int_{-\infty}^{\infty} dz' \int_{-\pi}^{\pi} d\eta' \, j(\eta', z') \frac{(\sinh^2 \xi_0 + \sin^2 \eta')^{1/2}}{|r - r'|_{\xi'=\xi_0}}, \tag{5.77}$$

whose three cartesian components are given by

$$A_x(r) = \frac{\mu_0 c}{4\pi} \int_{-\infty}^{\infty} dz' \int_{-\pi}^{\pi} d\eta' \, j_{x'}(\eta', z') \frac{(\sinh^2 \xi_0 + \sin^2 \eta')^{1/2}}{|r - r'|_{\xi'=\xi_0}} \tag{5.78}$$

$$A_y(r) = \frac{\mu_0 c}{4\pi} \int_{-\infty}^{\infty} dz' \int_{-\pi}^{\pi} d\eta' \, j_{y'}(\eta', z') \frac{(\sinh^2 \xi_0 + \sin^2 \eta')^{1/2}}{|r - r'|_{\xi'=\xi_0}} \tag{5.79}$$

$$A_z(r) = \frac{\mu_0 c}{4\pi} \int_{-\infty}^{\infty} dz' \int_{-\pi}^{\pi} d\eta' \, j_{z'}(\eta', z') \frac{(\sinh^2 \xi_0 + \sin^2 \eta')^{1/2}}{|r - r'|_{\xi'=\xi_0}}. \tag{5.80}$$

By using Eqs. (5.6) – (5.9), and noting that $j(\eta', z')$ has no radial component, the radial and azimuthal components of the vector potential, $A_\xi(\xi, \eta, z)$ and $A_\eta(\xi, \eta, z)$, are found to be

$$A_\xi(\xi, \eta, z) = \frac{\mu_0 c}{4\pi(\sinh^2 \xi + \sin^2 \eta)^{1/2}} \int_{-\infty}^{\infty} dz' \int_{-\pi}^{\pi} d\eta' \, j_{\eta'}(\eta', z')$$
$$\times \frac{\cosh \xi \sin \eta \sinh \xi_0 \cos \eta' - \sinh \xi \cos \eta \cosh \xi_0 \sin \eta'}{|r - r'|_{\xi'=\xi_0}} \tag{5.81}$$

$$A_\eta(\xi, \eta, z) = \frac{\mu_0 c}{4\pi(\sinh^2 \xi + \sin^2 \eta)^{1/2}} \int_{-\infty}^{\infty} dz' \int_{-\pi}^{\pi} d\eta' \, j_{\eta'}(\eta', z')$$
$$\times \frac{\cosh \xi \sin \eta \cosh \xi_0 \sin \eta' + \sinh \xi \cos \eta \sinh \xi_0 \cos \eta'}{|r - r'|_{\xi'=\xi_0}}. \tag{5.82}$$

By substituting for $|r - r'|^{-1}$ in Eqs. (5.80) – (5.82) using Eq. (5.73), and evaluating the integrals in these equations, the components of the vector potential in elliptic cylinder coordinates become

$$A_\xi(\xi, \eta, z) = \frac{\mu_0 c}{(\sinh^2 \xi + \sin^2 \eta)^{1/2}} \int_{-\infty}^{\infty} dk \, e^{ikz}$$

$$\times \left\{ \sum_{m=0}^{\infty} F_m \left[\cosh \xi \sin \eta \sinh \xi_0 \, u_m^c(k) - \sinh \xi \cos \eta \cosh \xi_0 \, u_m^s(k) \right] \right.$$

$$\left. + \sum_{m=1}^{\infty} G_m \left[\cosh \xi \sin \eta \sinh \xi_0 \, v_m^c(k) - \sinh \xi \cos \eta \cosh \xi_0 \, v_m^s(k) \right] \right\}, \tag{5.83}$$

$$A_\eta(\xi, \eta, z) = \frac{\mu_0 c}{(\sinh^2 \xi + \sin^2 \eta)^{1/2}} \int_{-\infty}^{\infty} dk \, e^{ikz}$$

97

$$\times \left\{ \sum_{m=0}^{\infty} F_m \left[\sinh \xi \cos \eta \sinh \xi_0 \, u_m^c(k) + \cosh \xi \sin \eta \cosh \xi_0 \, u_m^s(k) \right] \right.$$

$$\left. + \sum_{m=1}^{\infty} G_m \left[\sinh \xi \cos \eta \sinh \xi_0 \, v_m^c(k) + \cosh \xi \sin \eta \cosh \xi_0 \, v_m^s(k) \right] \right\}, \quad (5.84)$$

$$A_z(\xi, \eta, z) = \mu_0 c \int_{-\infty}^{\infty} dk \, e^{ikz} \left[\sum_{m=0}^{\infty} F_m w_m^c(k) + \sum_{m=1}^{\infty} G_m w_m^s(k) \right]. \quad (5.85)$$

Here

$$F_m = \frac{1}{(M_m^c)^2} \, \mathrm{ce}_m(\eta) \, \mathrm{Ce}_m(\xi_<) \, \mathrm{Fek}_m(\xi_>) \quad (5.86)$$

$$G_m = \frac{1}{(M_m^s)^2} \, \mathrm{se}_m(\eta) \, \mathrm{Se}_m(\xi_<) \, \mathrm{Gek}_m(\xi_>) \quad (5.87)$$

$$u_m^c(k) = \frac{1}{2\pi} \int_{-\infty}^{\infty} dz' \, e^{-ikz'} \int_{-\pi}^{\pi} d\eta' \, j_{\eta'}(\eta', z') \cos \eta' \, \mathrm{ce}_m(\eta') \quad (5.88)$$

$$v_m^c(k) = \frac{1}{2\pi} \int_{-\infty}^{\infty} dz' \, e^{-ikz'} \int_{-\pi}^{\pi} d\eta' \, j_{\eta'}(\eta', z') \cos \eta' \, \mathrm{se}_m(\eta') \quad (5.89)$$

$$u_m^s(k) = \frac{1}{2\pi} \int_{-\infty}^{\infty} dz' \, e^{-ikz'} \int_{-\pi}^{\pi} d\eta' \, j_{\eta'}(\eta', z') \sin \eta' \, \mathrm{ce}_m(\eta') \quad (5.90)$$

$$v_m^s(k) = \frac{1}{2\pi} \int_{-\infty}^{\infty} dz' \, e^{-ikz'} \int_{-\pi}^{\pi} d\eta' \, j_{\eta'}(\eta', z') \sin \eta' \, \mathrm{se}_m(\eta') \quad (5.91)$$

$$w_m^c(k) = \frac{1}{2\pi} \int_{-\infty}^{\infty} dz' \, e^{-ikz'} \int_{-\pi}^{\pi} d\eta' \, j_{z'}(\eta', z')(\sinh^2 \xi_0 + \sin^2 \eta')^{1/2} \, \mathrm{ce}_m(\eta') \quad (5.92)$$

$$w_m^s(k) = \frac{1}{2\pi} \int_{-\infty}^{\infty} dz' \, e^{-ikz'} \int_{-\pi}^{\pi} d\eta' \, j_{z'}(\eta', z')(\sinh^2 \xi_0 + \sin^2 \eta')^{1/2} \, \mathrm{se}_m(\eta'), \quad (5.93)$$

where $\xi_<$ ($\xi_>$) is the smaller (larger) of ξ and ξ_0. By comparing Eqs. (5.88) – (5.93) with Eqs. (5.30) and (5.31), noting that the first integral in each of Eqs. (5.88) – (5.93) is a Fourier integral with respect to z', it can be seen that $u_m^c(k)$, $v_m^c(k)$, $u_m^s(k)$, $v_m^s(k)$, $w_m^c(k)$ and $w_m^s(k)$ are, respectively, coefficients of Mathieu-Fourier expansions of $j_{\eta'}(\eta', z') \cos \eta'$, $j_{\eta'}(\eta', z') \sin \eta'$ and $j_{z'}(\eta', z')(\sinh^2 \xi_0 + \sin^2 \eta')^{1/2}$, differing at most by a normalization factor. It can be shown, using Eqs (5.29) – (5.31) and Fourier transformation, that

$$j_{\eta'}(\eta', z') \cos \eta' = \frac{1}{\pi} \int_{-\infty}^{\infty} dk \, e^{ikz'} \left[\sum_{m=0}^{\infty} u_m^c(k) \, \mathrm{ce}_m(\eta') + \sum_{m=1}^{\infty} v_m^c(k) \, \mathrm{se}_m(\eta') \right] \quad (5.94)$$

$$j_{\eta'}(\eta', z') \sin \eta' = \frac{1}{\pi} \int_{-\infty}^{\infty} dk \, e^{ikz'} \left[\sum_{m=0}^{\infty} u_m^s(k) \, \mathrm{ce}_m(\eta') + \sum_{m=1}^{\infty} v_m^s(k) \, \mathrm{se}_m(\eta') \right] \quad (5.95)$$

$$j_{z'}(\eta', z')(\sinh^2 \xi_0 + \sin^2 \eta')^{1/2}$$

$$= \frac{1}{\pi} \int_{-\infty}^{\infty} dk \, e^{ikz'} \left[\sum_{m=0}^{\infty} w_m^c(k) \, ce_m(\eta') + \sum_{m=1}^{\infty} w_m^s(k) \, se_m(\eta') \right]. \tag{5.96}$$

The z component of the magnetic field inside the coil, found by taking the curl of the vector potential, is given by

$$B_z(\xi, \eta, z) = (\nabla \times \boldsymbol{A})_z$$

$$= \frac{\mu_0}{\sinh^2 \xi + \sin^2 \eta} \int_{-\infty}^{\infty} dk \, e^{ikz} \left\{ \sum_{m=0}^{\infty} \frac{u_m^c(k)}{(M_m^c)^2} \sinh \xi_0 \, \mathrm{Fek}_m(\xi_0) \right.$$

$$\times \left[\sinh \xi \cos \eta \, \mathrm{Ce}_m'(\xi) \, ce_m(\eta) - \cosh \xi \sin \eta \, \mathrm{Ce}_m(\xi) \, ce_m'(\eta) \right]$$

$$+ \sum_{m=0}^{\infty} \frac{u_m^s(k)}{(M_m^c)^2} \cosh \xi_0 \, \mathrm{Fek}_m(\xi_0)$$

$$\times \left[\cosh \xi \sin \eta \, \mathrm{Ce}_m'(\xi) \, ce_m(\eta) + \sinh \xi \cos \eta \, \mathrm{Ce}_m(\xi) \, ce_m'(\eta) \right]$$

$$+ \sum_{m=1}^{\infty} \frac{v_m^c(k)}{(M_m^s)^2} \sinh \xi_0 \, \mathrm{Gek}_m(\xi_0)$$

$$\times \left[\sinh \xi \cos \eta \, \mathrm{Se}_m'(\xi) \, se_m(\eta) - \cosh \xi \sin \eta \, \mathrm{Se}_m(\xi) \, se_m'(\eta) \right]$$

$$+ \sum_{m=1}^{\infty} \frac{v_m^s(k)}{(M_m^s)^2} \cosh \xi_0 \, \mathrm{Gek}_m(\xi_0)$$

$$\left. \times \left[\cosh \xi \sin \eta \, \mathrm{Se}_m'(\xi) \, se_m(\eta) + \sinh \xi \cos \eta \, \mathrm{Se}_m(\xi) \, se_m'(\eta) \right] \right\}. \tag{5.97}$$

Here, the primes in $\mathrm{Se}_m'(\xi)$ and $\mathrm{Ce}_m'(\xi)$ signify derivatives with respect to ξ (in contrast to their use in Ref. [7]). The magnetic field outside the coil ($\xi > \xi_0$) can be obtained by replacing $\mathrm{Fek}_m(\xi_0)$ by $\mathrm{Ce}_m(\xi_0)$, $\mathrm{Ce}_m(\xi)$ by $\mathrm{Fek}_m(\xi)$, $\mathrm{Ce}_m'(\xi)$ by $\mathrm{Fek}_m'(\xi)$, $\mathrm{Gek}_m(\xi_0)$ by $\mathrm{Se}_m(\xi_0)$, $\mathrm{Se}_m(\xi)$ by $\mathrm{Gek}_m(\xi)$, and $\mathrm{Se}_m'(\xi)$ by $\mathrm{Gek}_m'(\xi)$ in Eq. (5.97).

5.2.5 Stored Energy in an Elliptic Cylinder Coil

Since the general expression for the stored magnetic energy in an elliptic cylinder coil had not been obtained previously, we present our derivation in some detail.

The stored energy in an elliptic cylinder coil is given by

$$W = \frac{1}{2} \int_V \boldsymbol{A} \cdot \boldsymbol{J} \, dV$$

$$= \frac{c}{2} \int_{-\infty}^{\infty} dz \int_{-\pi}^{\pi} d\eta \, (\sinh^2 \xi_0 + \sin^2 \eta)^{1/2} (A_\eta j_\eta + A_z j_z)_{\xi = \xi_0} \tag{5.98}$$

using Eqs. (5.54) and (5.75). The $A_\eta j_\eta$ term can be expressed as

$$
(\sinh^2 \xi_0 + \sin^2 \eta)^{1/2} (A_\eta j_\eta)_{\xi=\xi_0}
$$

$$
= \mu_0 c \int_{-\infty}^{\infty} dk\, e^{ikz} \left\{ \sum_{m=0}^{\infty} \frac{\mathrm{ce}_m(\eta)\, \mathrm{Ce}_m(\xi_0)\, \mathrm{Fek}_m(\xi_0)}{(M_m^c)^2} \right.
$$

$$
\times \left[j_\eta \cos \eta \sinh^2 \xi_0\, u_m^c(k) + j_\eta \sin \eta \cosh^2 \xi_0\, u_m^s(k) \right]
$$

$$
+ \sum_{m=1}^{\infty} \frac{\mathrm{se}_m(\eta)\, \mathrm{Se}_m(\xi_0)\, \mathrm{Gek}_m(\xi_0)}{(M_m^s)^2}
$$

$$
\left. \times \left[j_\eta \cos \eta \sinh^2 \xi_0\, v_m^c(k) + j_\eta \sin \eta \cosh^2 \xi_0\, v_m^s(k) \right] \right\}, \qquad (5.99)
$$

using Eq. (5.84). By substituting for $j_\eta \cos \eta$ and $j_\eta \sin \eta$ using Eqs (5.94) and (5.95), and noting that $u_m^c(-k) = [u_m^c(k)]^*$, $u_m^s(-k) = [u_m^s(k)]^*$, $v_m^c(-k) = [v_m^c(k)]^*$ and $v_m^s(-k) = [v_m^s(k)]^*$, one obtains

$$
\int_{-\infty}^{\infty} dz \int_{-\pi}^{\pi} d\eta \left(\sinh^2 \xi_0 + \sin^2 \eta \right)^{1/2} (A_\eta j_\eta)_{\xi=\xi_0}
$$

$$
= 2\pi \mu_0 c \int_{-\infty}^{\infty} dk \left\{ \sum_{m=0}^{\infty} \frac{\mathrm{Ce}_m(\xi_0)\, \mathrm{Fek}_m(\xi_0)}{(M_m^c)^2} \left[\sinh^2 \xi_0\, |u_m^c(k)|^2 + \cosh^2 \xi_0\, |u_m^s(k)|^2 \right] \right.
$$

$$
\left. + \sum_{m=1}^{\infty} \frac{\mathrm{Se}_m(\xi_0)\, \mathrm{Gek}_m(\xi_0)}{(M_m^s)^2} \left[\sinh^2 \xi_0\, |v_m^c(k)|^2 + \cosh^2 \xi_0\, |v_m^s(k)|^2 \right] \right\}. \qquad (5.100)
$$

Similarly, the $A_z j_z$ term in Eq. (5.98) is found to be

$$
\int_{-\infty}^{\infty} dz \int_{-\pi}^{\pi} d\eta \left(\sinh^2 \xi_0 + \sin^2 \eta \right)^{1/2} (A_z j_z)_{\xi=\xi_0}
$$

$$
= 2\pi \mu_0 c \int_{-\infty}^{\infty} dk \left\{ \sum_{m=0}^{\infty} \frac{\mathrm{Ce}_m(\xi_0)\, \mathrm{Fek}_m(\xi_0)}{(M_m^c)^2} |w_m^c(k)|^2 \right.
$$

$$
\left. + \sum_{m=1}^{\infty} \frac{\mathrm{Se}_m(\xi_0)\, \mathrm{Gek}_m(\xi_0)}{(M_m^s)^2} |w_m^s(k)|^2 \right\}. \qquad (5.101)
$$

Thus, the general expression for the stored energy in an elliptic cylinder coil is given by

$$
W = \pi \mu_0 c^2 \int_{-\infty}^{\infty} dk \left\{ \sum_{m=0}^{\infty} \frac{\mathrm{Ce}_m(\xi_0)\, \mathrm{Fek}_m(\xi_0)}{(M_m^c)^2} \right.
$$

$$
\times \left[\sinh^2 \xi_0\, |u_m^c(k)|^2 + \cosh^2 \xi_0\, |u_m^s(k)|^2 + |w_m^c(k)|^2 \right]
$$

$$
+ \sum_{m=1}^{\infty} \frac{\mathrm{Se}_m(\xi_0)\, \mathrm{Gek}_m(\xi_0)}{(M_m^s)^2}
$$

$$
\left. \times \left[\sinh^2 \xi_0\, |v_m^c(k)|^2 + \cosh^2 \xi_0\, |v_m^s(k)|^2 + |w_m^s(k)|^2 \right] \right\}. \qquad (5.102)
$$

5.2.6 General Characteristics of a Current Distributed on the Surface of an Elliptic Cylinder

In designing an elliptic cylinder coil to generate a specific field profile, for example a uniform field B_z, a uniform field gradient, or a higher order shim field, it is necessary to choose the η dependence of $j_\eta(\eta, z)$ appropriately. To conform to the symmetry of the elliptical cylinder, $j_\eta(\eta, z)$, for a uniform B_z or a z gradient, $\partial B_z / \partial z$, will be of the form

$$j_\eta(\eta, z) = \sum_{m=0}^{\infty} C_m(z) \cos m\eta \qquad (5.103)$$

with m even and the $m = 0$ term dominant. To generate an x gradient, $\partial B_z / \partial x$, $j_\eta(\eta, z)$ will be given by Eq. (5.103) with m odd and the $m = 1$ term dominant. For a y gradient, $\partial B_z / \partial y$, $j_\eta(\eta, z)$ will be of the form

$$j_\eta(\eta, z) = \sum_{m=1}^{\infty} S_m(z) \sin m\eta \qquad (5.104)$$

with m again odd and the $m = 1$ term dominant.

A simple way to determine the z dependence of $C_m(z)$ or $S_m(z)$ is to assume that $j_\eta(\eta, z)$ is separable, i.e. of the form $\alpha(\eta)\beta(z)$, so that the η dependence is independent of z. If the relative amplitudes of the various orders are arbitrarily chosen, the z dependence can be determined using the target field approach [4], and the optimal values of the relative amplitudes found by trial and error.

The axial component of the current density, $j_z(\eta, z)$, can be determined from $j_\eta(\eta, z)$ using the continuity condition $\nabla \cdot \boldsymbol{J} = 0$. By taking the divergence of $\boldsymbol{J}$ given in Eq. (5.75), one finds that

$$\frac{\partial j_\eta}{\partial \eta} + c\sqrt{\sinh^2 \xi_0 + \sin^2 \eta}\, \frac{\partial j_z}{\partial z} = 0. \qquad (5.105)$$

It is now necessary to introduce the Mathieu-Fourier transforms of the current density defined as

$$j_\eta^{c,n}(k) = \frac{1}{2\pi} \int_{-\infty}^{\infty} dz\, e^{-ikz} \int_{-\pi}^{\pi} d\eta\, j_\eta(\eta, z)\, \mathrm{ce}_n(\eta) \qquad (5.106)$$

$$j_\eta^{s,n}(k) = \frac{1}{2\pi} \int_{-\infty}^{\infty} dz\, e^{-ikz} \int_{-\pi}^{\pi} d\eta\, j_\eta(\eta, z)\, \text{se}_n(\eta). \tag{5.107}$$

The corresponding inverse transform is given by

$$j_\eta(\eta, z) = \frac{1}{\pi} \int_{-\infty}^{\infty} dk\, e^{ikz} \left[\sum_{n=0}^{\infty} j_\eta^{c,n}(k)\, \text{ce}_n(\eta) + \sum_{n=1}^{\infty} j_\eta^{s,n}(k)\, \text{se}_n(\eta) \right]. \tag{5.108}$$

By differentiation with respect to η, it is found that

$$\frac{\partial j_\eta}{\partial \eta} = \frac{1}{\pi} \int_{-\infty}^{\infty} dk\, e^{ikz} \left[\sum_{n=0}^{\infty} j_\eta^{c,n}(k)\, \text{ce}_n'(\eta) + \sum_{n=1}^{\infty} j_\eta^{s,n}(k)\, \text{se}_n'(\eta) \right]. \tag{5.109}$$

The derivatives $\text{ce}_n'(\eta)$ and $\text{se}_n'(\eta)$ can now be expressed in terms of Mathieu functions by

$$\text{ce}_n'(\eta) = \sum_{m=1}^{\infty} \mu_{n,m}\, \text{se}_m(\eta), \quad \text{where} \quad \mu_{n,m} = \frac{1}{\pi} \int_{-\pi}^{\pi} d\eta\, \text{ce}_n'(\eta)\, \text{se}_m(\eta) \tag{5.110}$$

$$\text{se}_n'(\eta) = \sum_{m=0}^{\infty} \nu_{n,m}\, \text{ce}_m(\eta), \quad \text{where} \quad \nu_{n,m} = \frac{1}{\pi} \int_{-\pi}^{\pi} d\eta\, \text{se}_n'(\eta)\, \text{ce}_m(\eta), \tag{5.111}$$

where $(m + n)$ must be an even integer. Thus, when n is even (odd), m is even (odd). Since

$$\int_{-\pi}^{\pi} d\eta\, \text{ce}_n'(\eta)\, \text{se}_m(\eta) = -\int_{-\pi}^{\pi} d\eta\, \text{se}_m'(\eta)\, \text{ce}_n(\eta), \tag{5.112}$$

as can be shown by integration by parts, it follows that $\mu_{n,m} = -\nu_{m,n}$ so that

$$\text{ce}_n'(\eta) = -\sum_{m=1}^{\infty} \nu_{m,n}\, \text{se}_m(\eta). \tag{5.113}$$

Substituting for $\text{se}_n'(\eta)$ and $\text{ce}_n'(\eta)$ in Eq. (5.109) using Eqs.(5.111) and (5.113) yields

$$\frac{\partial j_\eta}{\partial \eta} = \frac{1}{\pi} \int_{-\infty}^{\infty} dk\, e^{ikz} \left\{ \sum_{m=0}^{\infty} \left[\sum_n \nu_{n,m} j_\eta^{s,n}(k) \right] \text{ce}_m(\eta) \right.$$
$$\left. + \sum_{m=1}^{\infty} \left[-\sum_n \nu_{m,n} j_\eta^{c,n}(k) \right] \text{se}_m(\eta) \right\}, \tag{5.114}$$

where the summation over n is from 0 to ∞, with the restriction that $(m + n)$ is even. By substituting the expression for $\partial j_\eta / \partial \eta$, and the expression for $\partial j_z / \partial z$

obtained by differentiating Eq. (5.96), in Eq. (5.105), it is found that, to satisfy the continuity condition for the surface current density,

$$\frac{1}{\pi} \int_{-\infty}^{\infty} dk\, e^{ikz} \left\{ \sum_{m=0}^{\infty} \left[ikcw_m^c(k) + \sum_n \nu_{n,m} j_\eta^{s,n}(k) \right] ce_m(\eta) \right. $$
$$\left. + \sum_{m=1}^{\infty} \left[ikcw_m^s(k) - \sum_n \nu_{m,n} j_\eta^{c,n}(k) \right] se_m(\eta) \right\} = 0, \quad (5.115)$$

from which

$$w_m^c(k) = -\frac{1}{ikc} \sum_n \nu_{n,m} j_\eta^{s,n}(k) \qquad (5.116)$$

$$w_m^s(k) = \frac{1}{ikc} \sum_n \nu_{m,n} j_\eta^{c,n}(k). \qquad (5.117)$$

It can be seen that Eqs. (5.116) and (5.117) relate $w_m^c(k)$ and $w_m^s(k)$ (which are determined by $j_z(\eta, z)$ via Eqs. (5.92) and (5.93)) to $j_\eta^{s,n}(k)$ and $j_\eta^{c,n}(k)$ (which are determined by $j_\eta(\eta, z)$ via Eqs. (5.106) and (5.107)). Thus, if $j_\eta(\eta, z)$ is known or specified, the corresponding $j_z(\eta, z)$ can be found using Eqs. (5.106), (5.107), (5.116) and (5.117), followed by Eq. (5.96).

5.2.7 Magnetic Field of an Elliptic Cylinder z Gradient Coil with Purely Azimuthal Current Flow

If the current in an elliptic cylinder coil is entirely azimuthal so that $j_{z'} = 0$ everywhere, $w_m^c(k)$ and $w_m^s(k)$, defined in Eqs. (5.92) and (5.93) are obviously zero. Moreover, $v_m^c(k)$ and $u_m^s(k)$ are also zero because the integrands in Eqs. (5.89) and (5.90) are odd functions of η. The only non-zero $u_m^c(k)$ and $v_m^s(k)$ occur when m is odd. This can be seen by noting that $ce_m(\eta')$ and $se_m(\eta')$ in the expressions for $u_m^c(k)$ and $v_m^s(k)$ (Eqs. (5.88) and (5.91)) contain terms involving either $\cos m'\eta$ or $\sin m'\eta$, where m' is even (odd) if m is even (odd), as can be seen in Eqs. (5.16) – (5.19). Therefore, the integrands in Eqs. (5.88) and (5.91) contain either $\cos \eta' \cos m'\eta'$ or $\sin \eta' \sin m'\eta'$. The integrals with respect to η' in these equations are nonzero only

if $m' = 1$. Hence m must be odd. In this case, it can be shown by performing the integrations that

$$u_m^c(k) = (-1)^{(m-1)/2} \frac{B_1^{(m)}}{2} j_\eta(k) \qquad (5.118)$$

$$v_m^s(k) = (-1)^{(m-1)/2} \frac{A_1^{(m)}}{2} j_\eta(k), \qquad (5.119)$$

where $j_\eta(k)$ is the Fourier transform of $j_{\eta'}(z')$ given by

$$j_\eta(k) = \int_{-\infty}^{\infty} dz' \, j_{\eta'}(z') e^{-ikz'}. \qquad (5.120)$$

It follows from Eq. (5.97) that, for a purely azimuthal current,

$$B_z(\xi, \eta, z) = \frac{\mu_0}{2} \int_{-\infty}^{\infty} dk \, e^{ikz} j_\eta(k) P_z(\xi, \eta, \xi_0, q). \qquad (5.121)$$

Here $P_z(\xi, \eta, \xi_0, q)$ is given by

$$P_z(\xi, \eta, \xi_0, q) = \sum_{m=odd}^{\infty} (-1)^{(m-1)/2} \left[\frac{\beta_m B_1^{(m)}}{(M_m^c)^2} \sinh \xi_0 \, \mathrm{Fek}_m(\xi_0) \right.$$
$$\left. + \frac{\alpha_m A_1^{(m)}}{(M_m^s)^2} \cosh \xi_0 \, \mathrm{Gek}_m(\xi_0) \right], \qquad (5.122)$$

where m is restricted to odd positive integers, and

$$\alpha_m = \frac{\cosh \xi \sin \eta \, \mathrm{Se}_m'(\xi) \, \mathrm{se}_m(\eta) + \sinh \xi \cos \eta \, \mathrm{Se}_m(\xi) \, \mathrm{se}_m'(\eta)}{\sinh^2 \xi + \sin^2 \eta} \qquad (5.123)$$

$$\beta_m = \frac{\sinh \xi \cos \eta \, \mathrm{Ce}_m'(\xi) \, \mathrm{ce}_m(\eta) - \cosh \xi \sin \eta \, \mathrm{Ce}_m(\xi) \, \mathrm{ce}_m'(\eta)}{\sinh^2 \xi + \sin^2 \eta}. \qquad (5.124)$$

Comparison of our expression for B_z with Eq. (18) in the paper of Petropoulos et al. [7] shows that these authors failed to include the factor $(-1)^{(m-1)/2}(\mu_0/4\pi)$, or $(-1)^{(r-1)/2}(\mu_0/4\pi)$ in their notation. The omission of $(\mu_0/4\pi)$ was obviously unintended. However, omission of the factor $(-1)^{(r-1)/2}$ introduces an error by changing the sign of alternate terms, not only in Eq. (18) but also in their Eqs. (13) and (14). The error stems from the omission of $(-1)^{(r-1)/2}$ from the right-hand-side of their Eqs. (16) and (17), and cannot be attributed to differing definitions of the coefficients $A_i^{(r)}$ and $B_i^{(r)}$, since, according to Eqs. (36) – (43) in their paper, Petropoulos et al. used McLachlan's expressions for the Mathieu functions [9], as we have done.

5.2.8 Expansion of the Magnetic Field Generated by an Elliptic Cylinder Coil in Powers of x and y

For an elliptical configuration, B_z will vary with η, *i.e.* with orientation in the transverse plane. To investigate this variation, we expand B_z, first in ascending powers of x/c in the x-z plane, and then in ascending powers of y/c in the y-z plane. When $y = 0$, it follows that $\xi = 0$ and $x = c\cos\eta$ for $|x| \le c$. The expression for B_z (Eq. (5.121)) then reduces to

$$
B_z(0,\eta,z) = \frac{\mu_0 c^2}{8} \int_{-\infty}^{\infty} k^2\, dk\, e^{ikz} j_\eta(k)
$$

$$
\times \sum_{m=\text{odd}}^{\infty} (-1)^{(m-1)/2} \left\{ -\frac{\left[B_1^{(m)}\right]^3 \sinh\xi_0\, \text{Fek}_m(\xi_0)}{\text{ce}_m(0)\left[\text{ce}_m'(\pi/2)\right]^2} \left[\frac{\text{ce}_m'(\eta)}{\sin\eta}\right] \right.
$$

$$
\left. + \frac{\left[A_1^{(m)}\right]^3 \cosh\xi_0\, \text{Gek}_m(\xi_0)}{\text{se}_m'(0)\left[\text{se}_m(\pi/2)\right]^2} \left[\frac{\text{se}_m(\eta)}{\sin\eta}\right] \right\}.
\tag{5.125}
$$

By expanding $\text{ce}_m'(\eta)/\sin\eta$ and $\text{se}_m(\eta)/\sin\eta$ in ascending powers of $x/c = \cos\eta$, it is found that

$$
B_z(x,0,z) = C_0 + C_{2x}\left(\frac{x}{c}\right)^2 + C_{4x}\left(\frac{x}{c}\right)^4 + \cdots
\tag{5.126}
$$

where

$$
C_0 = \frac{\mu_0 c^2}{8} \int_{-\infty}^{\infty} k^2\, dk\, e^{ikz} j_\eta(k) \sum_{m=\text{odd}}^{\infty} \left[-\zeta_m(\xi_0,q) + \gamma_m(\xi_0,q)\right],
\tag{5.127}
$$

$$
C_{2x} = \frac{\mu_0 c^2}{8} \int_{-\infty}^{\infty} k^2\, dk\, e^{ikz} j_\eta(k)
$$

$$
\times \sum_{m=\text{odd}}^{\infty} \left\{ -\frac{1}{2}\zeta_m(\xi_0,q)\frac{\displaystyle\sum_{m'=\text{odd}}^{\infty} m'(1-m'^2)\, B_{m'}^{(m)}}{\displaystyle\sum_{m'=\text{odd}}^{\infty} m' B_{m'}^{(m)}} \right.
$$

$$
\left. + \frac{1}{2}\gamma_m(\xi_0,q)\frac{\displaystyle\sum_{m'=\text{odd}}^{\infty} (1-m'^2)\, A_{m'}^{(m)}}{\displaystyle\sum_{m'=\text{odd}}^{\infty} A_{m'}^{(m)}} \right\},
\tag{5.128}
$$

$$
C_{4x} = \frac{\mu_0 c^2}{8} \int_{-\infty}^{\infty} k^2\, dk\, e^{ikz} j_\eta(k)
$$

105

$$\times \sum_{m=odd}^{\infty} \left\{ -\frac{1}{24} \zeta_m(\xi_0, q) \frac{\sum_{m'=odd}^{\infty} m'(1-m'^2)(9-m'^2) B_{m'}^{(m)}}{\sum_{m'=odd}^{\infty} m' B_{m'}^{(m)}} \right.$$

$$\left. +\frac{1}{24} \gamma_m(\xi_0, q) \frac{\sum_{m'=odd}^{\infty} (1-m'^2)(9-m'^2) A_{m'}^{(m)}}{\sum_{m'=odd}^{\infty} A_{m'}^{(m)}} \right\}, \qquad (5.129)$$

and

$$\gamma_m(\xi_0, q) = \frac{(-1)^{(m-1)/2} \left[A_1^{(m)} \right]^3}{se_m'(0) se_m(\pi/2)} \cosh \xi_0 \, \mathrm{Gek}_m(\xi_0), \qquad (5.130)$$

$$\zeta_m(\xi_0, q) = \frac{(-1)^{(m-1)/2} \left[B_1^{(m)} \right]^3}{ce_m(0) ce_m'(\pi/2)} \sinh \xi_0 \, \mathrm{Fek}_m(\xi_0). \qquad (5.131)$$

By putting $x = 0$ so that $\eta = \pi/2$ and $y = c \sinh \xi$ in Eq. (5.121), and expanding $\mathrm{Ce}_m(\xi)/\cosh \xi$ and $\mathrm{Se}_m'(\xi)/\cosh \xi$ in ascending powers of y/c, it is found in a similar manner that

$$B_z(0, y, z) = C_0 + C_{2y} \left(\frac{y}{c} \right)^2 + C_{4y} \left(\frac{y}{c} \right)^4 + \cdots \qquad (5.132)$$

where

$$C_{2y} = \frac{\mu_0 c^2}{8} \int_{-\infty}^{\infty} k^2 \, dk \, e^{ikz} j_\eta(k)$$

$$\times \sum_{m=odd}^{\infty} \left\{ \frac{1}{2} \zeta_m(\xi_0, q) \frac{\sum_{m'=odd}^{\infty} (-1)^{(m'-1)/2} (1-m'^2) B_{m'}^{(m)}}{\sum_{m'=odd}^{\infty} (-1)^{(m'-1)/2} B_{m'}^{(m)}} \right.$$

$$\left. -\frac{1}{2} \gamma_m(\xi_0, q) \frac{\sum_{m'=odd}^{\infty} (-1)^{(m'-1)/2} m'(1-m'^2) A_{m'}^{(m)}}{\sum_{m'=odd}^{\infty} (-1)^{(m'-1)/2} m' A_{m'}^{(m)}} \right\}, \qquad (5.133)$$

$$C_{4y} = \frac{\mu_0 c^2}{8} \int_{-\infty}^{\infty} k^2 \, dk \, e^{ikz} j_\eta(k)$$

$$\times \sum_{m=\text{odd}}^{\infty} \left\{ -\frac{1}{24} \zeta_m(\xi_0, q) \frac{\sum_{m'=\text{odd}}^{\infty} (-1)^{(m'-1)/2} (1 - m'^2)(9 - m'^2) B_{m'}^{(m)}}{\sum_{m'=\text{odd}}^{\infty} (-1)^{(m'-1)/2} B_{m'}^{(m)}} \right.$$

$$\left. +\frac{1}{24} \gamma_m(\xi_0, q) \frac{\sum_{m'=\text{odd}}^{\infty} (-1)^{(m'-1)/2} m' (1 - m'^2)(9 - m'^2) A_{m'}^{(m)}}{\sum_{m'=\text{odd}}^{\infty} (-1)^{(m'-1)/2} m' A_{m'}^{(m)}} \right\} . \quad (5.134)$$

The above expressions are valid, not only for the field generated by an elliptic cylinder z gradient coil, in which case $j_\eta(k)$ is antisymmetric with respect to k, but also for the field generated by any purely azimuthal current flowing on the surface of an elliptic cylinder. It is shown in the next subsection how these expressions are modified when the current flows axially as well as azimuthally.

5.2.9 Magnetic Field of an Elliptic Cylinder z Gradient Coil When the Current Flows Axially as well as Azimuthally

To conform to the symmetry of the elliptic cylinder and to permit first order compensation of the variation of B_z in the transverse plane, we take the azimuthal component of the current density to be modulated in both the azimuthal and axial dimensions and to be of the form

$$j_\eta(\eta, z) = j_\eta(z)(1 - 2a_2 \cos 2\eta) \quad (5.135)$$

so that $j_\eta(z)$ is the current density at $\eta = \pi/4$. (The factor of 2 in the coefficient of $\cos 2\eta$ is introduced to simplify subsequent equations.)

From the definitions of $u_m^c(k)$, $v_m^c(k)$, $u_m^s(k)$ and $v_m^s(k)$ given by Eqs. (5.88) – (5.91), it is found that when $j_\eta(\eta, z)$ is given by Eq. (5.135), the only non-zero quantities are

$$u_m^c(k) = (-1)^{(m-1)/2} \frac{(1 - a_2) B_1^{(m)} + a_2 B_3^{(m)}}{2} j_\eta(k) \quad (5.136)$$

107

$$v_m^s(k) = (-1)^{(m-1)/2} \frac{(1+a_2)A_1^{(m)} + a_2 A_3^{(m)}}{2} j_\eta(k),\qquad (5.137)$$

when m is odd.

Determination of $w_m^c(k)$ and $w_m^s(k)$, which are governed by $j_z(\eta, z)$, requires knowledge of $j_\eta^{c,n}(k)$ and $j_\eta^{s,n}(k)$. By evaluating Eqs. (5.106) and (5.107) for $j_\eta(\eta, z)$ given by Eq. (5.135), it is found that $j_\eta^{s,n}(k)$ is always zero, and $j_\eta^{c,n}(k)$ is given by

$$j_\eta^{c,n}(k) = \begin{cases} (-1)^{n/2} j_\eta(k)\left[A_0^{(n)} + a_2 A_2^{(n)}\right], & \text{if } n = 0,\ 2,\ 4,\ldots; \\ \\ 0, & \text{if } n = 1,\ 3,\ 5,\ldots. \end{cases} \qquad (5.138)$$

It then follows from Eqs. (5.116) and (5.117) that $w_m^c(k)$ is always zero, and $w_m^s(k)$ is nonzero only if m is even and ≥ 2, in which case

$$w_m^s(k) = \frac{j_\eta(k)}{ikc}\left[\sum_{n=\text{even},\geq 0}^{\infty} (-1)^{n/2} \nu_{m,n} A_0^{(n)} + a_2 \sum_{n=\text{even},\geq 0}^{\infty} (-1)^{n/2} \nu_{m,n} A_2^{(n)}\right]. \qquad (5.139)$$

The two summations on the right-hand side can be expressed as

$$\sum_{n=\text{even},\geq 0}^{\infty} (-1)^{n/2} \nu_{m,n} A_0^{(n)} = \frac{1}{\pi}\int_{-\pi}^{\pi} d\eta\ \text{se}_m'(\eta) \sum_{n=\text{even},\geq 0}^{\infty} (-1)^{n/2} A_0^{(n)} \text{ce}_n(\eta) \qquad (5.140)$$

$$\sum_{n=\text{even},\geq 0}^{\infty} (-1)^{n/2} \nu_{m,n} A_2^{(n)} = \frac{1}{\pi}\int_{-\pi}^{\pi} d\eta\ \text{se}_m'(\eta) \sum_{n=\text{even},\geq 0}^{\infty} (-1)^{n/2} A_2^{(n)} \text{ce}_n(\eta), \qquad (5.141)$$

using the definition of $\nu_{m,n}$ given by Eq. (5.111). Since

$$\sum_{n=\text{even},\geq 0}^{\infty} (-1)^{n/2} A_0^{(n)} \text{ce}_n(\eta) = \frac{1}{2} \qquad (5.142)$$

$$\sum_{n=\text{even},\geq 0}^{\infty} (-1)^{n/2} A_2^{(n)} \text{ce}_n(\eta) = -\cos 2\eta, \qquad (5.143)$$

it follows that

$$\sum_{n=\text{even},\geq 0}^{\infty} (-1)^{n/2} \nu_{m,n} A_0^{(n)} = \frac{1}{2\pi}\int_{-\pi}^{\pi} d\eta\ \text{se}_m'(\eta)$$
$$= 0 \qquad (5.144)$$

$$\sum_{n=\text{even},\geq 0}^{\infty} (-1)^{n/2} \nu_{m,n} A_2^{(n)} = -\frac{1}{\pi}\int_{-\pi}^{\pi} d\eta\ \cos 2\eta\ \text{se}_m'(\eta)$$
$$= -2(-1)^{(m-2)/2} B_2^{(m)}. \qquad (5.145)$$

Thus, $w_m^s(k)$ is given by

$$w_m^s(k) = (-1)^{(m-2)/2} \frac{2ia_2 B_2^{(m)}}{kc} j_\eta(k) \tag{5.146}$$

where m is even and ≥ 2.

Comparison of the above expressions for $u_m^c(k)$ and $v_m^s(k)$, with those obtained for a purely azimuthal current, namely Eqs. (5.118) and (5.119), shows that $A_1^{(m)}$ and $B_1^{(m)}$ are replaced by $[(1 + a_2)A_1^{(m)} + a_2 A_3^{(m)}]$ and $[(1 - a_2)B_1^{(m)} + a_2 B_3^{(m)}]$, respectively. The expression for B_z is therefore of the same form as for a purely azimuthal current, namely Eq. (5.121), but with

$$
\begin{aligned}
P_z(\xi, \eta, \xi_0, q) = & \sum_{m=odd}^{\infty} (-1)^{(m-1)/2} \left\{ \frac{\beta_m \left[(1 - a_2)B_1^{(m)} + a_2 B_3^{(m)}\right]}{(M_m^c)^2} \sinh \xi_0 \, \text{Fek}_m(\xi_0) \right. \\
& \left. + \frac{\alpha_m \left[(1 + a_2)A_1^{(m)} + a_2 A_3^{(m)}\right]}{(M_m^s)^2} \cosh \xi_0 \, \text{Gek}_m(\xi_0) \right\}.
\end{aligned}
\tag{5.147}
$$

It also follows that C_0, C_{2x}, C_{2y}, C_{4x} and C_{4y} are still given by Eqs. (5.127) – (5.129), (5.133) and (5.134), but with $\gamma_m(\xi_0, q)$ and $\zeta_m(\xi_0, q)$ now given by

$$\gamma_m(\xi_0, q) = \frac{(-1)^{(m-1)/2} \left[A_1^{(m)}\right]^2 \left[(1 + a_2)A_1^{(m)} + a_2 A_3^{(m)}\right]}{\text{se}_m'(0) \, \text{se}_m(\pi/2)} \cosh \xi_0 \, \text{Gek}_m(\xi_0), \tag{5.148}$$

$$\zeta_m(\xi_0, q) = \frac{(-1)^{(m-1)/2} \left[B_1^{(m)}\right]^2 \left[(1 - a_2)B_1^{(m)} + a_2 B_3^{(m)}\right]}{\text{ce}_m(0) \, \text{ce}_m'(\pi/2)} \sinh \xi_0 \, \text{Fek}_m(\xi_0). \tag{5.149}$$

5.2.10 Minimization of the Inductance of an Elliptic Cylinder z Gradient Coil

When the current is purely azimuthal, the expression for the stored energy in an elliptic cylinder coil, namely Eq. (5.102), reduces to

$$W = \frac{\pi \mu_0 c^2}{4} \int_{-\infty}^{\infty} dk \, |j_\eta(k)|^2 Q_z(\xi_0, q), \tag{5.150}$$

where $Q_z(\xi_0, q)$ is given by

$$Q_z(\xi_0, q) = \sum_{m=odd}^{\infty} \left\{ \left[\frac{B_1^{(m)}}{M_m^c} \right]^2 \sinh^2\xi_0 \, \mathrm{Ce}_m(\xi_0) \, \mathrm{Fek}_m(\xi_0) \right.$$
$$\left. + \left[\frac{A_1^{(m)}}{M_m^s} \right]^2 \cosh^2\xi_0 \, \mathrm{Se}_m(\xi_0) \, \mathrm{Gek}_m(\xi_0) \right\}. \qquad (5.151)$$

It should be pointed out that, although our expression for the stored energy is of the same form as Eq. (20) in the paper of Petropoulos *et al.* [7] (apart from a typographical error; $(\eta^2 - 1)$ should read $(\eta_0^2 - 1)$), they differ by a factor of $\pi^2(\mu_0/4\pi)$. In the limit when the ellipse becomes a circle ($\xi_0 \to \infty$ and $c \to 0$ in our notation), it is found that our Eqs. (5.150) and (5.151) agree with expressions for the stored energy in a circular cylinder z gradient coil [4, 5, 12], whereas Eq. (20) in Ref. [7] does not. The omission of the factor $(-1)^{(r-1)/2}$ in Eqs. (16) and (17) in Ref. [7] is of no consequence in Eq. (20), since it is squared under the summation sign.

When the current is *no longer purely azimuthal*, and the azimuthal component of the current density is given by Eq. (5.135), the stored energy is still given by Eq. (5.150) but with

$$Q_z(\xi_0, q) = \sum_{m=odd}^{\infty} \left\{ \left[\frac{(1 - a_2)B_1^{(m)} + a_2 B_3^{(m)}}{M_m^c} \right]^2 \sinh^2\xi_0 \, \mathrm{Ce}_m(\xi_0) \, \mathrm{Fek}_m(\xi_0) \right.$$
$$\left. + \left[\frac{(1 + a_2)A_1^{(m)} + a_2 A_3^{(m)}}{M_m^s} \right]^2 \cosh^2\xi_0 \, \mathrm{Se}_m(\xi_0) \, \mathrm{Gek}_m(\xi_0) \right\}$$
$$+ \sum_{m=even,\geq 2}^{\infty} \left[\frac{2a_2 B_2^{(m)}}{\sqrt{q}\, M_m^s} \right]^2 \mathrm{Se}_m(\xi_0) \, \mathrm{Gek}_m(\xi_0). \qquad (5.152)$$

In order to minimize the inductance and hence the stored energy when the coil produces target fields B_n at locations $r_n = (\xi_n, \eta_n, z_n)$, where $n = 1, 2, \ldots, N$, we rewrite Eq. (5.121) in the symmetrical form

$$B_z(\xi, \eta, z) = \frac{\mu_0}{4} \int_{-\infty}^{\infty} dk \, \left[j_\eta(k)e^{ikz} + j_\eta^*(k)e^{-ikz} \right] P_z(\xi, \eta, \xi_0, q), \qquad (5.153)$$

110

and follow Turner's method for circular cylinder coils [4] by constructing a functional

$$U = W - \sum_{n=1}^{N} \lambda_n \left[B_n - B_z(\mathbf{r}_n) \right] \tag{5.154}$$

where λ_n are Lagrange multipliers. Setting the variation of U to zero results in the following equations

$$\frac{\partial F}{\partial j_\eta(k)} = 0 \quad \text{and} \quad \frac{\partial F}{\partial j_\eta^*(k)} = 0 \tag{5.155}$$

where

$$F\left[k, j_\eta(k), j_\eta^*(k) \right] = \frac{\pi \mu_0 c^2}{4} |j_\eta(k)|^2 Q_z(\xi_0, q)$$
$$- \sum_{n=1}^{N} \lambda_n \frac{\mu_0}{4} \left[j_\eta(k) e^{ikz_n} + j_\eta^*(k) e^{-ikz_n} \right] P_z(\xi_n, \eta_n, \xi_0, q). \tag{5.156}$$

In Eq. (5.156), $P_z(\xi, \eta, \xi_0, q)$ and $Q_z(\xi_0, q)$ are given by Eqs. (5.122) and (5.151), respectively, for a purely azimuthal current, and by Eqs. (5.147) and (5.152), respectively, for a current density whose azimuthal component is $j_\eta(z)(1 - 2a_2 \cos 2\eta)$. By solving either $\partial F/\partial j_\eta(k) = 0$ or $\partial F/\partial j_\eta^*(k) = 0$, and imposing the condition that $j_{\eta'}(z')$ should be antisymmetric with respect to z', so that $j_\eta(k)$ is antisymmetric with respect to k, it is found that

$$j_\eta(k) = \frac{1}{i\pi c^2 Q_z(\xi_0, q)} \sum_{n=1}^{N} \lambda_n \sin k z_n \, P_z(\xi_n, \eta_n, \xi_0, q). \tag{5.157}$$

The Lagrange multipliers can then be determined by solving the simultaneous equations

$$B_m = \sum_{n=1}^{N} \lambda_n \frac{\mu_0}{\pi c^2} \int_0^\infty dk \, \sin k z_m \, \sin k z_n \frac{P_z(\xi_m, \eta_m, \xi_0, q) P_z(\xi_n, \eta_n, \xi_0, q)}{Q_z(\xi_0, q)}, \tag{5.158}$$

where $m = 1, 2, \ldots, N$. By substituting Eq. (5.157) in Eq. (5.150), the stored energy is given by

$$W = \frac{\mu_0}{2\pi c^2} \int_0^\infty dk \frac{1}{Q_z(\xi_0, q)} \left[\sum_{n=1}^{N} \lambda_n \sin k z_n \, P_z(\xi_n, \eta_n, \xi_0, q) \right]^2, \tag{5.159}$$

which can be rearranged to read

$$W = \frac{1}{2} \sum_{n=1}^{N} \lambda_n \left[\sum_{n'=1}^{N} \lambda_{n'} \frac{\mu_0}{\pi c^2} \int_0^\infty dk \, \sin k z_n \, \sin k z_{n'} \frac{P_z(\xi_n, \eta_n, \xi_0, q) P_z(\xi_{n'}, \eta_{n'}, \xi_0, q)}{Q_z(\xi_0, q)} \right].$$
$$\tag{5.160}$$

By comparing Eq. (5.160) with Eq. (5.158), it can be seen that the terms within the square brackets on the right-hand side of Eq. (5.160) are simply equal to B_n, the specified values of the magnetic field at points $r_n = (\xi_n, \eta_n, z_n)$. Therefore, the minimum stored energy of an elliptic cylinder z gradient coil can be expressed in a very simple form, namely

$$W = \frac{1}{2} \sum_{n=1}^{N} \lambda_n B_n, \qquad (5.161)$$

which is the same as that for a circular cylinder coil, as shown in my M.Sc. thesis [12].

5.3 Elliptic Cylinder Gradient Coil Designs

The theory developed in the previous section was first used to design an elliptic cylinder z gradient coil which carries a purely azimuthal current. A representative axial ratio, b/a, of 0.75 was chosen, where a and b are, respectively, the lengths of the semi-major and semi-minor axes of the ellipse. Such a ratio corresponds to an eccentricity of 0.661 and is roughly the value that might be utilized for whole body MRI. All dimensions are expressed in terms of a, as a scaling factor, so that the design can be used for a coil of any size whose axial ratio is 0.75. Design specifications are presented for coils that generate a gradient of 10 mT/m, irrespective of the scaling factor. Eight target field points, located at $x/a = y/a = 0$ and $z/a = 0.05n$ with $n = 1, 2, \ldots, 8$, were selected, the corresponding values of B_z being $(5 \times 10^{-4} na)$ T, where a is expressed in metres.

As in the case of circular cylinder coils [5], very high accuracy is required in evaluating the integrals in Eq. (5.158), if reliable values of the Lagrange multipliers are to be obtained. This is especially true if, as in our case, a large number of target field points is used. Since we were not aware of any software to evaluate modified Mathieu functions, and the software to evaluate coefficients of Mathieu functions is of insufficient accuracy, subroutines were developed in house. Our values of periodic Mathieu functions and their coefficients are in agreement with those

listed in Ref. [10], which are given to eight or more digits. We note that Petropoulos *et al.*'s values of the leading coefficients of the Mathieu functions sometimes differ from NBS values in the sixth significant digit [7]. We believe that the accuracy of Petropoulos *et al.*'s values is inadequate for evaluating the Lagrange multipliers.

The current density distribution, evaluated using the method described in the previous section, is shown in Fig. 5.5a for $z/a > 0$. Rapid oscillations in the current density were removed by smoothing or apodization [4], multiplication by $\exp(-0.0052k^2a^2)$ prior to the inverse Fourier transformation. The exponent in the apodization factor was chosen so that the current did not change sign. The integrated current, $I_{\text{int}}(z)$, given by

$$I_{\text{int}}(z) = \int_0^z j_\eta(z')\,dz', \tag{5.162}$$

is shown in Fig. 5.5b. The location of N_w wires that would approximate the current distribution was found by dividing $I_{\text{int}}(\infty)$ into N_w equal increments, and then placing the wires at positions $z = \pm z_i$ such that

$$I_{\text{int}}(z_i) = \left(i + \frac{1}{2}\right)\frac{I_{\text{int}}(\infty)}{N_w}, \tag{5.163}$$

where $i = 0, 1, \ldots, (n-1)$. Figure 5.6a shows the location of 18 wires, all carrying identical currents, that approximate, on the surface of the elliptic cylinder, the smoothed current distribution shown in Fig. 5.5a.

The energy stored in the coil, when it generates a gradient of 10 mT/m, was found, using Eqs. (5.150) and (5.151), to be $(479a^5)$ J. For comparison, the energy stored in a circular cylinder coil of radius a (metres) which also generates a gradient of 10 mT/m was found to be $(696a^5)$ J. In this case, the apodization factor was $\exp(-0.015k^2a^2)$, again chosen so that the current did not change sign. The reduction in the stored energy, and hence in the inductance, achieved by replacing a circular coil by an elliptical one with an equal value of a, is therefore 31%. This
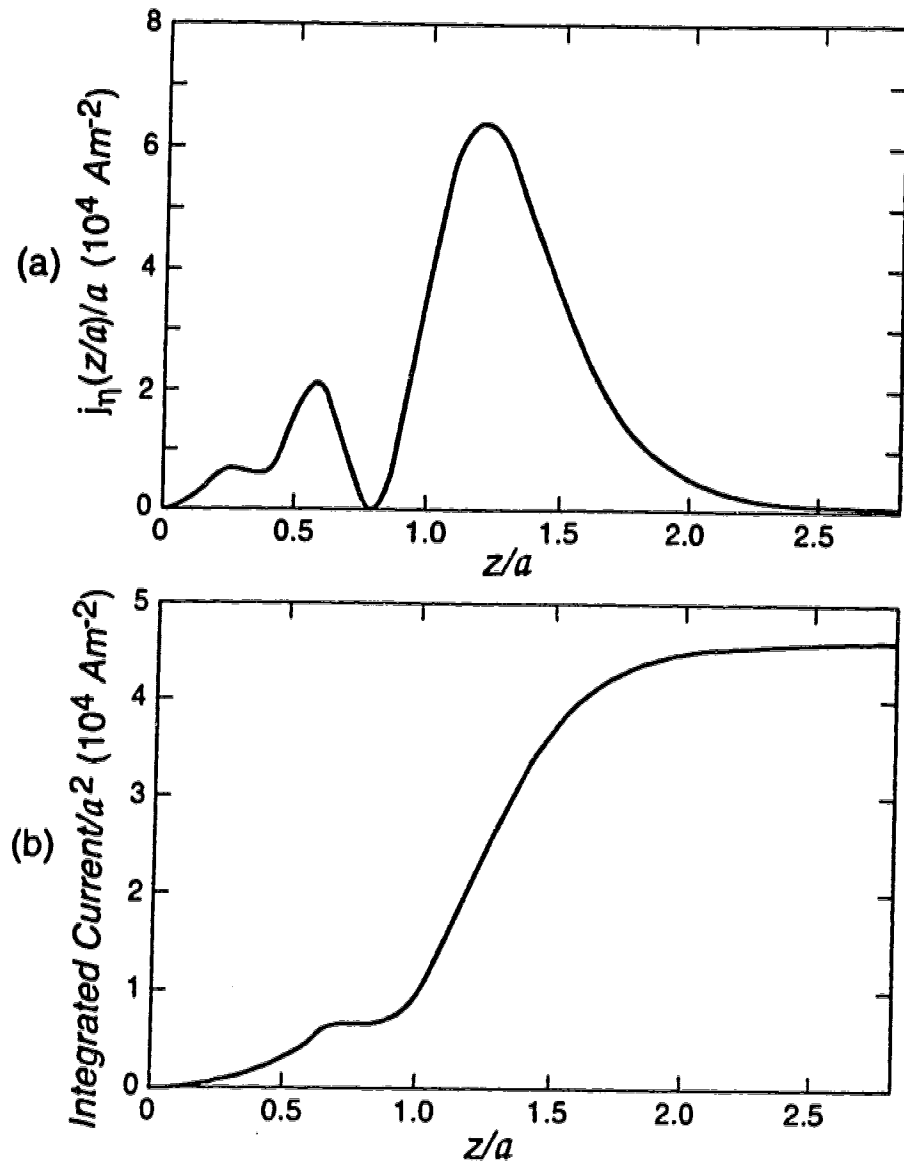
Figure 5.5: (a) The smoothed, purely azimuthal current density, $j_\eta(z/a)/a$, which, flowing in an elliptic cylinder z gradient coil of minimum inductance and semi-major axis a, will generate a gradient of 10 mT/m. (The current density is of opposite sign for $z < 0$.) (b) The corresponding integrated current.

114
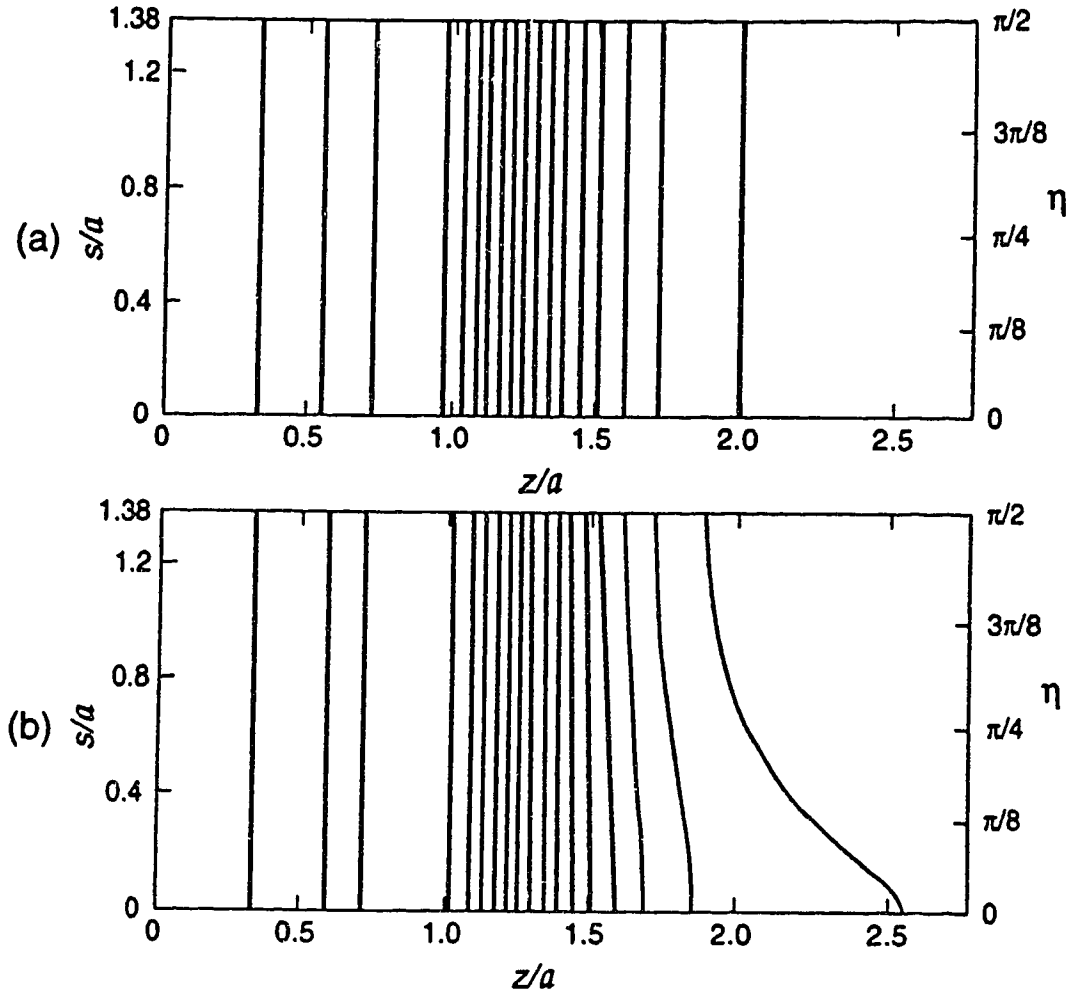
Figure 5.6: (a) Configuration of 18 wires in the octant $z > 0$ and $0 \le \eta \le \pi/2$ of the elliptic cylinder, that approximates the current distribution shown in Fig. 5.5a. (b) The corresponding configuration of 18 wires that approximates the current distribution when the azimuthal component is of the form $j_\eta(z/a)(1 - 0.025\cos 2\eta)$. The representation is on the curved surface of the elliptic cylinder, and is therefore linear in s, the length measured in the azimuthal direction from the line $x = a$, $y = 0$, but nonlinear in η.

115

is comparable with the reduction found by Petropoulos *et al.* [7], and Du and Parker [13] for an elliptic cylinder coil carrying a purely azimuthal current.

Along the z axis, B_z was found to deviate from linearity by less than 0.1% out to $z/a = 0.61$ ($z/b = 0.81$). However, there is quite a substantial nonuniformity in the transverse directions. As can be seen in Fig. 5.7, B_z/a increases quite rapidly with x/a at $y/a = 0$ in the transverse planes $z/a = 0.05$ and 0.25, but decreases equally rapidly with y/a at $x/a = 0$, at least in the region $y/a < 0.4$. This is consistent with the fact that C_{2x}/a and C_{2y}/a, evaluated using Eqs. (5.128) and (5.133) at either $z/a = 0.05$ or 0.25, are almost equal in magnitude to each other, but opposite in sign, as shown in Table 5.1. This is not a coincidence since,

Table 5.1: C_{2x}/a, C_{2y}/a, C_{4x}/a and C_{4y}/a, evaluated at $z/a = 0.05$, 0.25 and 0.6, for the first design where the current is purely azimuthal, the gradient is 10 mT/m, and a is the length of the semi-major axis of the ellipse

z/a	C_{2x}/a (T/m)	C_{2y}/a (T/m)	C_{4x}/a (T/m)	C_{4y}/a (T/m)
0.05	5.21×10^{-3}	-5.21×10^{-3}	-3.05×10^{-3}	3.37×10^{-3}
0.25	3.13×10^{-2}	-3.09×10^{-2}	-2.49×10^{-2}	2.17×10^{-2}
0.6	2.42×10^{-1}	3.40×10^{-3}	-2.09×10^{-1}	-5.37×10^{-1}

for a steady field, $\nabla^2 B = 0$ in a current-free region, so that

$$\frac{\partial^2 B_z}{\partial x^2} + \frac{\partial^2 B_z}{\partial y^2} + \frac{\partial^2 B_z}{\partial z^2} = 0. \tag{5.164}$$

If the z gradient, $\partial B_z/\partial z$, is independent of z, $\partial^2 B_z/\partial z^2$ is zero, from which it follows that

$$\frac{\partial^2 B_z}{\partial x^2} = -\frac{\partial^2 B_z}{\partial y^2} \quad \text{or} \quad C_{2x} = -C_{2y}. \tag{5.165}$$

Figure 5.7: The magnetic field B_z, divided by the length of the semi-major axis a, associated with a z gradient of 10 mT/m, shown as a function of x/a with $y/a = 0$, and as a function of y/a with $x/a = 0$ in (a) the $z/a = 0.05$ transverse plane and in (b) the $z/a = 0.25$ transverse plane. The upper and lower curves refer to the first design where the current is purely azimuthal. The other two curves refer to the second design where the azimuthal component of the current is of the form $j_\eta(z/a)(1 - 0.025\cos 2\eta)$.

117

Since the z gradient in our elliptic cylinder coil design is almost independent of z in the region $0 \leq z/a \leq 0.4$, C_{2x} and C_{2y} at $z/a = 0.05$ and 0.25 are expected to be almost equal in magnitude but opposite in sign, as obtained.

Also shown in Table 5.1 are C_{4x}/a and C_{4y}/a, evaluated using Eqs. (5.129) and (5.134). They too are of opposite sign but unequal in amplitude, thereby accounting for the shape and asymmetric behaviour of the curves in Fig. 5.7 when x/a or y/a is greater than 0.4. The behaviour of B_z/a in the transverse plane $z/a = 0.6$, well outside the target field region, is shown as the upper and lower curves in Fig. 5.8, and is seen to be quite different from that in Fig. 5.7. This is reflected in the values of C_{2x}/a, C_{2y}/a, C_{4x}/a, and C_{4y}/a at $z/a = 0.6$, which are also listed in Table 5.1.

To achieve an accuracy ~ 1 part in 10^3 in calculating the coefficients C_{2x}/a, etc., it was necessary to carry out the summation over m out to $m = 7$ or $m = 9$. It should be noted that the coefficients were evaluated using the apodized current distribution. Without apodization, the numerical values of C_{2x}/a and C_{2y}/a (C_{4x}/a and C_{4y}/a) are roughly 10% (30%) smaller than those listed in Table 5.1.

The fact that C_{2x}/a and C_{2y}/a are of almost equal magnitude but opposite sign in the target field region, indicates that it should be possible to largely eliminate the parabolic component of B_z/a in the x and y directions, by introducing a small $\cos 2\eta$ dependence into the azimuthal current, even though this introduces a concomitant axial component. We therefore consider a second design where the azimuthal component of the current density is given by

$$j_\eta(\eta, z/a) = j_\eta(z/a)(1 - 0.025 \cos 2\eta), \qquad (5.166)$$

so that a_2 in Eq. (5.135) is 0.0125. When the apodization factor is taken to be $\exp\left(-0.0063k^2a^2\right)$, so that the current does not change sign, $j_\eta(z/a)$, the azimuthal current density at $\eta = \pi/4$, is very similar to that shown in Fig. 5.5a for a purely
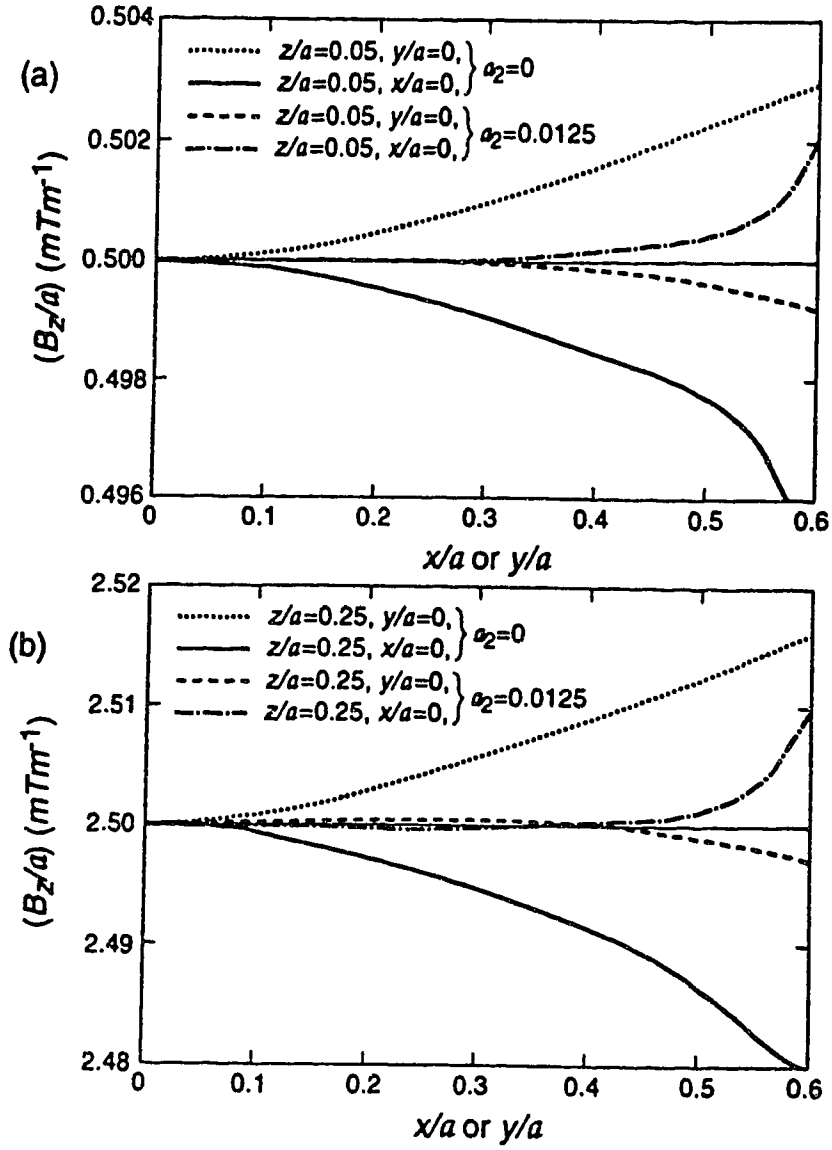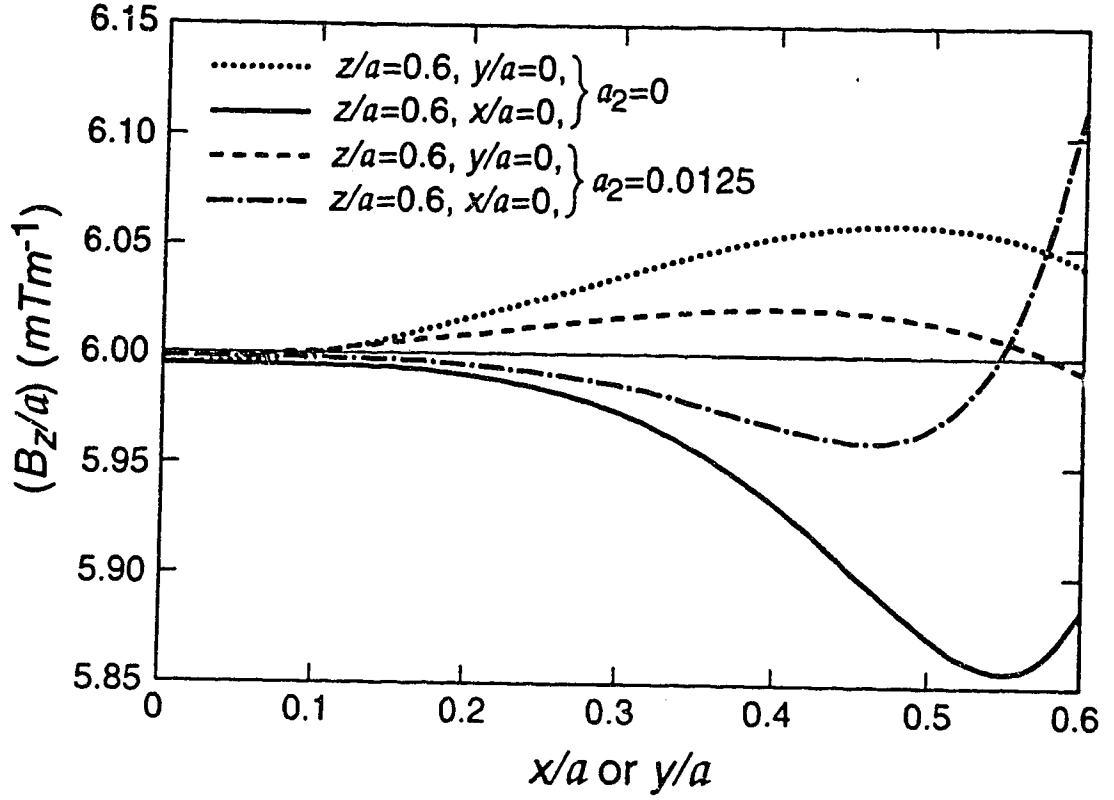
Figure 5.8: The magnetic field B_z, divided by the length of the semi-major axis a, associated with a z gradient of 10 mT/m, shown as a function of x/a with $y/a = 0$, and as a function of y/a with $x/a = 0$ in the $z/a = 0.6$ transverse plane. The upper and lower curves refer to the first design where the current is purely azimuthal. The other two curves refer to the second design where the azimuthal component of the current is of the form $j_\eta(z/a)(1 - 0.025\cos 2\eta)$.

119

azimuthal current. The behaviour of B_z/a in the planes $z/a = 0.05$ and 0.25, evaluated using Eqs. (5.121) and (5.147), is shown in Fig. 5.7. It can be seen that the variation of B_z/a in the transverse directions is less than 0.1% out to x/a or $y/a = 0.53$, as compared to being less than 0.1% out to x/a or $y/a = 0.2$ when the current is purely azimuthal. Moreover, the linearity of the gradient along the z axis is slightly better than before.

While it is possible to choose a_2 to eliminate the parabolic component of B_z accurately in both the x and y directions when $z/a \ll 1$, this parameter was chosen empirically to be 0.0125 so as to yield an extended region of essentially uniform B_z in those directions. Values of C_{2x}/a, C_{4x}/a, C_{2y}/a and C_{4y}/a, calculated using Eqs. (5.128), (5.129), (5.133) and (5.134) but with $\gamma_m(\xi_0, q)$ and $\zeta_m(\xi_0, q)$ given by Eqs. (5.148) and (5.149), are listed in Table 5.2. Comparison of the values of C_{2x}/a

Table 5.2: C_{2x}/a, C_{2y}/a, C_{4x}/a and C_{4y}/a, evaluated at $z/a = 0.05$, 0.25 and 0.6, for the second design where the azimuthal component of current is given by Eq. (5.166), the gradient is 10 mT/m, and a is the length of the semi-major axis of the ellipse.

z/a	C_{2x}/a (T/m)	C_{2y}/a (T/m)	C_{4x}/a (T/m)	C_{4y}/a (T/m)
0.05	2.60×10^{-4}	-2.60×10^{-4}	-2.21×10^{-3}	2.43×10^{-3}
0.25	4.99×10^{-3}	-4.88×10^{-3}	-1.74×10^{-2}	1.77×10^{-2}
0.6	1.29×10^{-1}	6.61×10^{-3}	-1.75×10^{-1}	-3.67×10^{-1}

and C_{2y}/a in Tables 5.1 and 5.2 shows that a large measure of cancellation of the parabolic component of the field has been achieved using the current distribution given by Eq. (5.166). The values of C_{4x}/a and C_{4y}/a in Tables 5.1 and 5.2, on the

other hand, are comparable. This is, however, to be expected since the η dependence of the azimuthal component of the current density given by Eq. (5.166) was chosen to mainly cancel the parabolic component.

Figure 5.6b shows the location of 18 wires, all carrying identical currents, that approximate the current density distribution of Eq. (5.166) on the curved surface of the elliptic cylinder. Here, s is the length measured on the surface of the elliptic cylinder in the azimuthal direction from the line $x = a$, $y = 0$. The ordinate scale is linear in s/a but nonlinear in η, since $s/a = E[(\pi/2)\backslash\alpha] - E[(\pi/2) - \eta\backslash\alpha]$, where $E[(\pi/2)\backslash\alpha]$ and $E[(\pi/2) - \eta\backslash\alpha]$ are, respectively, complete and incomplete elliptic integrals of the second kind [14] and $\sin\alpha = c/a$.

The energy stored in a coil of this second design, when it generates a gradient of 10 mT/m, is $(514a^5)$ J, 7% larger than that associated with the first design, because of the energy associated with the axial component of current.

5.4   Discussion

We have shown, as can be seen in Fig. 5.7, that the nonuniformity of B_z in the transverse directions, which is characteristic of elliptic cylinder coil designs where the current is purely azimuthal, can be largely eliminated by introducing a $\cos 2\eta$ dependence of appropriate amplitude into the azimuthal component of the current density. This results in a z gradient coil with much improved linearity. Higher order compensation can be achieved by modifying the η dependence to cancel the $(x/a)^4$, $(y/a)^4$, etc. dependence of B_z when $z/a \ll 1$, if the region of interest extends close to the coil or if the coil is highly elliptical.

Our first design where the current is purely azimuthal displays considerably better gradient linearity along the z axis, and field uniformity in transverse planes, than do the coil designs of Petropoulos *et al.* [7]. For example, in our first design

121

where $b/a = 0.75$, the nonuniformity of B_z in the transverse directions is less than 0.5% out to x/a or $y/a = 0.5$. In Ref. [7], the nonuniformity at $y/a = 0.5$ is about 5% for a coil with $b/a = 0.82$ and 9% for a coil with $b/a = 0.73$, as can be seen in their Figs. 4 and 7. While the much poorer gradient linearity in Ref. [7] may be partly due to the choice of target field points very close to the $z = 0$ plane, we believe that the differences are mainly due to the omission of the factor $(-1)^{(r-1)/2}$ from Eqs. (27) and (30) in Ref. [7] and the fact that there is no summation over a second index, r' say, in Eq. (27). (The summation over j in Eq. (30) should be over r', though this is presumably a typographical error.)

A coil with $b/a = 0.75$ and carrying a purely azimuthal current, but with other parameters the same as those used in Ref. [7], namely $a = 0.275$ m and a gradient of 15 mT/m, was found to have a stored energy of 1.70 J. This is substantially larger than the stored energies found in Ref. [7], namely 0.76 J for $b/a = 0.73$ and 0.97 J for $b/a = 0.82$. This difference is mainly due to our selection of target field points out to $z/a = 0.4$, which yields a far better field profile over an extended region than that achieved by Petropoulos *et al.*, but at the expense of a larger stored energy. A calculation of the stored energy in a coil with their dimensions, $a = 0.275$ m and $b = 0.2$ m, their gradient strength, 15 mT/m, and using their target field points and no apodization, gave a stored energy of 0.74 J, in comparison with their value of 0.76 J. We note that their Eq. (28), the expression for the stored energy, is in agreement with ours (apart from the fact that their integral should be from 0 to ∞ instead of from $-\infty$ to ∞, presumably a typographical error). The omission of the factor $(-1)^{(r-1)/2}$ is of no direct consequence in their Eq. (28), and its predecessor Eq. (20) as explained in Section 5.2.10. However, its omission from their Eq. (30) will affect values of the Lagrange multipliers, which may be responsible for the small discrepancy between their value of stored energy and ours.

References

[1] P. Mansfield and I.L. Pykett, J. Magn. Reson. **29**, 355 (1978)

[2] M.J. Stehling, A.M. Howseman, R.J. Ordidge, B. Chapman, R. Turner, R. Coxon, P. Glover, P. Mansfield, and R.E. Coupland, *Radiology* **170**, 257 (1989).

[3] R. Turner, *J. Phys. D: Appl. Phys.* **19**, L147 (1986).

[4] R. Turner, *J. Phys. E: Sci. Instrum.* **21**, 948 (1988).

[5] R. Turner, *Magn. Reson. Imaging* **11**, 903 (1993).

[6] D.G. Hughes, R. Teshima, Q. Liu and P.S. Allen, *J. Magn. Reson. B* **110**, 158 (1996).

[7] L.S. Petropoulos, M.A. Martens, R.W. Brown, M.R. Thompson, M.A. Morich, and J.L. Patrick, *Meas. Sci. Technol.* **4**, 349 (1993).

[8] F. Romeo and D.I. Hoult, *Magn. Reson. Med.* **1**, 44 (1984).

[9] N.W. McLachlan. "Theory and Application of Mathieu Functions," Oxford University Press, London, 1947.

[10] G. Blanch, *in* "Handbook of Mathematical Functions" (M. Abramowitz and I.A. Stegun, eds.), p. 721, Dover, New York, 1972.

[11] P.M. Morse and H. Feshbach, "Methods of Theoretical Physics", McGraw-Hill, New York, 1953.

[12] Q. Liu, M.Sc. Thesis, University of Alberta, 1991.

[13] Y.P. Du and D.L. Parker, Proceedings, 3rd Annual Meeting, Society of Magnetic Resonance, 1995, Nice, p.946.

[14] L.M. Milne-Thomson, *in* "Handbook of Mathematical Functions" (M. Abramowitz and I.A. Stegun, eds.), p. 587, Dover, New York, 1972.

Chapter Six

SUMMARY AND CONCLUSIONS

The work presented in this thesis falls into two distinct parts. The first part involves upgrading a 40 cm bore, 2.35 T Bruker MR magnet system, used for animal studies in the University of Alberta's *In vivo* NMR Facility. The second part deals with the design of elliptic cylinder gradient coils.

6.1 Upgrading of the Bruker Magnet System

The work of an earlier graduate student, Mr. Scott Robertson [1], had clearly shown that the Bruker magnet and gradient system had serious deficiencies which prevented "state of the art" protocols being implemented. Moreover, the required upgrades could not be made using equipment commercially available at the time. Thus, it was decided to do the upgrading "in house".

Particularly troublesome were magnetic fields associated with slowly decaying eddy currents induced in the structure of the magnet by switched gradients. The temporal and spatial dependence of the eddy current fields were therefore studied by measuring the offset frequency of the proton FID obtained from a 13 mm diameter spherical sample of water, as described in Chapter Two. By analysing the data, it was found that there were three exponentially decaying eddy current fields associated with each of the x, y and z gradients. Decay times of these eddy current fields ranged from 13.5 ± 1.8 ms to 481 ± 1 ms. The spatial dependence of the eddy current fields showed that, while all the eddy current fields were primarily uniform gradients, those associated with the x and z gradients were accompanied by time dependent homogeneous field shifts. The data analysis also showed that

the amplitudes of the eddy current field gradients were extremely large, more than 50% of the main gradient in the case of the x and y gradients, and about 40% of the main gradient in the case of the z gradient! Moreover, the amplitudes of the field shifts were as large as 120 Hz, large enough to cause serious problem in observing proton spectra, for example. The large eddy current field gradients and field shifts, as well as very slow switching times of ~ 1 ms for the main gradients led to the conclusion that, in order to carry out *in vivo* NMR studies, especially fast imaging experiments, on this Bruker system, an actively shielded gradient set [2] was required. Accordingly, three shielded, distributed current, cylindrical gradient coils of minimum inductance of Turner design were constructed in house [3].

When these gradient coils were installed in the magnet, it was found that very accurate positioning of the primary and shielding coils in the axial direction was required to achieve proper shielding. In a theoretical study of shielded z gradient coils, presented in Chapter Three, it was found that a small relative axial displacement of the primary and shielding coils from their correct juxtaposition, gave rise primarily to a homogeneous field shift. Analytical expressions were derived which enabled the artifacts caused by such a field shift to be evaluated for various MRI and MRS protocols. This, in turn, enabled the maximum allowable relative displacement of the primary and shielding coils, which would give rise to minimal artifacts, to be estimated. It was found, using typical timing parameters, that the maximum tolerable relative displacement in the case of spin-echo, FLASH [4] and MBEST [5] imaging was roughly 1 mm, if the decay times of the eddy currents are less than or of the order of the duration of the gradient pulses. If the eddy currents have much longer decay times, there is substantial cancellation of the eddy current fields generated by the switch-on and switch-off of the gradient pulses. In that case, the maximum allowable relative displacement is much larger than 1 mm.

By applying the analytical expressions to the STEAM pulse sequence [6] for

126

proton spectroscopy, it was found that the demands of *in vivo* proton spectroscopy require a maximum relative displacement of roughly 0.1 mm, much smaller than in MRI.

While we have restricted ourselves to an axial relative displacement of the primary and shielding coils in a shielded z gradient set, the results obtained should give a good indication of the tolerance required in the construction of the individual coils in transverse gradient sets, as well as in their alignment in the transverse directions.

Our calculated tolerances should be useful, not only for manufacturers of gradient coil systems, but also research groups in the forefront of MRI, since shielded gradient coils can be constructed by well equipped machine shops.

It is important in MRI and MRS that the main magnetic field be homogeneous over an extended region. This requires an effective shimming system. However, the axial variation of the field strength in the Bruker magnet, which is predominantly fourth order in the z coordinate, could only be one-third compensated using the z^4 shim coil provided by the manufacturer, the associated power dissipation being about 100 watts leading to temperature increases in the sample space of up to 12°C in one hour. To overcome this problem, we studied the influence of various design parameters on the power dissipation and field profile of z^4 shim coils.

We considered two types of four-ring z^4 shim coils, namely those that generate no z^0 and z^2 field components (Type 1 coils), and those that generate no z^2 and z^6 field components (Type 2 coils). Type 2 coils therefore generate a field shift in addition to the z^4 shim field. This may be a disadvantage in some cases, especially if the field shift is large. Relations between the design parameters, namely the z coordinates of the inner and outer pairs of rings, and the respective currents, I_1 and I_2, flowing through them, were determined for both types of coils. The power dissipation and field profile of various designs were compared in order to find the

optimal design.

The most efficient Type 1 design was found to be one where $I_2/I_1 = -4$. It has a better field profile and a power dissipation 40% less than Romeo and Hoult's [7] design for which $I_2/I_1 = -9$. Most of the Type 2 designs were found to dissipate much less power than Type 1 designs, while at the same time approximating the desired z^4 field profile over an extended region without generating an inordinately large field shift. This led us to construct a replacement shim coil for the Bruker magnet using a Type 2 design with $I_2/I_1 = -2.5$. This enabled the z^4 field variation of the magnet to be fully compensated with a power dissipation of only 21 watts.

In summary, our results from this study enable the most appropriate z^4 shim coil design to be chosen in individual cases. The method used to compare the power dissipation of different coil designs is not restricted to z^4 shim coils. However, its most likely application is in the design of high order z^n shim coils in wide bore NMR magnets.

6.2   Design of Elliptic Cylinder Gradient Coils

The demands of new, rapid imaging sequences for fast and efficient production of strong magnetic field gradient pulses led Petropoulos et al. [8] to consider the elliptic cylinder as a preferred geometry over the circular cylinder for the former of gradient coils. However, these workers assumed that the current on the surface of the elliptic cylinder is purely azimuthal. Moreover, their treatment is in error because of the omission of an important factor from the expression for the magnetic field. Their numerical results are therefore of questionable validity.

We began our work by deriving general expressions for the magnetic field and stored energy associated with a distributed current on the surface of an elliptic cylinder, which is allowed to flow axially as well as azimuthally. We note that these

expressions can be used to design not only elliptic cylinder gradient coils but also coils which generate other field profiles such as a uniform field or higher order shim fields [7]. Relations between Mathieu-Fourier transforms of the azimuthal and axial components of the current density were derived in order to design elliptic coils of minimum inductance using the target field approach [9], when the current is not restricted to azimuthal flow.

When the general expressions were used to design an elliptic cylinder z gradient coil carrying a purely azimuthal current, it was found that, near the z axis, B_z increases parabolically in the x direction but decreases parabolically equally rapidly in the y direction. This is a direct result of the ellipticity, when the current is purely azimuthal. It was shown that it should be possible to eliminate this variation of B_z in the transverse directions by introducing a $\cos 2\eta$ dependence of the appropriate amplitude into the azimuthal component of the current density, even though this introduces a concomitant axial component.

The theory was used to design two elliptic cylinder z gradient coils of minimum inductance, with an axial ratio of the ellipse of 0.75 and eight target field points along the z axis. In the first design, the current was assumed to be purely azimuthal. Even though the gradient was found to deviate from linearity by less than 0.1% out to $z/a = 0.61$, where a is the length of the semi-major axis of the ellipse, there was substantial nonuniformity of B_z in the x and y directions, the region where B_z varies by less than 0.1% being limited to x/a or $y/a < 0.2$ in the target field region. In the second design, the η dependence of the azimuthal component of the current density was assumed to be of the form $(1 - 0.025 \cos 2\eta)$. The variation of B_z was in this case less than 0.1% out to x/a or $y/a = 0.53$, a considerable improvement over the first design. Moreover, the linearity of the gradient along the z axis was slightly better in the second design than the first.

The stored energy in generating a given gradient in the first design is 31%

129

less than that of a circular cylinder z gradient coil whose radius is equal to the semi-major axis of the ellipse. The stored energy of the second design was 26% less than that of the circular cylinder coil. Despite the fact that the stored energy of the second design is somewhat larger than that of the first design, the second design should be preferred, because of its more uniform gradient.

6.3 Future Research

Since a general theoretical treatment of elliptic cylinder coils has been accomplished, the next obvious task is to apply the theory to design elliptic cylinder transverse gradient coils. The theory can also be extended to cover the situation where the power dissipation, instead of the stored energy, is minimized.

Elliptic cylinder gradient coils, like gradient coils of other geometries, should be shielded to eliminate eddy current effects. The current distribution in a circular cylinder shielding coil surrounding an elliptic cylinder gradient coil can probably be derived numerically from the current distribution in the inner coil by means of optimization. On the other hand, the current distribution in an elliptic cylinder shielding coil, which is confocal with the inner coil, may be derived analytically, in a similar way to that for circular cylinder shielded gradient coils.

References

[1] S. Robertson, M.Sc. Thesis, University of Alberta, 1989.

[2] P. Mansfield and B. Chapman, J. Phys. E: Sci. Instrum. **19**, 540 (1986).

[3] Q. Liu, M.Sc. Thesis, University of Alberta, 1991.

[4] J. Frahm, A. Haase, and D. Matthaei, *Magn. Reson. Med.* **3**, 321 (1986).

[5] M.J. Stehling, A.M. Howseman, R.J. Ordidge, B. Chapman, R. Turner, R. Coxon, P. Glover, P. Mansfield, and R.E. Coupland, *Radiology* **170**, 257 (1989).

[6] J. Frahm, K.R. Merboldt, and W. Hanicke, *J. Magn. Reson.* **72**, 508 (1987).

[7] F. Romeo and D.I. Hoult, *Magn. Reson. Med.* **1**, 44 (1984).

[8] L.S. Petropoulos, M.A. Martens, R.W. Brown, M.R. Thompson, M.A. Morich, and J.L. Patrick, *Meas. Sci. Technol.* **4**, 349 (1993).

[9] R. Turner, *J. Phys. D: Appl. Phys.* **19**, L147 (1986).

Appendix A

DERIVATION OF EXPRESSIONS FOR α

A.1   Derivation of Eq. (3.59)

The initial amplitude of the eddy current field caused by switching on the slice selection gradient is $(B_z^{\text{eddy}})_0$. After the selective rf pulse is switched off, and before the slice selection gradient is reversed, the eddy current field has decayed to $(B_z^{\text{eddy}})_0 \exp\left(-\tau_{\text{slice}}/\tau\right)$. The change in the eddy current field, δB_z^{eddy}, during slice selection is given by

$$\delta B_z^{\text{eddy}} = \left(1 - e^{-\tau_{\text{slice}}/\tau}\right)\left(B_z^{\text{eddy}}\right)_0 . \tag{A.1}$$

By comparing Eq. (A.1) with Eq. (3.56), it is found that

$$\alpha = 1 - e^{-\tau_{\text{slice}}/\tau}, \tag{A.2}$$

which is Eq. (3.59).

A.2   Derivation of Eq. (3.62)

Immediately after reversal of the slice selection gradient, the amplitude of the eddy current field is

$$\left(-2 + e^{-\tau_{\text{slice}}/\tau}\right)\left(B_z^{\text{eddy}}\right)_0 ,$$

which decays to

$$\left(-2 + e^{-\tau_{\text{slice}}/\tau}\right) e^{-\tau_{\text{slice}}/2\tau} \left(B_z^{\text{eddy}}\right)_0$$

before the gradient is switched off. By switching off the gradient, the eddy current field becomes

$$\left(1 + e^{-3\tau_{\text{slice}}/2\tau} - 2e^{-\tau_{\text{slice}}/2\tau}\right)\left(B_z^{\text{eddy}}\right)_0 .$$

132

At the beginning of the phase encoding period in MBEST imaging, the eddy current field has decayed to

$$\left(1 + e^{-3\tau_{\text{slice}}/2\tau} - 2e^{-\tau_{\text{slice}}/2\tau}\right) e^{-[\tau_1 + (\tau_2/2)]/\tau} \left(B_z^{\text{eddy}}\right)_0.$$

Since the duration of the phase encoding period is $n\tau_2$, the change in the eddy current field during this period is given by

$$\delta B_z^{\text{eddy}} = \left(1 + e^{-3\tau_{\text{slice}}/2\tau} - 2e^{-\tau_{\text{slice}}/2\tau}\right) \left(1 - e^{-n\tau_2/\tau}\right) e^{-[\tau_1 + (\tau_2/2)]/\tau} \left(B_z^{\text{eddy}}\right)_0, \quad \text{(A.3)}$$

from which Eq. (3.62) is obtained.

A.3 Derivation of Eq. (3.64)

Assuming $\tau_3/\tau \ll 1$, and that the prepulse and the blips comprising G_{phase} in MBEST imaging all possess the same amplitude, the amplitudes of the eddy current fields caused by the prepulse and each blip are given by $[1 - \exp(-\tau_1/\tau)](B_z^{\text{eddy}})_0$ and $(-\tau_3/\tau)(B_z^{\text{eddy}})_0$, respectively. At the beginning of the first echo, the total eddy current field caused by the prepulse and the first blip is given by

$$\left[\left(1 - e^{-\tau_1/\tau}\right) u^{1/2} - \frac{\tau_3}{\tau}\right] \left(B_z^{\text{eddy}}\right)_0,$$

where $u = \exp(-\tau_2/\tau)$. This field is reduced by a factor of u^n at the end of the nth echo. At this instant, the eddy current field caused by the rest of $(n - 1)$ blips is given by

$$-\left(B_z^{\text{eddy}}\right)_0 \frac{\tau_3}{\tau} \left(u + u^2 + \cdots + u^{n-1}\right) = -\left(B_z^{\text{eddy}}\right)_0 \frac{\tau_3 u \left(1 - u^{n-1}\right)}{\tau(1 - u)}. \quad \text{(A.4)}$$

Thus, the change in the eddy current field caused by G_{phase} in MBEST imaging during the phase encoding period is given by

$$\delta B_z^{\text{eddy}} = \left\{\left[\left(1 - e^{-\tau_1/\tau}\right) u^{1/2} - \frac{\tau_3}{\tau}\right] (1 - u^n) + \frac{\tau_3 u \left(1 - u^{n-1}\right)}{\tau (1 - u)}\right\} \left(B_z^{\text{eddy}}\right)_0. \quad \text{(A.5)}$$

Equation (3.64) is then obtained by comparing Eq. (A.5) with Eq. (3.56).

A.4 Derivation of Eqs. (3.66) and (3.67)

In SE imaging, the eddy current field at the beginning of the acquisition period, caused by the read compensation gradient pulse, is given by

$$- \left(1 - e^{-\tau_{aq}/2\tau}\right) e^{-\tau_4/\tau} \left(B_z^{eddy}\right)_0 .$$

By switching on the read gradient, the total eddy current field becomes

$$\left[1 - \left(1 - e^{-\tau_{aq}/2\tau}\right) e^{-\tau_4/\tau}\right] \left(B_z^{eddy}\right)_0 .$$

At the end of the acquisition period, this field is reduced by a factor of $\exp\left(-\tau_{aq}/\tau\right)$. Therefore, the change in the eddy current field during the acquisition period is given by

$$\delta B_z^{eddy} = \left[1 - \left(1 - e^{-\tau_{aq}/2\tau}\right) e^{-\tau_4/\tau}\right] \left(1 - e^{-\tau_{aq}/\tau}\right) \left(B_z^{eddy}\right)_0 . \tag{A.6}$$

It follows that

$$\alpha = \left[1 - \left(1 - e^{-\tau_{aq}/2\tau}\right) e^{-\tau_4/\tau}\right] \left(1 - e^{-\tau_{aq}/\tau}\right) , \tag{A.7}$$

which is Eq. (3.66).

The derivation of Eq. (3.67) is similar to that of Eq. (3.66).

A.5 Derivation of Eq. (3.68)

Before the first gradient reversal in MBEST imaging, the eddy current field caused by switching on $-G_{read}$ is $-(B_z^{eddy})_0 \exp\left(-\tau_2/2\tau\right)$. At the beginning and end of the nth echo, this field will have decayed to

$$- \left(B_z^{eddy}\right)_0 e^{-[n-(1/2)]\tau_2/\tau} \qquad \text{and} \qquad - \left(B_z^{eddy}\right)_0 e^{-[n+(1/2)]\tau_2/\tau},$$

respectively. The eddy current field caused by n gradient reversals is given by

$$2\left(1 - e^{-\tau_2/\tau} + \cdots + e^{-(n-1)\tau_2/\tau}\right) \left(B_z^{eddy}\right)_0 = \frac{2\left(1 + e^{-n\tau_2/\tau}\right)}{1 + e^{-\tau_2/\tau}} \left(B_z^{eddy}\right)_0 \tag{A.8}$$

at the beginning of the nth echo, which is reduced by a factor of $\exp\left(-\tau_2/\tau\right)$ at the end of that echo. Here, we have assumed that n is odd. If n is even, the eddy current field at the beginning of the nth echo, caused by the n gradient reversals, is given by

$$-\frac{2\left(1 - e^{-n\tau_2/\tau}\right)}{1 + e^{-\tau_2/\tau}}\left(B_z^{\text{eddy}}\right)_0.$$

The change in the total eddy current field during the nth echo, caused by switching G_{read}, is therefore given by

$$\delta B_z^{\text{eddy}} = \left[-\left(e^{-(n-\frac{1}{2})\tau_2/\tau} - e^{-(n+\frac{1}{2})\tau_2/\tau}\right) + \frac{2\left(1 - e^{-\tau_2/\tau}\right)\left(1 + e^{-n\tau_2/\tau}\right)}{1 + e^{-\tau_2/\tau}}\right]\left(B_z^{\text{eddy}}\right)_0, \tag{A.9}$$

when n is odd.

For echoes near the end of the acquisition period, where n is large and $\exp\left(-n\tau_2/\tau\right) \ll 1$, Eq. (A.9) reduces to

$$\delta B_z^{\text{eddy}} = \frac{2\left(1 - e^{-\tau_2/\tau}\right)}{1 + e^{-\tau_2/\tau}}\left(B_z^{\text{eddy}}\right)_0, \tag{A.10}$$

from which Eq. (3.68) is obtained.

A.6 Derivation of Eq. (3.72)

The eddy current field at the beginning of the acquisition period, caused by the second G_{slice3} in the STEAM spectroscopy sequence, is given by

$$\left(B_z^{\text{eddy}}\right)_0\left(1 - e^{-\tau_5/\tau}\right)e^{-\tau_6/\tau}.$$

Since the eddy current field will almost completely decay during the long acquisition period, α is given by

$$\alpha = \left(1 - e^{-\tau_5/\tau}\right)e^{-\tau_6/\tau}, \tag{A.11}$$

which is Eq. (3.72).